



M Ű E G Y E T E M 1 7 8 2

BUDAPEST UNIVERSITY OF
TECHNOLOGY AND ECONOMICS

DEPARTMENT OF NETWORKED SYSTEMS AND SERVICES

Improvements in Analytical Wideband
Impedance Matching and Visible Light
Communication

Ph. D. Thesis

Author:

Balázs Matolcsy

Electrical Engineer M. Sc.

Associate supervisor:

Dr. Eszter Udvary Ph. D.

Associate Professor

Associate supervisor:

Dr. Attila Zólomy Ph. D.

Associate Professor

Budapest, 2021

Acknowledgements

I would like to first address thanks to my internal and external supervisors, Dr. Eszter Udvary and Dr. Attila Zólmoy for all the scientific advice, guidelines for the theses, publication, financial support and other supportive thoughts. Special thanks to Dr. Eszter Udvary who helped me with every possible asset for my successful studies since 2014. I would like to thank my colleagues at BME: Ágoston Schranz, Zoltán Szalay for helping me with measurements and theoretical problems. Special thanks to my colleague Dr. Zsolt Kollár who invested countless hours in enhancing and correcting my papers and gave me helpful positive thoughts and advice throughout the previous years. I would like to thank Csaba Fűzy[†] for his works in wideband matching. I'm grateful to my parents for providing me a calm and stable supportive background during my studies. Very special thanks to Réka Fincicky, my fiancée, without whom this thesis never would have been finished.

Abstract

Recently, the scientific community of telecommunication systems holds the fifth-generation telecommunication networks and systems (5G) in clear focus. Contrary to the previous generations, 5G brings a large variety of novel wireless communications into scope. These are dedicated to fulfill the large data-speed (over GBit/s), great coverage (pico- and atto-cells) and low-latency (millisecond delay range) requirements defined by the 5G guidelines. Naturally, the emphasis in the physical layer of 5G is on the higher radio-frequency (RF) bands, such as 3.3...4.2 GHz, 26 GHz and 39 GHz. All these frequency bands require carefully designed RF devices that are adequately matched to each other on the desired bandwidth of operation. In order to efficiently operate a large number of RF pico- and atto-cells for providing enhanced coverage, the energy efficiency of endpoint RF devices is crucial. As known from RF network theory, the efficiency of RF devices significantly depend on the interconnection between RF stages (amplifier, resonator, antenna). The connections are implemented with coaxial cables, transmission lines (microstrip, stripline etc.) or waveguides. The connection between two stages reach maximum efficiency if and only if the interconnected stages are matched in terms of input and output impedance. This is the main motivation of why I chose the enhancement of analytical impedance matching methods as the first scope of my thesis. During the thesis discussion I use analytical approaches for identifying the key problems of the well-known Bode-Fano matching method. In this thesis I present an improved impedance matching approach mainly based on the Bode-Fano algorithm. The improved method helps to: exclude non-realizable matching networks and find a realizable solution, automate the search for the acceptable matching network. I introduce my simulation results, where I demonstrate how the matching task is carried out step-by-step. Finally, I present the limitations of the enhanced matching method when it comes to ultra-small scale, electrically small on-chip antennas (OCA).

The 5G guidelines mention the possibility of creating local pico-, femto- and even atto-cells based on mm-Wave RF technology. This small-cell approach alleviated

the spread of alternative, not RF based communication possibilities, such as: Visible Light Communication (VLC). Recently, the majority of lighting devices are equipped with energy efficient Light Emitting Diodes (LEDs). The lighting infrastructure based on LEDs allow the small-cell VLC approach. The small-cell VLC infrastructure enables: indoor navigation, indoor positioning, high data-speed downlink data transfer, etc. VLC has several application areas, mainly where RF communication is difficult, expensive or prohibited (indoor navigation, underwater communication, indoor explosion proof areas (ATEX)). The key advantages of VLC are: potentially high data speed (up to GB/s), security (limited light propagation, small-cells), immunity to EMI (Electromagnetic Interference), license-free usage. The most important drawbacks are: required LOS (Line of Sight) between TX-RX, relatively low transmission distance (few cm to few 10 meters), sensitivity to other visible light noises (sunlight irradiance). A promising VLC application is Vehicle-to-Vehicle (V2V) communication. The demand for secure, low-latency data transmission between vehicles rose, as the concept of self-driving vehicles became reality. VLC-V2V allows real-time, secure peer-to-peer (P2P) data transmission between moving vehicles, alleviating the teamwork of vehicles in dangerous traffic situations (rear-end collisions, sudden lane-departures). For this reason, this thesis discusses VLC-V2V substantially, focusing on reducing the hindering effects of noises in the VLC-V2V channel.

Contents

Bibliography	4
List of Figures	7
List of Tables	9
1 Overcoming the Realization Problems of Wideband Impedance Matching Network Synthesis	10
1.1 Introduction	11
1.2 Analytical Wideband Impedance Matching	13
1.2.1 Theoretical Limitations of Impedance Matching	14
1.3 The Bode-Fano Method for Transmission Line Matching Networks . .	15
1.4 The Bode-Fano Method for Series R-L-C Load with Transmission Line Network	17
1.5 The Bode-Fano Method for Parallel R-L-C Load with Coupled Transmission Line Network	20
1.6 Realization Problems of Matching Networks based on Admittance Inverters	21
1.6.1 Avoiding Complex Transmission Line Impedance Values	22
1.6.2 Avoiding Negative Transmission Line Y_2 Values	23
1.6.3 Avoiding Negative Transmission Line Y_3 Values	25
1.6.4 Summary of Conditions for Avoiding Negative and Complex Impedance Values	26
1.7 Realization Problems of Matching Networks based on Impedance Inverters	26
1.7.1 Avoiding Complex Coupled Line Impedance Values	27
1.7.2 Requirements for Positive Coupled Line Impedance Values . .	29
1.7.3 Suggested Parameter Values for Avoiding Negative or Complex Coupled Line Impedance Values	32
1.8 An Example Application of the Realization Limits in Matching Tasks	33
1.8.1 Automated Matching of Series R-L-C loads	33

1.8.2	Series R-L-C Load Matching with the Iterative Algorithm . . .	37
1.9	Application Limitations of Analytical Matching	39
1.9.1	On-chip Antenna Design and Matching Problems in UHF-RFID Applications	40
1.10	Summary of Thesis I.	50
2	Differential Space-Divided 2x2 Visible Light Communication in Vehicle-to-Vehicle Applications	52
2.1	Introduction	53
2.2	Applications of Visible Light Communication	55
2.2.1	Underwater Communication	56
2.2.2	Indoor Localization and Navigation	56
2.2.3	Vehicle-to-X (V2X) Communication	57
2.3	Visible Light Communication in Vehicle-to-Vehicle Applications (VLC-V2V)	58
2.4	The Concept of Differential Space-Divided 2x2 VLC-V2V	60
2.4.1	Mathematical Background of 2x2 C-SD and 2x2 D-SD for VLC-V2V	61
2.5	2x2 D-SD VLC-V2V Simulation Environment and Results	64
2.5.1	The Simulated 2x2 D-SD Noise Rejection Performance	65
2.5.2	The Effects of Noise Amplitude Imbalance on Noise Rejection Performance	69
2.5.3	The Effects of Crosstalk Between Transmitted Signals	71
2.5.4	Simulation Results Summary	71
2.6	Visible Light Noise Measurement in Urban Environment Under Low-Light Conditions	73
2.6.1	Measurement Setup and Data Processing	73
2.6.2	Evaluation of Measurement Results	75
2.7	Indoor Laboratory Measurement Results for 2x2 D-SD VLC-V2V	76
2.7.1	Measurement setup	76
2.7.2	Noise Rejection Performance Measurement of 2x2 D-SD and 2x2 C-SD VLC-V2V	77
2.7.3	Measurement Results and Conclusion	78
2.7.4	Improvements in Crosstalk Reduction for 2x2 D-SD VLC-V2V Systems	79
2.7.5	Measurement Results with Receiver FOV Limiter	80
2.7.6	Future Plans for Crosstalk Reduction in 2x2 D-SD Systems	80

2.8	Summary of Thesis II.	81
3	Novel Scientific Results: Summary of Theses and List of Related Publications	84
3.1	Thesis I. - Overcoming the Realization Problems of Wideband Impedance Matching Network Synthesis	84
3.2	Thesis II. - Differential Space-Divided 2x2 Visible Light Communication in Vehicle-to-Vehicle Applications	88
3.2.1	Introduction	88
	Bibliography	92

List of Figures

1.1	The block diagram of single-stage microwave system.	14
1.2	Third-order matching network with series R-L-C load configuration .	20
1.3	Third-order coupled transmission line matching network realization example with parallel R-L-C load.	22
1.4	Acceptable and unacceptable matching results	35
1.5	Block-diagram of the iterative matching process	36
1.6	Successful series R-L load matching task, with matching window and results.	38
1.7	The schematic of the matching network with shorted quarter-wave shunt stubs in a microstrip realization.	39
1.8	First, second and third-order Peano curves [34].	42
1.9	First, second and third-order Hilbert curves [35].	42
1.10	Self-complementary planar spiral antenna structure [31].	42
1.11	Top view of the RFID chip with the tag antenna surrounding it. [39] .	44
1.12	3D model of the USPT in CST Microwave Studio 2018.	45
1.13	The USPT wideband circuit model.	45
1.14	Power flow parallel to the X-Y plane, at Z=5 mm.	47
1.15	First antenna performance, x-axis.	47
1.16	First antenna performance, y-axis.	48
1.17	3D spiral antenna model, perspective-view.	49
1.18	3D multi-layered spiral antenna power flow, x-axis.	49
1.19	3D spiral antenna power flow, y-axis.	50
2.1	The concept of Visible Light Communication (VLC).	53
2.2	Multi-room, multi-user VLC scenario. No light penetration through the walls, hence eavesdropping among users may not happen. [43] . .	55
2.3	An Underwater Visible Light Communication scenario (U-VLC). [50]	56
2.4	Indoor positioning and navigation via spatially distributed VLC transmitter anchors and devices equipped with VLC receivers.	57
2.5	V2X Communication via VLC	58
2.6	V2V-VLC situations	59

2.7	VLC receiver at the back of the vehicle.	61
2.8	The D-SD VLC-V2V vs. C-SD VLC-V2V solution.	62
2.9	Schematic diagram of the signals and signal routes implemented in the simulation environment.	65
2.10	2x2 CT simulation results.	67
2.11	2x2 DT simulation results.	68
2.12	The effect of noise imbalance between receivers on the Q-factor.	70
2.13	The effect of noise imbalance between receivers on the BER.	70
2.14	The effect of overlapping beams at receivers. Q-factor vs. crosstalk value.	72
2.15	The effect of overlapping beams at receivers. BER vs. crosstalk value.	72
2.16	The table for choosing the 2x2 D-SD over 2x2 C-SD, with respect to crosstalk, noise amplitude and noise amplitude balance.	73
2.17	Receiver arrangement for road testing on the car's trunk lid.	74
2.18	Road test measurement setup block diagram.	74
2.19	Visible light noise measurement results.	75
2.20	The schematic diagram of the indoor measurement setup.	76
2.21	Indoor laboratory measurement setup, for 2x2 D-SD vs. 2x2 C-SD comparison with deactivated common-mode noise source.	77
2.22	Indoor laboratory measurement setup for the 2x2 D-SD vs. 2x2 C-SD comparison, with activated common-mode noise source.	78
2.23	Noise rejection performance comparison between 2x2 D-SD and 2x2 C-SD.	78
2.24	Noise rejection performance with FOV limiters.	81
2.25	VLC-V2V using adaptively controlled LED headlight segments	82

List of Tables

1.1	Realization constraints for single reactance resistive loads.	16
1.2	Input parameters for the series R-L matching task with the iterative method	37
1.3	Matching network parameters and low-pass filter prototype values calculated with the iterative algorithm.	38
1.4	The calculated optimized matching network impedance values	38
2.1	Simulation parameters for the noise reduction comparison.	66
2.2	Changed simulation parameters for the noise amplitude balance investigation simulation.	69

Chapter 1

Overcoming the Realization Problems of Wideband Impedance Matching Network Synthesis

1.1 Introduction

The majority of microwave devices contains several four-poles and two-poles attached to each other with microwave transmission lines, waveguides or coaxial cables depending on the frequency band of operation and transmitted power. As known from linear network theory, if an electromagnetic wave meets an inhomogeneity of any kind (connection port, termination, dielectric material), power reflection occurs. The goal is to minimize reflected power and maximize transmitted power across the whole microwave network chain. There are minor exceptions, such as microwave oscillator design. All in all, the minimalization of reflection is the key to high-quality interconnections, acceptable transmission efficiency and overload protection of microwave devices.

The ratio between the reflected and the transmitted electromagnetic wave, or power, is an explicit function of the input and output impedances of the attached N-port networks. It is also a well-known fact that the best power transmission ratio is available when the connected microwave networks' input and output impedance is matched. Unfortunately, in most cases the connected microwave devices are not inherently matched, therefore additional impedance matching networks between the adjacent devices are required. An ideal impedance matching network consists of only lossless reactive components, causes no additional insertion loss and reduces the reflection coefficient to zero in the desired operational frequency band. It goes without saying that the synthesis of such impedance matching networks is an undoubtedly difficult task. The level of difficulty depends on the frequency dependent behavior and impedance value difference between the adjacent devices. One of the greatest challenges is the wideband matching of complex impedances, due to the frequency dependent behavior.

Therefore, several wideband matching methods have been developed for such tasks. Generally, these methods are separated into two main groups: analytical and numerical. Analytical methods use the theory of double-terminated filter synthesis in order to obtain a satisfactory result. It's been shown by Bode and Fano in [8] and [9] that impedance matching network synthesis is analogous to filter network design. The task in case of the Bode-Fano method starts by load impedance classification. This requirement came from Fano's work, where he created a generalized solution for any lossless two-port that is terminated in a unity value resistance. However, due to the complexity of the calculation above for more than one reactive components, single-reactance models are required [9]. Then the synthesis of the low-pass filter prototype, later the frequency and impedance scaling is carried out. The advantage

of analytical matching is that filter synthesis processes are well-documented in literature and the desired frequency response functions are relatively straightforward to obtain [10, 11, 12] (Chebyshev, maximally flat, elliptical etc.). Additionally, analytical methods always give an exact result, without the need for computationally expensive numerical calculations. The drawback of the analytical method presented by Bode and Fano is that only single-reactance resistive load models are allowed (parallel R-C, R-L; series R-C, R-L). Even though this may restrict the application area of analytical matching, several real-life matching tasks are easy to handle with it.

Youla introduced an analytical wideband impedance matching method based on complex normalization and network synthesis [13, 14]. An extended step-by-step example of the matching process is found in [15]. The benefit of Youla's method is that it can be extended for not purely real generator impedances as well. Youla gave closed-form solutions for parallel R-C and series R-L networks. Parallel R-L and series R-C loads are also supported, but it may provide non-realizable matching networks in some situations (negative capacitance or inductance values). The largest drawback of the Youla-method, and this is generally true for the analytical matching methods, is that the resistive part of the load impedance and the generator impedance must be equal. Otherwise, additional impedance transformers are needed, causing realization problems for wideband solutions. Summarizing the above, Youla's method is similar to the general double-terminated filter synthesis process (Bode-Fano method). However, it has got some limitations regarding physical realization and load types, but generally it is a viable alternative to the analytical solution provided by Bode and Fano method.

Apart from the analytical solutions, there are few numerical impedance matching methods. The most important and widely used is called Real-Frequency-Technique (RFT). In contrast to analytical methods, RFT inherently does not require a single-reactance load impedance model. The fundamental mechanism of RFT is the sampling of the real part of the load impedance as a function of frequency. Therefore no load impedance model is required. This numerical approach was first introduced by H. J. Carlin in [16]. His greatest contribution was in noting that a piecewise linear approximation of the real-part of the load impedance R_L enables the simple computation of the imaginary part X_L , through Hilbert transformation, provided that the impedance function has the property of minimal reactance [17]. Furthermore, he showed that a nonlinear optimization program would usually succeed in obtaining power transfer or several other impedance-dependent objectives by a piecewise fit of R_L . Then the Gewertz method [18] is used

to synthesize the impedance-frequency function from the resistance-frequency function. The resistance-frequency function should be given in the form of rational polynomials. The computational complexity of this method is reasonably higher than analytical methods and the resulting low-pass prototype network values often fall into a physically non-realizable range. Moreover, the obtained matching networks calculated with RFT mostly need further numerical optimization, especially if a band-pass response is required.

For this reason, I opted for extending and enhancing the usability of the analytical matching method presented by Bode and Fano. This chapter will present this commonly used wideband impedance matching solution, that can handle complex load impedances. I also provide an in-depth look and deep analysis of the Bode-Fano method. I highlight the problems occurring during the matching network synthesis process and propose new rules (constraints) to obey during the synthesis and an algorithmic approach to automate the network synthesis process, keeping physical realization goals in focus. By using the matching network algorithm I proposed together with the restriction rules I present in this chapter, finding a realizable matching network solution becomes remarkably easier and faster.

1.2 Analytical Wideband Impedance Matching

The optimum power transmission between multi-poles happens when the corresponding input and output impedances are matched [19, 20, 21]. In order to define the quality of matching, first the voltage reflection coefficient is introduced. The reflection coefficient between A and Z_L (see Fig. 1.1) is defined as

$$\Gamma_{\text{out}} = \frac{Z_L - Z_{\text{out}}}{Z_L + Z_{\text{out}}}. \quad (1.1)$$

As input and output impedances of microwave stages are generally complex (not necessarily purely real), the condition of perfect impedance matching between stages happens when

$$Z_{\text{out}} = Z_L^*. \quad (1.2)$$

For simultaneous matching on both the generator and the load side, the following equations must hold

$$\Gamma_{\text{out}} = \frac{Z_L - Z_{\text{out}}}{Z_L + Z_{\text{out}}} = 0 \quad \text{and} \quad \Gamma_{\text{in}} = \frac{Z_{\text{in}} - R_g}{Z_{\text{in}} + R_g} = 0. \quad (1.3)$$

Therefore the goal of the impedance matching network synthesis is to design a four-pole that has the following properties

$$Z_{\text{in}} = R_g \quad \text{and} \quad Z_{\text{out}} = Z_L^*. \quad (1.4)$$

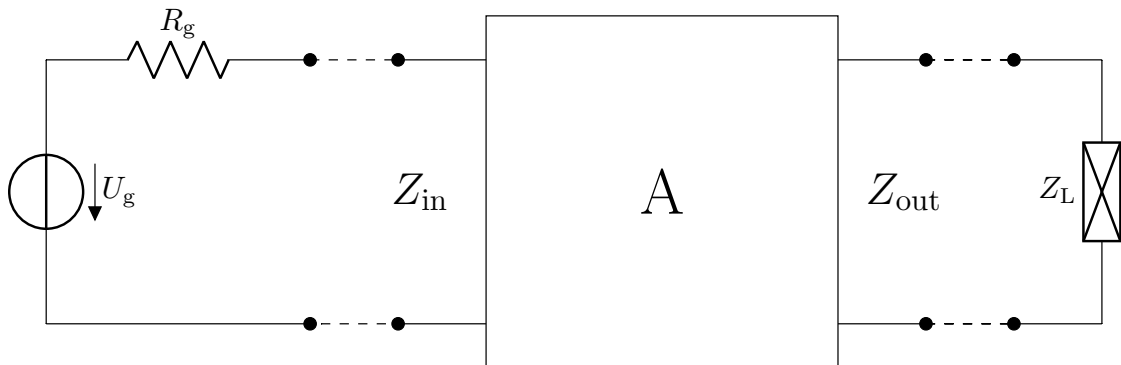


Figure 1.1: The block diagram of single-stage microwave system.

1.2.1 Theoretical Limitations of Impedance Matching

Bode first introduced his theoretical wideband matching limitations for a parallel R-C load [8]. He derived that there is a physical limitation on what Γ can be as a function of frequency. A few years later Fano presented his general limitations on all types of load impedances [9]. Fano pointed out that efficiency of transmission and bandwidth are exchangeable quantities in the impedance matching of any load containing a reactive component. Bode showed that there is a physical limitation on what the reflection coefficient can be as a function of frequency

$$\int_0^{\infty} \ln \left| \frac{1}{\Gamma} \right| d\omega = \frac{\pi}{RC}. \quad (1.5)$$

If a good matching is only required between frequencies ω_1 to ω_2 and for the rest of the total interval $\Gamma = 1$

$$\int_{\omega_1}^{\omega_2} \ln \left| \frac{1}{\Gamma} \right| d\omega = \frac{\pi}{RC} \quad (1.6)$$

Evaluating this definite integral

$$|\Gamma| = \exp \left(\frac{-\pi}{(\omega_1 - \omega_2) RC} \right) \quad \text{for } \omega_1 \leq \omega \leq \omega_2, \quad (1.7)$$

$$|\Gamma| = 1 \quad \text{for } 0 \leq \omega \leq \omega_1 \quad \text{and} \quad \omega_2 \leq \omega \leq \infty. \quad (1.8)$$

This statement claims that the best impedance matching of a parallel R-C load is a band-pass filter that minimizes reflection between ω_1 and ω_2 . This limit can only be reached in theory, as such matching network would require an infinite number of elements. This theoretical limit is used for qualifying a practical, finite-order matching network by comparing it to the theoretical limit. Fano took Bode's idea further by giving a closed form solution for all single-reactance resistive and R-L-C

loads [9]. The theoretical limitations for such loads are

$$|\Gamma_{\text{limit}}| = \exp\left(-\frac{\pi \omega_1 L}{R}\right) \quad \text{for parallel R-L load,} \quad (1.9)$$

$$|\Gamma_{\text{limit}}| = \exp\left(-\frac{\pi R}{\omega_1 L}\right) \quad \text{for series R-L load,} \quad (1.10)$$

$$|\Gamma_{\text{limit}}| = \exp(-\pi RC \omega_1) \quad \text{for series R-C load,} \quad (1.11)$$

$$|\Gamma_{\text{limit}}| = \exp(-\pi \delta) \quad \text{for band-pass structure.} \quad (1.12)$$

These limits are defined for infinite element low-pass matching networks, where ω_1 is the low-pass cutoff frequency. Whereas, for band-pass R-L-C structures

$$|\Gamma_{\text{limit}}| = \exp(-\pi \delta). \quad (1.13)$$

The parameter δ is the quantity for identifying the impedance [22], it is called decrement. It is in a close relationship with the quality factor Q . The equation for determining the decrement is

$$\delta = \frac{\sqrt{\omega_1 \omega_2}}{\omega_1 - \omega_2} \frac{1}{Q}, \quad (1.14)$$

where ω_1 and ω_2 represents the -3 dB bandwidth points of the band-pass structure. With these theoretical limitations for an infinite element matching network kept in mind, qualification of finite element matching networks gets easier. In practice, only finite order matching networks are used (third-, fifth-order).

1.3 The Bode-Fano Method for Transmission Line Matching Networks

The Bode-Fano method is based on the Darlington-theorem: an arbitrary passive complex load can be substituted with a passive, reactant, lossless network that is terminated in a unity value resistance [23]. This principle allows impedance matching to be redefined, as a double-terminated filter synthesis task. The Darlington-synthesis is capable of providing a low-pass filter prototype for such problems. The analytical method for broadband impedance matching was thoroughly described by Fano [9]. He extended Bode's integral matching limitation for R-C load networks to load networks composed of any number of L-C elements terminated in a resistance. However, the theory becomes too complicated for more than two load reactance elements, therefore mostly single-reactance models are used. The subject is invariably presented as the low-pass case; i.e., loads are parallel R-C or series R-L and the matching frequency band begins at 0 Hz. However, real-life

applications usually require pass bands above 0 Hz, that are obtained by a simple network transformation and the loads are R-L-C structures. Thus, the development requires consideration of the transformation that changes the network from low-pass to band-pass. This broadband-matching concept requires that the matched load must be related to a hypothetical lumped-element terminating network. This is called load classification, i.e. modeling the load impedance with a single-reactance lumped model that resembles the original load adequately. The major problem with the Darlington-synthesis is that the generator impedance is determined as the synthesis result [23]. This is not generally acceptable. Therefore, for arbitrary generator impedance values, an extended matching solution is required. Possible solutions are: impedance transformers or admittance/impedance inverters [12, 22]. To properly summarize the abilities and matching network realization methods of the Bode-Fano method, Tab. 1.1 presents all the solutions for single-reactance type loads.

	Series R-L-C	Parallel R-L-C
Transmission Line	ST, ADI	CL, IMI
Lumped Elements	ADI-L or TR	IMI-L or TR

Table 1.1: Realization constraints for single reactance resistive loads.

The abbreviations used in Tab. 1.1 are as follows.

- ST: Shorted Quarter-Wave Stub Network Realization
- CL: Coupled Line Transmission Line Network Realization
- ADI: Admittance Inverter is used
- IMI: Impedance Inverter is used
- ADI-L: Lumped Element Admittance Inverter
- IMI-L: Lumped Element Impedance Inverter
- TR: Transformer (ideal, wideband)

In this section, I focus on the transmission line matching network realization with Chebyshev-response for band-pass load configurations: series R-L-C and parallel R-L-C. Series R-L and R-C loads must be extended with a capacitor or inductor for series resonance. Parallel structures must be extended with a capacitor/inductor for parallel resonance. The detailed process of deciding, whether series or parallel

resonance tuning is required can be found in [22]. The series R-L-C structure requires admittance inverters for independent source impedance values, whereas the parallel R-L-C requires impedance inverters as shown in Tab. 1.1.

1.4 The Bode-Fano Method for Series R-L-C Load with Transmission Line Network

The matching network synthesis process begins with the input parameter constraints, such as matching network order, center frequency, relative bandwidth, R-L-C values, Chebyshev-ripple factor. For demonstration purposes, I included the detailed matching steps of matching a series R-L load to a purely real generator impedance using a third-order ideal matching network. As I mentioned earlier, the first step is to calculate the series capacitance value for resonance at the center frequency f_c

$$C_s = \frac{1}{4\pi^2 f_c^2 L}. \quad (1.15)$$

The quality factor Q for this R-L-C structure is

$$Q = \frac{2\pi f_c L}{R}. \quad (1.16)$$

The theoretical matching limit, as shown in Eq. 1.18 is calculated using the decrement factor,

$$\delta = \frac{1}{Q} \frac{\sqrt{4\pi^2 f_h f_l}}{2\pi(f_h - f_l)}, \quad (1.17)$$

where f_h is the upper and f_l is the lower frequency limit. Using the decrement factor and the minimum of the reflection coefficient on the desired bandwidth is expressed

$$|\Gamma_{\text{limit}}| = 20 \log_{10} (\exp(-\pi\delta)), \quad (1.18)$$

where $|\Gamma_{\text{limit}}|$ stands for the best available reflection coefficient in case of an ideal matching network consisting of an infinite number of lossless, passive components. The $|\Gamma_{\text{limit}}|$ parameter is used for the comparison of the theoretical and the finite-order matching quality. The following equations are required for the low-pass filter prototype of the matching circuit,

$$d = \sinh \frac{\sinh^{-1} \sqrt{\frac{1}{10^{(\tau/10)} - 1}}}{n}, \quad (1.19)$$

$$D = \frac{d}{\delta \sin\left(\frac{\pi}{2n}\right)} - 1, \quad (1.20)$$

where n represents the order of the matching circuit and r stands for the maximal allowed Chebyshev-ripple factor in the matched frequency band. These parameters are used for evaluating the coupling coefficients for the low-pass filter prototype network provided by Green in [24]

$$k_{1,2} = \sqrt{\frac{3}{8} \left(1 + \left(1 + \frac{D^2}{3} \right) \delta^2 \right)}, \quad (1.21)$$

$$k_{2,3} = \sqrt{\frac{3}{8} \left(1 + \left(\frac{1}{3} + D^2 \right) \delta^2 \right)}. \quad (1.22)$$

Based on [17] and [22], the low-pass filter prototype component values for the double-terminated filter are

$$g_0 = 1, \quad (1.23)$$

$$g_1 = \frac{1}{\delta}, \quad (1.24)$$

$$g_2 = \frac{1}{g_1 k_{1,2}^2}, \quad (1.25)$$

$$g_3 = \frac{1}{g_2 k_{2,3}^2}, \quad (1.26)$$

$$g_4 = \frac{1}{D \delta g_3}. \quad (1.27)$$

As seen in Eq. 1.23, the generator impedance ($g_0 = 1$ or $Rg = 1$) is determined as the synthesis result. This overrides the original generator impedance and this is unacceptable. Furthermore, this is a low-pass filter prototype circuit, therefore filter transformation steps are required for a pass-band configuration. In order to alter the determined generator impedance and achieve a band-pass response; admittance inverters are used. For the transmission line admittance inverter synthesis, further parameters are required

$$d_p > 0, \quad (1.28)$$

$$\omega_m = \frac{(f_h - f_l)}{f_c}, \quad (1.29)$$

$$\Theta_1 = \frac{\pi}{2} \left(1 - \frac{\omega_m}{2} \right) \quad (1.30)$$

The admittance inverter parameters for the third-order matching network are

calculated using equations in [17, 22]

$$C_2 = g_2, \quad (1.31)$$

$$C_3 = g_0 g_3 g_4 \frac{R_L}{R_g}, \quad (1.32)$$

$$C'_2 = g_2 (1 - d_p), \quad (1.33)$$

$$C''_2 = d_p g_2, \quad (1.34)$$

$$C'_3 = C''_2, \quad (1.35)$$

$$C''_3 = C_3 - C'_3, \quad (1.36)$$

$$J_{2,3} = \frac{1}{R_L g_0} \sqrt{\frac{C_2 C_3}{g_2 g_3}}, \quad (1.37)$$

$$N_{2,3} = \sqrt{(J_{2,3} R_L)^2 + \left(\frac{C''_2 \tan(\Theta_1)}{g_0}\right)^2}. \quad (1.38)$$

The construction of the matching network is based on quarter-wavelength, shorted transmission line stubs. The shorted stubs only have a single free parameter in this case: transmission line admittance. These admittance values are

$$Y_2 = \frac{1}{g_0 R_L} C'_2 \tan(\Theta_1) + \frac{1}{R_L} (N_{2,3} - J_{2,3} R_L), \quad (1.39)$$

$$Y_3 = \frac{1}{g_0 R_L} C''_3 \tan(\Theta_1) + \frac{1}{R_L} (N_{2,3} - J_{2,3} R_L), \quad (1.40)$$

$$Y_{2,3} = J_{2,3}. \quad (1.41)$$

The impedance values are defined as the reciprocals of the corresponding admittance values

$$Z_2 = \frac{1}{Y_2}, \quad (1.42)$$

$$Z_3 = \frac{1}{Y_3}, \quad (1.43)$$

$$Z_{2,3} = \frac{1}{Y_{2,3}}. \quad (1.44)$$

This was the last step of the matching networks synthesis process. The following step is to implement the matching network and simulate the response combined together with the load. In ideal situations when these matching network impedance values are positive, purely real and fall into the realizable impedance value range (e.g. for microstrip realizations: $15 \Omega < Z_{ij} < 150 \Omega$), then the matching task is considered successful. A possible realization of the matching network is shown in Fig. 1.2. However, this is not generally ensured by the Bode-Fano method. And combining the Bode-Fano method with admittance inverters does have some serious

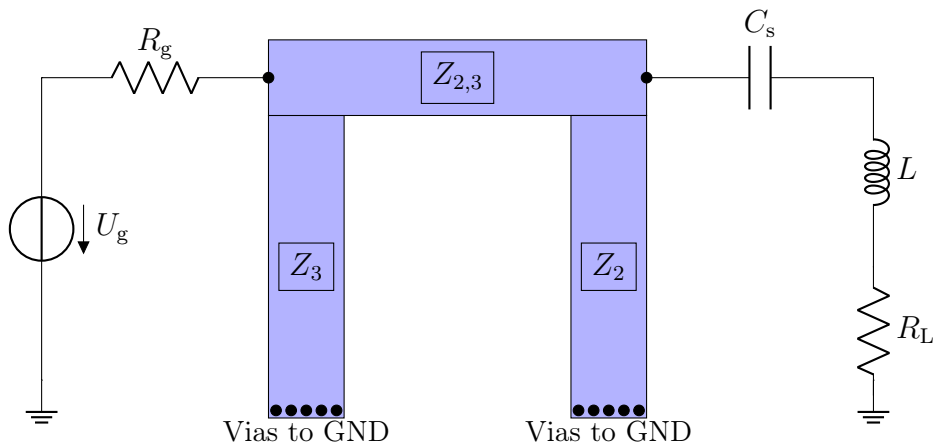


Figure 1.2: Third-order matching network with series R-L-C load configuration in a microstrip transmission line realization.

realization problems. I first ran into these problems during the first investigations of the Bode-Fano method. This is the reason why I decided to thoroughly investigate the stems of non-realizable matching networks and try to give an adequate solution for avoiding them.

1.5 The Bode-Fano Method for Parallel R-L-C Load with Coupled Transmission Line Network

The equations for matching a parallel R-L-C load using impedance inverters consisting of ideal coupled transmission lines is presented in this section. The calculation steps for the parallel R-L-C load configuration are very similar to the ones presented in the previous section. It is important to note that the calculation steps are exactly the same up to the point, where the low-pass prototype values are defined (g_0, g_1, \dots, g_4). For parallel R-L-C loads, impedance inverters are required. Impedance inverter realization is done by using edge coupled transmission lines (shown in Fig. 1.3). The auxiliary parameters [22] for calculating the impedance

inverter values are

$$L_2 = g_2, \quad (1.45)$$

$$L_3 = g_0 g_3 g_4 \frac{R_g}{R_L}, \quad (1.46)$$

$$L'_2 = g_2 (1 - d_p), \quad (1.47)$$

$$L''_2 = d_p g_2, \quad (1.48)$$

$$L'_3 = L''_2, \quad (1.49)$$

$$L''_3 = L_3 - L'_3, \quad (1.50)$$

$$K_{2,3} = R_L \sqrt{\frac{L_2 L_3}{g_2 g_3}}, \quad (1.51)$$

$$\Theta_1 = \frac{\pi}{2} \left(1 - \frac{\omega_m}{2}\right), \quad (1.52)$$

$$M_{2,3} = \sqrt{\left(\frac{K_{2,3}}{R_L}\right)^2 + \left(\frac{L''_2 \tan(\Theta_1)}{g_0}\right)^2}. \quad (1.53)$$

The coupled transmission line odd- and even-mode impedance values [22] are

$$(Z_{0\text{-even}}^a)_{2,3} = \frac{R_L L'_2}{g_0} \tan(\Theta_1) + (R_L M_{2,3} + K_{2,3}), \quad (1.54)$$

$$(Z_{0\text{-odd}}^a)_{2,3} = \frac{R_L L'_2}{g_0} \tan(\Theta_1) + (R_L M_{2,3} - K_{2,3}), \quad (1.55)$$

$$(Z_{0\text{-even}}^b)_{2,3} = \frac{R_L L''_3}{g_0} \tan(\Theta_1) + (R_L M_{2,3} + K_{2,3}), \quad (1.56)$$

$$(Z_{0\text{-odd}}^b)_{2,3} = \frac{R_L L''_3}{g_0} \tan(\Theta_1) + (R_L M_{2,3} - K_{2,3}). \quad (1.57)$$

Finally, the odd- and even-mode impedance coupled transmission lines are realized, hopefully resulting in an adequate matching network. However, similarly to the previous admittance inverter based solution presented in Sec. 1.4 realization problems may arise during the synthesis process. I'm going to address these problems in the following two sections.

1.6 Realization Problems of Matching Networks based on Admittance Inverters

If the Bode-Fano method for series R-L-C structures is combined with the admittance inverter synthesis, serious physical realization problems may arise. During the calculation process of the admittance inverter values there are situations, where the final transmission line impedance values are not purely real or negative. This is generally not acceptable as lossless, passive matching networks are required.

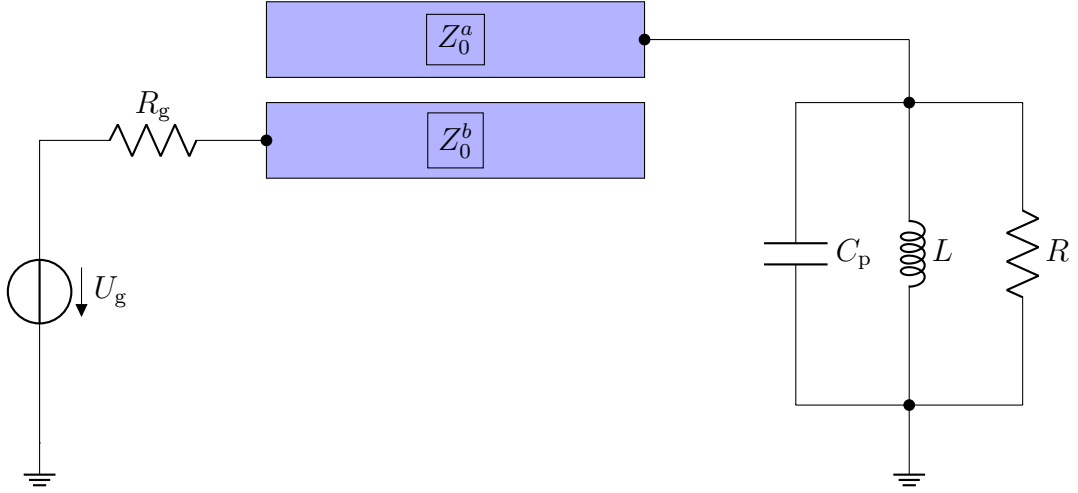


Figure 1.3: Third-order coupled transmission line matching network realization example with parallel R-L-C load.

Unfortunately, the admittance inverter synthesis process has no limitations defined for avoiding such unacceptable networks. The aim of this thesis section is to present my results regarding the in-depth analysis of the Bode-Fano synthesis process, combined with admittance inverter synthesis problems. In the end, I suggest a method for avoiding non-realizable matching networks and systematic optimization of finding acceptable and realizable matching networks.

1.6.1 Avoiding Complex Transmission Line Impedance Values

All impedance values contain the parameter $J_{2,3}$, the analysis begins with $J_{2,3}$. I'm going to start with the final equation

$$Y_{2,3} = J_{2,3}. \quad (1.58)$$

The aim is to avoid complex or negative admittance values, hence the equation of parameter $J_{2,3}$ needs further investigation

$$J_{2,3} = \frac{1}{R_L} \sqrt{\frac{C_2 C_3}{g_2 g_3}}. \quad (1.59)$$

Parameter R_L represents the real part of the load impedance, that is assumed to be always positive. The square-root function has the inherent property of providing only purely real or purely imaginary result, if the values on which the square-root function was applied to are purely real. Accordingly, the only task is to determine whether the value on which the square-root function is applied, is less than zero?

$$\frac{C_2 C_3}{g_2 g_3} < 0 \quad (1.60)$$

As the parameters are multiplied together, only an odd number of negative coefficients in the expression can yield a negative result. Due to the fact, that the decrement δ and Green-coefficients $k_{1,2}$ and $k_{2,3}$ are always greater than or equal to zero (and purely real), g_0 , g_1 and g_2 can only be positive (and purely real). Thus, a negative value in Eq. 1.60 can only occur if $C_3 < 0$, leading to $g_4 < 0$. Parameter g_4 is negative if $D < 0$ yielding

$$\frac{d}{\delta \sin\left(\frac{\pi}{2n}\right)} < 1. \quad (1.61)$$

Assuming that $n = 3$ (third-order matching network) and $\delta > 0$

$$\text{Im}(J_{2,3}) = 0 \quad \text{if and only if} \quad 2d > \delta. \quad (1.62)$$

In order to avoid complex or negative transmission line admittance value in third-order matching networks for $Y_{2,3}$, the mandatory rule is to ensure that

$$d > \frac{\delta}{2}. \quad (1.63)$$

On one hand, parameter d can be adjusted by modifying parameter r , which adjusts the amount of allowed Chebyshev-ripple in the matched frequency band, on the other hand the decrement is determined by the quality factor and the relative bandwidth. If the matching task allows the modification of either r , f_c or b this mandatory rule can be fulfilled. Implying that this condition is fulfilled, it is clear from the equations that all other admittance values (Y_2 and Y_3) are purely real without any further condition.

1.6.2 Avoiding Negative Transmission Line Y_2 Values

Similarly to the case of $Y_{2,3}$, first the equation of Y_2 is analyzed

$$Y_2 = \underbrace{\frac{1}{g_0 R_L} C'_2 \tan(\Theta_1)}_A + \underbrace{\frac{1}{R_L} (N_{2,3} - J_{2,3} R_L)}_B. \quad (1.64)$$

The equation of Y_2 is a sum of two separate terms denoted as Term A and Term B in Eq. 1.64. Both terms must be analyzed separately. First, I begin with the analysis of Term B . Assuming that Eq. 1.63 is fulfilled, $J_{2,3}$ and R_L are considered purely real and positive. The first question is whether, there is a parameter combination when

$$(N_{2,3} - J_{2,3} R_L) < 0. \quad (1.65)$$

By rearranging Eq. 1.65 and substituting parameters

$$N_{2,3} < J_{2,3} R_L \quad ? \quad (1.66)$$

$$\sqrt{\frac{C_2 C_3}{g_2 g_3} + \frac{(C_2 \tan(\Theta_1))^2}{R_L^2}} < \sqrt{\frac{C_2 C_3}{g_2 g_3}} \quad ? \quad (1.67)$$

As $(C_2 \tan(\Theta_1))^2$ is always positive and the square-root function increases monotonically for positive purely real values, Eq. 1.66 leads to a contradiction. The left side of the inequality is always greater than the right.

$$N_{2,3} > J_{2,3} R_L \quad (1.68)$$

$$\sqrt{\frac{C_2 C_3}{g_2 g_3} + \frac{(C_2 \tan(\Theta_1))^2}{R_L^2}} > \sqrt{\frac{C_2 C_3}{g_2 g_3}} \quad (1.69)$$

Consequently, the second term of the sum in Eq. 1.64 (denoted as B) is always positive. Therefore, $Y_2 < 0$ if and only if $C'_2 \tan(\Theta_1) < 0$. Starting with the analysis of $\tan(\Theta_1)$

$$\Theta_1 = \frac{\pi}{2} \left(1 - \frac{\omega_m}{2}\right) \quad \text{and} \quad 0 \leq \omega_m \leq 2, \quad (1.70)$$

$$0 \leq \Theta_1 \leq \frac{\pi}{2}, \quad (1.71)$$

$$\tan(\Theta_1) \geq 0. \quad (1.72)$$

As $\tan(\Theta_1) \geq 0$ the only remaining question is whether $C'_2 < 0$ can happen?

$$C'_2 = g_2 (1 - d_p) = \frac{\delta}{k_{1,2}^2} (1 - d_p) \quad (1.73)$$

Parameter $k_{1,2}^2$ and δ are always positive and purely real. However, if $d_p > 1$ then $C'_2 < 0$. The inverse condition ($d_p < 1$) in this case is sufficient for avoiding $Y_2 < 0$. In cases where $d_p > 1$ further investigation is required.

The Necessary Condition for $Y_2 > 0$ if $d_p > 1$.

$$Y_2 = \underbrace{\frac{1}{g_0 R_L} C'_2 \tan(\Theta_1)}_A + \underbrace{\frac{1}{R_L} (N_{2,3} - J_{2,3} R_L)}_B, \quad (1.74)$$

can be rewritten by substituting into the variables as

$$\frac{g_2 (1 - d_p) \tan(\Theta_1)}{R_L} + \sqrt{J_{2,3}^2 + \left(\frac{d_p g_2 \tan(\Theta_1)}{R_L}\right)^2} - J_{2,3} > 0 \quad ? \quad (1.75)$$

Introducing a new variable

$$U = \frac{\tan(\Theta_1) g_2}{R_L}, \quad (1.76)$$

the previous equation can be rewritten in the form

$$-(d_p - 1) U + \sqrt{J_{2,3}^2 + (d_p U)^2} - J_{2,3} > 0. \quad (1.77)$$

Rearranging the terms and raising to the square

$$J_{2,3}^2 + (d_p U)^2 > U^2 (d_p^2 - 2 d_p + 1) + 2 (d_p - 1) U J_{2,3} + J_{2,3}^2, \quad (1.78)$$

$$0 > -2 d_p U^2 + U^2 + 2 (d_p - 1) U J_{2,3}, \quad (1.79)$$

$$2 d_p U > U + 2 (d_p - 1) J_{2,3}. \quad (1.80)$$

Finally, the necessary condition for $Y_2 > 0$ if $d_p > 1$ is

$$U > \frac{U}{2 d_p} + 2 \frac{(d_p - 1)}{d_p} J_{2,3}. \quad (1.81)$$

In this case the parameters used for checking whether $Y_2 > 0$ are: $Y_{2,3}$, $\tan(\Theta_1)$, d_p , R_L , $k_{1,2}$, δ .

1.6.3 Avoiding Negative Transmission Line Y_3 Values

Similarly to the case of Y_2 , first the equation of Y_3 is analyzed

$$Y_3 = \underbrace{\frac{1}{g_0 R_L} C_3'' \tan(\Theta_1)}_C + \underbrace{\frac{1}{R_L} (N_{2,3} - J_{2,3} R_L)}_E. \quad (1.82)$$

The equation defining Y_3 is a sum of two separate terms denoted as C and E in Eq. 1.82 both must be analyzed separately. As known from the previous section, Term E is positive and $\tan(\Theta_1) \geq 0$, therefore the only questionable parameter is C_3'' .

$$C_3'' = C_3 - C_3' = g_3 g_4 \frac{R_L}{R_g} - d_p g_2 = \frac{1}{\delta D} \frac{R_L}{R_g} - d_p \frac{\delta}{k_{1,2}^2} \quad (1.83)$$

Therefore, if

$$d_p \frac{\delta}{k_{1,2}^2} > \frac{R_L}{\delta D R_g}, \quad (1.84)$$

then $C_3'' < 0$. As all the parameters in Eq. 1.84 are positive and purely real, the sufficient condition for avoiding negative Y_3 admittance values is

$$d_p \frac{\delta}{k_{1,2}^2} < \frac{R_L}{\delta D R_g}. \quad (1.85)$$

It is important to notice that this inequality is only the sufficient condition for $Y_3 > 0$. Even if $C_3'' < 0$, Y_3 can be positive, if $|E| > |C|$. Unfortunately, both

Term E and Term C contains common and different dependent variables. Their relationship depends on all the input parameters. Hence, in order to calculate the absolute value of both terms and set up the relationship between them would require the direct calculation of the whole Y_3 equation. Hence, if $C_3'' < 0$ then there is no *shorter* way for deciding whether $Y_3 > 0$, or not.

1.6.4 Summary of Conditions for Avoiding Negative and Complex Impedance Values

If parameter $d > \frac{\delta}{2}$ then all impedance values are purely real. The rules for avoiding negative impedance values are a bit more complex.

1. If $Y_{2,3}$ is purely real, then $Y_{2,3} > 0$ without any further condition.
2. If $d_p < 1$ then $Y_2 > 0$ without any further condition. However, if $d_p > 1$ then $Y_2 > 0$ only if the necessary condition is fulfilled

$$U < \frac{U}{2d_p} + 2 \frac{(d_p - 1)}{d_p} J_{2,3}. \quad (1.86)$$

3. The sufficient condition for $Y_3 > 0$ is

$$d_p \frac{\delta}{k_{1,2}^2} < \frac{R_L}{\delta D R_g}. \quad (1.87)$$

1.7 Realization Problems of Matching Networks based on Impedance Inverters

Similarly to the realization problems of admittance inverters in series R-L-C load configurations, impedance inverter parameters calculation may also result in physical realization limits for parallel R-L-C loads. In coupled transmission line structures, the odd- and even-mode impedances must be positive and purely real. As the synthesis process in itself does not prevent non-realizable solutions, I suggest the extended requirements for achieving realizable matching networks. In this thesis section, I present the realization requirements that must be fulfilled for the successful matching of a parallel R-L-C load using an edge coupled transmission line matching network.

1.7.1 Avoiding Complex Coupled Line Impedance Values

The odd- and even-mode impedance values are determined by the four equations below

$$(Z_{0\text{-even}}^a)_{2,3} = \frac{R_L L'_2}{g_0} \tan(\Theta_1) + (R_L M_{2,3} + K_{2,3}), \quad (1.88)$$

$$(Z_{0\text{-odd}}^a)_{2,3} = \frac{R_L L'_2}{g_0} \tan(\Theta_1) + (R_L M_{2,3} - K_{2,3}), \quad (1.89)$$

$$(Z_{0\text{-even}}^b)_{2,3} = \frac{R_L L''_3}{g_0} \tan(\Theta_1) + (R_L M_{2,3} + K_{2,3}), \quad (1.90)$$

$$(Z_{0\text{-odd}}^b)_{2,3} = \frac{R_L L''_3}{g_0} \tan(\Theta_1) + (R_L M_{2,3} - K_{2,3}). \quad (1.91)$$

Unfortunately, nothing prevents a complex transmission line impedance result, therefore all four equations must be analyzed separately. The following boundary conditions are required for further analysis

$$g_0 = 1; \quad R_g, R_L, \delta, k_{1,2}, k_{2,3}, d_p > 0 \text{ and purely real; } \quad \tan(\Theta_1) \geq 0. \quad (1.92)$$

Avoiding complex $(Z_{0\text{-even}}^a)_{2,3}$ value. Starting with the first equation and separating it into two terms A and B and substituting into the equations

$$(Z_{0\text{-even}}^a)_{2,3} = \underbrace{\frac{R_L L'_2}{g_0} \tan(\Theta_1)}_A + \underbrace{(R_L M_{2,3} + K_{2,3})}_B, \quad (1.93)$$

$$A = \frac{R_L}{g_0} \frac{\delta}{k_{1,2}^2} (1 - d_p) \tan(\Theta_1), \quad (1.94)$$

$$B = \sqrt{\underbrace{(K_{2,3})^2}_{B_1} + \underbrace{\left(\frac{R_L \delta d_p (1 - d_p) \tan(\Theta_1)}{k_{1,2}^2 g_0}\right)^2}_{B_2}} + \underbrace{K_{2,3}}_{B_4}. \quad (1.95)$$

Term A is always purely real, while $R_L, g_0, \delta, k_{1,2}, d_p$ are purely real and the tangent function with purely real argument yields purely real value. The two subterms (B_3 and B_4) under Term B require further investigation. The square-root function applied to Term B_3 has either a purely imaginary or purely real result. Parameter $K_{2,3}$ is either purely real or purely imaginary, because the square-root function was applied to purely real values that are multiplied together. If $K_{2,3}$ is purely imaginary there are two possibilities.

1. If $|B_2| > |B_1|$, then $B_3 \geq 0$, therefore $\text{Im}(\sqrt{B_3}) = 0$. Therefore, as B_4 is purely imaginary, $\text{Im}(B) \neq 0$, and this is *not* acceptable.

2. If $|B_2| \leq |B_1|$, then $B_3 \leq 0$. Hence, $\text{Im}(\sqrt{B_3}) \neq 0$ and $\text{Im}(\sqrt{B_3}) \neq -\text{Im}(B_4)$. Therefore, Term B will be purely imaginary and this is *not* acceptable, as well.

Concluding the above, Term B can only be purely real if and only if $K_{2,3}$ is purely real. But how can one determine whether $K_{2,3}$ is purely real? In order to define the constraints for this statement, let me start with the equation of $K_{2,3}$

$$K_{2,3} = R_L \sqrt{\frac{L_2 L_3}{g_2 g_3}} = \sqrt{\frac{\frac{\delta}{k_{1,2}^2} \frac{1}{\delta D} \frac{R_g}{R_L}}{\frac{\delta}{k_{1,2}^2} \frac{k_{1,2}^2}{\delta k_{2,3}^2}}} = \sqrt{\frac{k_{2,3}^2 R_g}{k_{1,2}^2 D}}. \quad (1.96)$$

The Green-coefficients ($k_{1,2}$, $k_{2,3}$) and the generator resistance R_g are purely real and greater than zero. Parameter D is the only that can be negative and thus turn $K_{2,3}$ purely imaginary. Therefore, if $D \geq 0$ then $K_{2,3}$ is purely real. However, $D = 0$ would cause infinite $K_{2,3}$, therefore the appropriate formula for purely real $K_{2,3}$ is $D > 0$.

$$D > 0 \quad \text{if and only if} \quad \frac{d}{\delta \sin\left(\frac{\pi}{2n}\right)} > 1. \quad (1.97)$$

For third-order matching networks (where $n = 3$) this equation is simplified to

$$d > \frac{\delta}{2}. \quad (1.98)$$

Summarizing the above: $K_{2,3}$ *must* be purely real in order to obtain a realizable matching network (fulfills Eq. 1.98). And this leads to non-complex $(Z_{0\text{-even}}^a)_{2,3}$.

Avoiding complex $(Z_{0\text{-odd}}^a)_{2,3}$ value. The calculated odd- and even-mode impedance values only slightly differ. The relationship between them can be expressed as

$$(Z_{0\text{-even}}^a)_{2,3} = (Z_{0\text{-odd}}^a)_{2,3} + 2K_{2,3}. \quad (1.99)$$

For successful realization all impedance values must be purely real (and greater than zero). I previously introduced the requirement for $(Z_{0\text{-even}}^a)_{2,3}$: $K_{2,3}$ must be purely real. With this assumption and Eq. 1.99 I can safely state that the requirement for non-complex $(Z_{0\text{-odd}}^a)_{2,3}$ is exactly the same, as it was for $(Z_{0\text{-even}}^a)_{2,3}$:

$$d > \frac{\delta}{2}. \quad (1.100)$$

Avoiding complex $(Z_{0\text{-even}}^b)_{2,3}$ value. The equation for $(Z_{0\text{-even}}^b)_{2,3}$ must be analyzed separately for avoiding complex impedance values. I'm going to use the

assumption of $K_{2,3}$ being purely real, as before.

$$(Z_{0\text{-even}}^b)_{2,3} = \underbrace{\frac{R_L L_3''}{g_0} \tan(\Theta_1)}_A + \underbrace{(R_L M_{2,3} + K_{2,3})}_B. \quad (1.101)$$

Term B is purely real, as $K_{2,3}$ is purely real. Term A represents the scope of this analysis from here. R_L, g_0 is purely real, as well as the result of the tangent function. Parameter L_3'' is expressed as

$$L_3'' = \frac{R_g}{\delta D R_L} - \frac{\delta d_p (1 - d_p)}{k_{1,2}^2}. \quad (1.102)$$

The parameters of L_3'' are all purely real, hence Term A is purely real. To sum up, $(Z_{0\text{-even}}^b)_{2,3}$ is purely real if $K_{2,3}$ is purely real.

Avoiding complex $(Z_{0\text{-odd}}^b)_{2,3}$ value. Finally, $(Z_{0\text{-odd}}^b)_{2,3}$ is expressed using $(Z_{0\text{-even}}^b)_{2,3}$

$$(Z_{0\text{-even}}^b)_{2,3} = (Z_{0\text{-odd}}^b)_{2,3} + 2 K_{2,3}. \quad (1.103)$$

Similarly, if $(Z_{0\text{-even}}^b)_{2,3}$ and $K_{2,3}$ is purely real then $(Z_{0\text{-odd}}^b)_{2,3}$ is also purely real.

Summary of conditions. I introduced the fundamental requirements for avoiding complex transmission line impedances for third-order matching networks with impedance inverters. It turned out from the equations that the necessary condition for avoiding complex impedance values in third-order matching networks is

$$d > \frac{\delta}{2}. \quad (1.104)$$

This result shows good correspondence with the constraints required for admittance inverters used in series R-L-C load configurations.

1.7.2 Requirements for Positive Coupled Line Impedance Values

For edge-coupled transmission lines it is not enough that the odd- and even-mode impedances are purely real. They also must be positive. Checking whether zero, or negative impedance values can occur requires deeper analysis. This is the scope of this section. The previously defined constraint for impedance values not being complex is considered fulfilled from now on: $\text{Im}(K_{2,3}) = 0$ and $K_{2,3} \geq 0$ (as seen in Sec. 1.5 and Sec. 1.7.1). All other parameter restrictions are the same as defined previously in Sec. 1.7.

Conditions for $(Z_{0\text{-even}}^a)_{2,3} > 0$.

$$(Z_{0\text{-even}}^a)_{2,3} = \underbrace{\frac{R_L L'_2}{g_0} \tan(\Theta_1)}_A + \underbrace{(R_L M_{2,3} + K_{2,3})}_B \quad (1.105)$$

For adequate analysis, Term A and Term B is separated. Term $B \geq 0$, as $K_{2,3}$ and therefore $M_{2,3} \geq 0$. R_L and $\tan(\Theta_1) \geq 0$ in Term A is positive and purely real, hence only L'_2 must be investigated separately.

$$L'_2 = (1 - d_p) \frac{\delta}{k_{1,2}^2}. \quad (1.106)$$

Clearly, if $0 \leq d_p \leq 1$ Term A remains positive. However, if $d_p > 1$, then Term A turns negative. As $g_0 = 1$, the question is whether

$$|L'_2 \tan(\Theta_1)| < \left| \left(M_{2,3} + \frac{K_{2,3}}{R_L} \right) \right| ? \quad (1.107)$$

From the equation of $M_{2,3}$ it is clear, that $M_{2,3} > L''_2 \tan(\Theta_1)$. The relationship between L''_2 and L'_2 is as follows

$$L'_2 = \frac{\delta}{k_{1,2}^2} (1 - d_p), \quad L''_2 = \frac{\delta}{k_{1,2}^2} d_p. \quad (1.108)$$

If $d_p > 1$ then $|L''_2 \tan(\Theta_1)| > |L'_2 \tan(\Theta_1)|$, therefore the questioned equation Eq. 1.107 holds. Even if Term A is negative due to $d_p > 1$ its' absolute value is always smaller than Term B , hence $(Z_{0\text{-even}}^a)_{2,3}$ *cannot* be negative. Therefore, for any $d_p > 0$ values $(Z_{0\text{-even}}^a)_{2,3}$ is unconditionally greater than zero.

Conditions for $(Z_{0\text{-odd}}^a)_{2,3} > 0$. As all odd- and even-mode impedance values must be positive I assume that $(Z_{0\text{-even}}^a)_{2,3} > 0$,

$$(Z_{0\text{-odd}}^a)_{2,3} = \underbrace{\frac{R_L L'_2}{g_0} \tan(\Theta_1)}_A + \underbrace{(R_L M_{2,3} - K_{2,3})}_B. \quad (1.109)$$

Term $B > 0$. Term $A \geq 0$ if $0 \leq d_p \leq 1$, otherwise Term A is negative. The sufficient condition for positive $(Z_{0\text{-odd}}^a)_{2,3}$ is

$$0 < d_p \leq 1. \quad (1.110)$$

However, what happens when $d_p > 1$? This leads to negative Term A and it must be analyzed separately. A new auxiliary parameter is declared for this calculation

$$U = R_L \tan(\Theta_1) \frac{\delta}{k_{1,2}^2}. \quad (1.111)$$

If $d_p > 1$, then

$$-(d_p - 1) U + \sqrt{K_{2,3}^2 + (d_p U)^2} - K_{2,3} > 0? \quad (1.112)$$

Rearranging the two sides, and raising to the square

$$K_{2,3}^2 + (d_p U)^2 > (d_p^2 - 2 d_p + 1) U^2 + 2 (d_p - 1) U K_{2,3} + K_{2,3}^2, \quad (1.113)$$

$$0 > (-2 d_p + 1) U + 2 (d_p - 1) K_{2,3}, \quad (1.114)$$

$$2 d_p (U - K_{2,3}) > U - 2 K_{2,3}, \quad (1.115)$$

$$d_p > \frac{U - 2 K_{2,3}}{2 (U - K_{2,3})}. \quad (1.116)$$

This inequality must be separated into two cases:

1. If $U > K_{2,3}$ the inequality is fulfilled for any $d_p > 1$ value, hence $(Z_{0\text{-odd}}^a)_{2,3} > 0$.
2. If $U < K_{2,3}$ then the maximum d_p value is restricted

$$1 < d_p < \frac{U - 2 K_{2,3}}{2 (U - K_{2,3})}. \quad (1.117)$$

The conditions for $(Z_{0\text{-odd}}^a)_{2,3} > 0$ are summarized as follows.

1. If $0 < d_p \leq 1$ then $(Z_{0\text{-odd}}^a)_{2,3} > 0$ without any further condition.
2. If $d_p > 1$ and $U > K_{2,3}$ then $(Z_{0\text{-odd}}^a)_{2,3} > 0$ without any further condition.
3. If $d_p > 1$ and $U < K_{2,3}$ then $(Z_{0\text{-odd}}^a)_{2,3} > 0$, if and only if

$$1 < d_p < \frac{U - 2 K_{2,3}}{2 (U - K_{2,3})}. \quad (1.118)$$

Conditions for $(Z_{0\text{-even}}^b)_{2,3} > 0$.

$$(Z_{0\text{-even}}^b)_{2,3} = \underbrace{\frac{R_L L_3''}{g_0} \tan(\Theta_1)}_A + \underbrace{(R_L M_{2,3} + K_{2,3})}_B. \quad (1.119)$$

Yet again, $B > 0$ and only L_3'' should be analyzed

$$L_3'' = \frac{R_g}{\delta D R_L} - \frac{\delta d_p}{k_{1,2}^2}. \quad (1.120)$$

The next question whether,

$$\begin{aligned} & - R_L d_p \frac{\delta}{k_{1,2}^2} \tan(\Theta_1) + \frac{R_g \tan(\Theta_1)}{\delta D} + \dots \\ & \dots + \sqrt{K_{2,3}^2 + \left(R_L d_p \frac{\delta}{k_{1,2}^2} \tan(\Theta_1) \right)^2} + K_{2,3} > 0 \quad ? \quad (1.121) \end{aligned}$$

And as,

$$\sqrt{K_{2,3}^2 + \left(R_L d_p \frac{\delta}{k_{1,2}^2} \tan(\Theta_1)\right)^2} > \left| -R_L d_p \frac{\delta}{k_{1,2}^2} \tan(\Theta_1) \right| \quad (1.122)$$

and all other terms are positive, the condition is fulfilled without any further constraint. $(Z_{0\text{-even}}^b)_{2,3}$ cannot be less than zero.

Conditions for $(Z_{0\text{-odd}}^b)_{2,3} > 0$.

$$(Z_{0\text{-odd}}^b)_{2,3} = \frac{R_L L_3''}{g_0} \tan(\Theta_1) + (R_L M_{2,3} - K_{2,3}). \quad (1.123)$$

This equation can be reformulated as

$$(Z_{0\text{-odd}}^b)_{2,3} = (Z_{0\text{-even}}^b)_{2,3} - 2 K_{2,3}. \quad (1.124)$$

For this reason, it is enough to check whether

$$(Z_{0\text{-even}}^b)_{2,3} > 2 K_{2,3} \quad ? \quad (1.125)$$

If this condition is fulfilled, then $(Z_{0\text{-odd}}^b)_{2,3} > 0$.

Summary of conditions. The complete system of constraints for the coupled line impedance values to be positive is presented here.

1. $(Z_{0\text{-even}}^a)_{2,3} > 0$ is unconditionally fulfilled for any $d_p > 0$ values.
2. $(Z_{0\text{-odd}}^a)_{2,3} > 0$
 - if $0 < d_p \leq 1$, then $(Z_{0\text{-even}}^a)_{2,3} > 0$, or
 - if $d_p > 1$ and $U > K_{2,3}$ then $(Z_{0\text{-even}}^a)_{2,3} > 0$, where $U = R_L \tan(\Theta_1) \frac{\delta}{k_{1,2}^2}$,
or
 - if $d_p > 1$ and $U < K_{2,3}$ and $1 < d_p < \frac{U - 2K_{2,3}}{2(U - K_{2,3})}$ then $(Z_{0\text{-even}}^a)_{2,3} > 0$.
3. $(Z_{0\text{-even}}^b)_{2,3} > 0$ is unconditionally fulfilled for any $d_p > 0$ values.
4. $(Z_{0\text{-odd}}^b)_{2,3} > 0$ if $(Z_{0\text{-even}}^b)_{2,3} > 2 K_{2,3}$.

1.7.3 Suggested Parameter Values for Avoiding Negative or Complex Coupled Line Impedance Values

If parameter $d > \frac{\delta}{2}$ then all impedance values are purely real. This result is similar to the one I got at the admittance inverter analysis. The rules for avoiding negative impedance values are a bit more complex, therefore it can be found summarized at the end of Sec. 1.7.2. As a rule of thumb, parameter d_p should be less than or equal to 1. But this is neither a necessary, nor a sufficient condition.

1.8 An Example Application of the Realization Limits in Matching Tasks

In the previous sections, I presented the realization problems and how to avoid them in impedance matching tasks. This section discusses an example use case of the realization constraints I suggested, for matching networks with admittance inverters. I present a new automated matching algorithm that contains those realization constraints I described earlier. The algorithm only requires the minimal number of input parameters, easing the efficient calculation.

1.8.1 Automated Matching of Series R-L-C loads

The original Bode-Fano method and admittance inverter synthesis requires the following input parameters:

- f_c - center frequency,
- b - relative matched bandwidth,
- b_{user} - user defined target matching bandwidth,
- R_L - load resistance,
- R_g - generator resistance,
- L/C - load inductance or capacitance,
- d_p - free parameter,
- r - Chebyshev ripple factor.

The output values of the synthesis are the transmission line impedances. If the synthesis provides an adequate result, the matching quality (i.e input reflection function) must be checked by implementing the matching network combined with the source and load into a microwave simulation software. If there are no realization related problems, the matching process is considered successful. If the synthesis fails during the process, another iteration is required with modified parameters. However, the Bode-Fano synthesis process contains some freely adjustable parameters (d_p , r), for which the values are not exactly defined, only the interval in which they must fall. Therefore, the user of the Bode-Fano algorithm must reiterate many times if the starting parameter values are not well chosen. This is a bad practice and there is a way to handle this better.

The matching network design task can be integrated into an iterative algorithm. Generally, the aim of the task is to match a complex load to purely real generator impedance on a specified relative bandwidth around a center frequency, with a predefined highest allowed input reflection coefficient (S_{11} or Γ_{limit}). My aim is to create an iterative algorithm that is able to find the best realizable matching network for the application, among a wide range of input parameter values.

At the beginning, one has to define the target matching details such as: center frequency, bandwidth, load, generator impedances, target S_{11} value etc. The iterative approach contains five fixed and three variable input parameters. The fixed parameters are: f_c , b_{user} , R_g , R_L , L ; the variable parameters are: b , d_p , r . The reason why parameter b_{user} is used in the iterative algorithm is the following. The Bode-Fano method may not give acceptable results when it is ran with the aimed target bandwidth. There are situations when a larger bandwidth parameter results in a realizable network. Therefore, those solutions must not be excluded from the set of realizable networks. This is the reason why parameter b is adjusted ($b_{\text{user}} < b < 2$).

The iteration runs through the whole number of b , d_p , r combinations and synthesizes the low-pass filter prototype networks. Each cycle contains two realization limit checkpoints (pre- and post-admittance inverter synthesis) that filters out all non-realizable networks based on constraints I presented in Sec. 1.6. If the synthesized network is realizable, the matching network values are saved into the row of a matrix.

The algorithm runs until all realizable networks based on the parameter combinations are found. The range of these variable parameters depend on the aims of the matching network. In this case these parameters were chosen: $0.01 \leq b < 2$, $0 \leq d_p < 1$ and $10^{-6} \leq r \leq 1$. After the calculation, only the realizable networks are remaining, let their number be N . The next task is to rate and qualify the remaining matching networks based on their input reflection functions.

The quality of the input reflection function is generally evaluated by the matching network designer, manually. Instead, due to the potentially high number of acceptable results, I introduced a quantity for rating the Quality Of Matching: QOM. With this quantity, it is possible to compare multiple input reflection results (multiple matching networks) and it aids the systematic search of the best matching network for the defined target.

The last step is to find out which matching network provided the best result. The

rating function for this decision is defined as

$$\text{QOM}(k) = \sum_{i=f_c-b/2}^{f_c+b/2} |S_{11}(i)|_k \quad k = 1 \dots N, \quad (1.126)$$

where QOM stands for quality of matching. The QOM function sums the absolute value of the discretized input reflection function $S_{11}(i)$, for the aimed bandwidth between $f_c - b/2$ and $f_c + b/2$. Naturally, the best result is represented by the lowest QOM value. As part of the optimization process, the method filters out all solutions where the input reflection function breaches the target matched bandwidth window. This breach occurs if the matched input reflection function value is above the target reflection value in any of the frequency points in the matched bandwidth (see Fig. 1.4). The target of the process is to find

$$K = \underset{k \in \{1 \dots N\}}{\text{arg min}} \{ \text{QOM}(k) \}, \quad (1.127)$$

where K is the index of the best performing matching network based on the QOM value. After K is obtained, the last task is to find the matching network with index K and the element parameters in the matching network matrix that provides the solution. The complete matching algorithm is shown as a complete block diagram in Fig. 1.5.

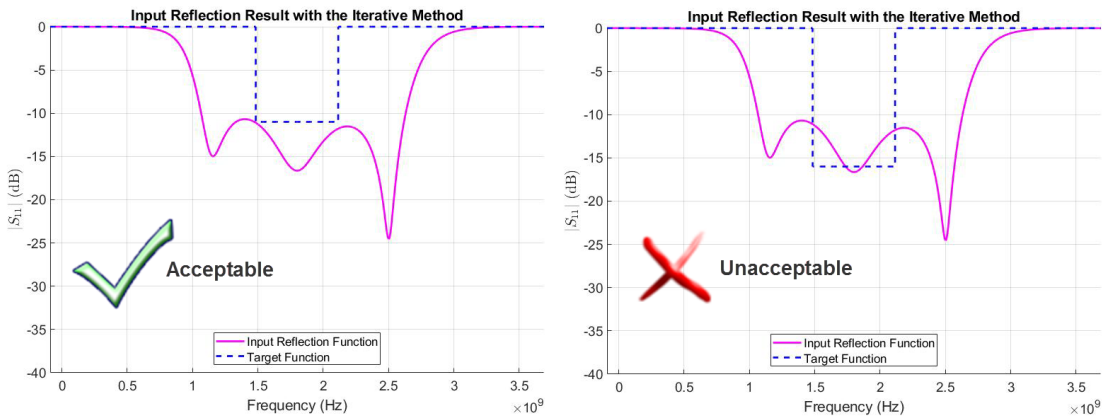


Figure 1.4: The dashed blue function represents the target reflection window, the input reflection coefficient as a function of frequency is shown in magenta.

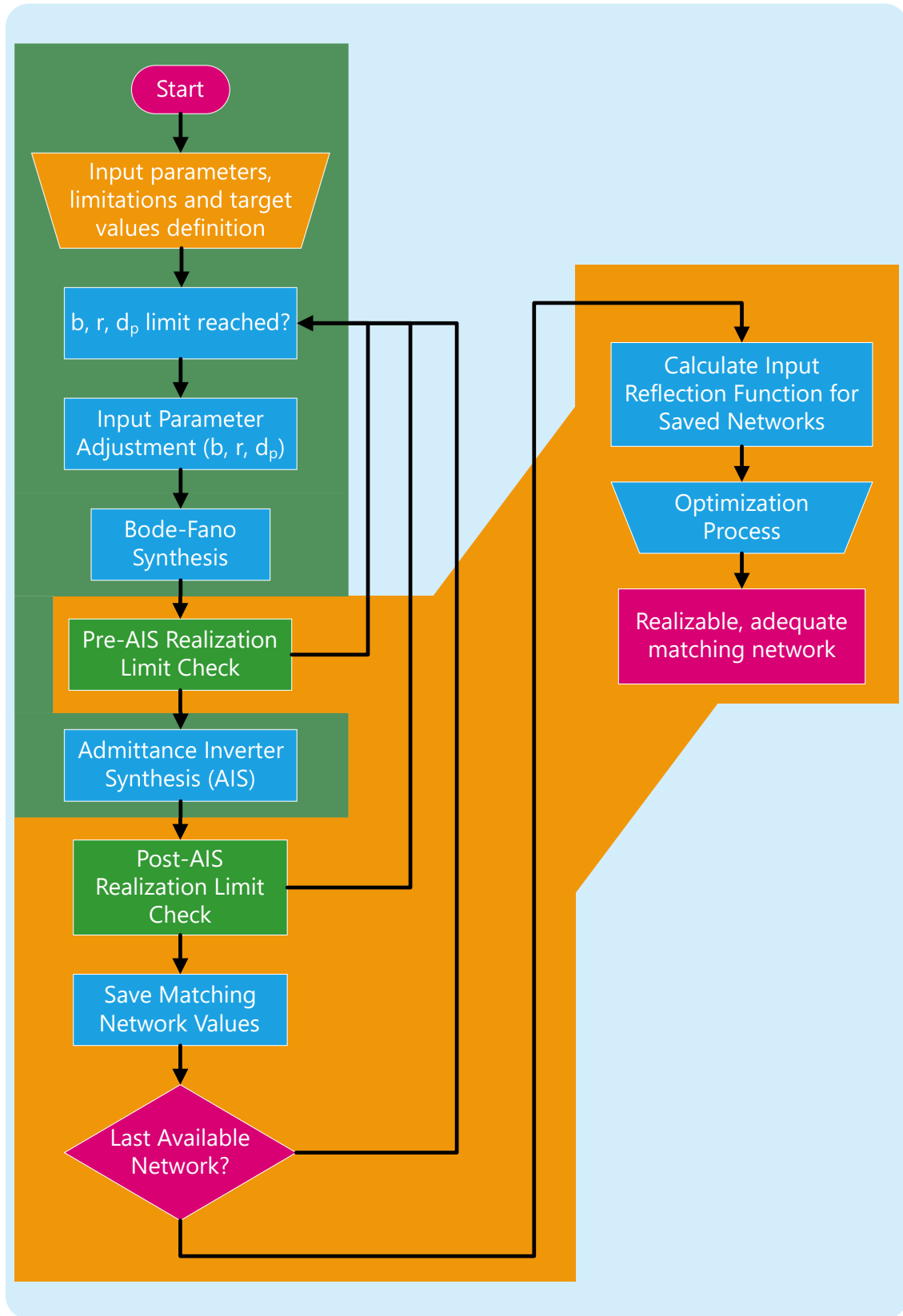


Figure 1.5: Block-diagram of the iterative matching process: Steps highlighted with green color are part of the original Bode-Fano synthesis process, orange colored segments are the ones proposed as part of the iterative algorithm.

1.8.2 Series R-L-C Load Matching with the Iterative Algorithm

The iterative algorithm needs specific parameter ranges defined in Tab. 1.2.

Table 1.2: Input parameters for the series R-L matching task with the iterative method

Center Frequency	2.4 GHz
Relative Bandwidth	30...100 %
Target Bandwidth (b_{user})	30 %
Generator Impedance	50 Ω
Load Resistance	20 Ω
Load Inductance	2 nH
Load Capacitance	2.2 pF
Input Reflection Goal	≤ -10 dB
Load Type	Series R-L-C
Chebyshev Ripple (r)	$10^{-8} \dots 1$
d_p	0 ... 1

The iterative method runs in three nested for-cycles (for parameters b , d_p , r) and each cycle has variable number of iteration steps. As a good starting value all cycle iteration steps were chosen to be 100, therefore the whole number of iteration steps are 100^3 . The iterative process contains two checkpoints (Pre-AIS and Post-AIS) where the physical and practical realization limits are checked and non-realizable results are filtered out (practically realizable impedance values must be $15 \Omega < Z < 150 \Omega$). In this unique case the number of realizable networks was only 5.4 % of the original 100^3 . Therefore, 94.6 % of the available networks are filtered out before any further calculations are started. This significantly helps the speed of calculation. The remaining realizable matching networks are collected and the matching quality is tested by calculating the input reflection function for each remaining case (QOM values). The input reflection functions for the realizable networks were calculated and the optimization process successfully found acceptable results. The parameters of the best matching network calculated with the iterative method are: $b = 0.69$, $d_p = 0.554$, $r = 0.0739$. The rest of the calculated parameters are shown in Tab. 1.3 and Tab. 1.4. A possible realization of the matching network is shown in Fig. 1.7. The final matching network's input reflection function results are shown in Fig. 1.6. The algorithm found a realizable matching network which provides the best result for the target bandwidth (b_{user}). However, this result was found with the original algorithm when the relative bandwidth (b) parameter value was 0.69. The most

Table 1.3: Matching network parameters and low-pass filter prototype values calculated with the iterative algorithm.

Q	δ	Γ_{\max}	d	$k_{1,2}$	$k_{2,3}$	g_0	g_1	g_2	g_3	g_4
1.51	0.57	-24.6 dB	0.44	0.72	0.69	1	1.74	1.10	1.89	1.28

Table 1.4: The calculated optimized matching network impedance values

Z_2	Z_3	$Z_{2,3}$
15.1Ω	148.9Ω	33.4Ω

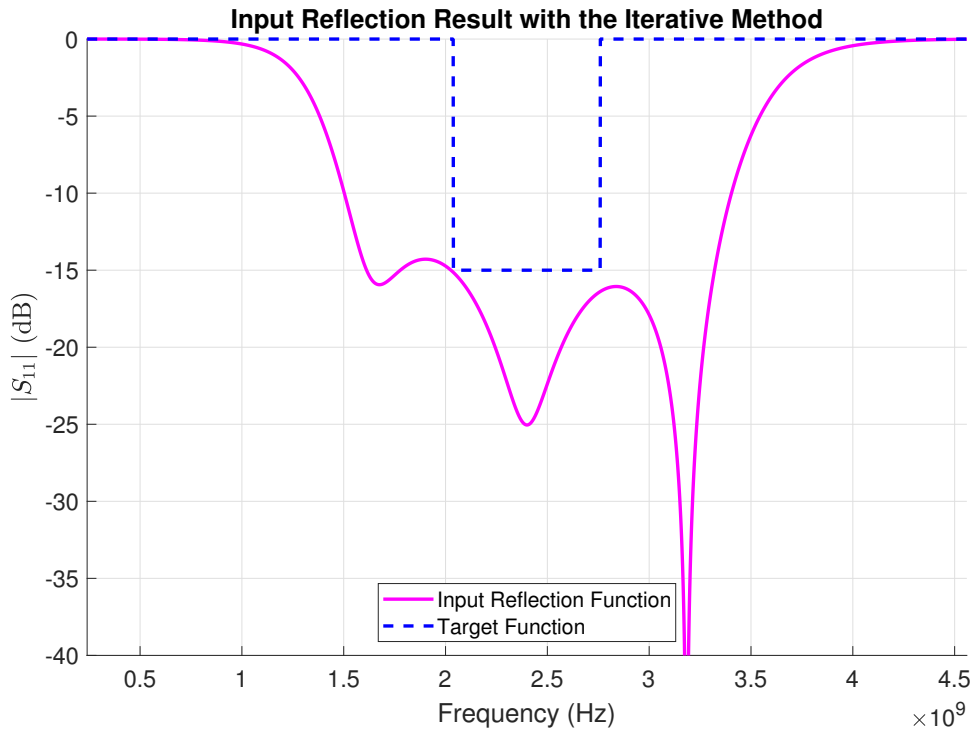


Figure 1.6: Series R-L load matching task - Calculated input reflection function using the proposed iterative method for the matching network. The blue dashed function shows the target best matching window, in which the input reflection function fits well. The iterative algorithm successfully found the best solution.

important benefit of the iterative algorithm is that it provides the best matching network with the available parameters. It is not limited to a single set of parameter combinations like the original method. Moreover, it only yields realizable matching networks. Therefore, one of the key problems of the original Bode-Fano matching process is solved: even if the initial values of the freely adjustable input parameters d_p and r are arbitrarily chosen, the algorithm is able to find an acceptable solution, if it exists with the predefined constraints.

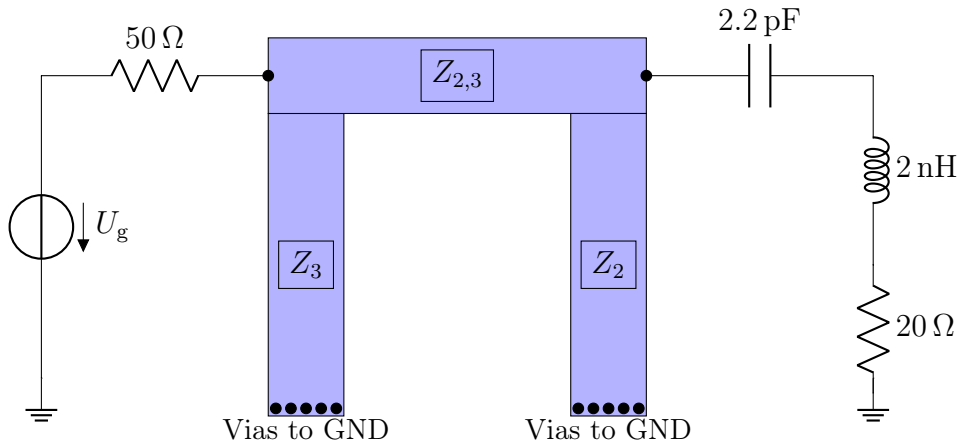


Figure 1.7: The schematic of the matching network with shorted quarter-wave shunt stubs in a microstrip realization.

1.9 Application Limitations of Analytical Matching

The analytical matching method presented in Sec. 1.5 is only capable of matching loads that are characterized as single-reactance models. For instance, first-order resonant structures are good candidates for matching to the source (e.g. resonant antenna). Still, the matching quality and limitations presented in the previous sections tighten the range of application, even if they are modeled as a single-reactance. A good example is an antenna that has significantly lower physical dimensions ($\lambda_g/10$ or even $\lambda_g/100$) compared to the wavelength of operation. Generally, such antennas suffer from:

- low radiation resistance, hence bad radiation efficiency
- distorted farfield pattern, weak gain
- high quality factor, narrow bandwidth of operation.

Such antennas are found in a wide range of commercial devices: smartphones, smartwatches, tablets, Wi-Fi dongles, RFID cards etc. One of the most interesting and active areas of research regarding small antennas are on-chip antennas (OCA). Due to the high level of integration in compact electrical devices, antennas had to fit in restricted spatial dimensions. This demand led to the large-scale development of antenna miniaturization techniques. On-chip antennas took the level of integration to extremes. For example, an RFID chip that operates in the ISM band (either 920 MHz or 2.4 GHz) has physical dimensions close to the millimeter range. These chips require additional booster antennas, for better radiation properties, however booster antennas significantly enlarge the physical antenna size. Contrary to the booster

antenna approach, by integrating the antenna onto the chip itself the physical space required for the antenna is reduced dramatically. This on-chip approach often prevents engineers from using conventional impedance matching techniques, like the Bode-Fano method as there would not be enough space to place the lumped element or transmission line matching network onto the chip. Thus, alternative matching and resonant frequency lowering techniques are required.

1.9.1 On-chip Antenna Design and Matching Problems in UHF-RFID Applications

Many of these applied miniaturization approaches utilize bent [25], meandered antenna designs [26], or booster antennas [27]. However, these procedures are only available if the antenna physical dimensions allow this [28]. The OCA design method requires a different approach for determining antenna performance and radiation parameters in simulation. Although, there is a well-formed measurement solution for measuring antenna radiation pattern for UHF RFID antennas, presented in [29], obtaining the appropriate antenna parameter results in simulation domain for such ultra small scale antennas require further investigation.

Definition of small antennas. Starting out with an important definition issue: when is it appropriate to describe an antenna as *small*? The most commonly used expression for small antennas in scientific literature is: Electrically Small Antennas (ESA). This refers to the fact that the best practice is to compare antenna physical dimensions to the wavelength of operation λ_g . A well-known definition for ESA is having dimensions in the range

$$k a \leq 0.5, \tag{1.128}$$

where parameter $k = 2\pi/\lambda_g$ and parameter a is the half-length of a thin linear dipole [30]. There is an alternative version of this definition where a is the radius of a sphere surrounding the antenna structure. An important subset of ESA's are the Physically Constrained Small Antennas (PCSA) [31]. A PCSA is an antenna that has at least one dimension which fulfills the ESA dimension criteria set in Eq. 1.128. An adequate example of this is a conventional planar patch antenna lying in the X-Y plane. The planar patch has got much smaller dimensions compared to the operating wavelength in the Z-direction (in the range of $\lambda/50$). A Physically Small Antenna (PSA) only refers to the physical dimensions of the antenna, regardless of the operation frequency, therefore it is not the best way to describe the quality of antenna.

The purpose and principles of miniaturized antennas. The concept of antenna downsizing spread at an unexpected rate, as telecommunication devices began to shrink in terms of physical dimensions. Handheld platforms require efficient design of electrically small antennas. The smaller the volume occupied by the antennas from the space inside or on the device, the better. This enforces antenna designers to more-or-less sacrifice antenna performance in exchange for reduced antenna size. The straightforward solution would be the linear downscaling of antenna dimensions. Unfortunately, this would result in uneven current distribution on the antenna geometry, reduced radiation efficiency, higher resonance frequency, etc.; in short: dramatically decreased overall antenna performance. Therefore efficient downsizing requires a range of special geometry transformations (bending, meandering etc.) or other solutions (slow-wave or metamaterial structure etc.). An adequate way of lowering the resonance frequency of an antenna (while maintaining all physical dimensions) is to compose the antenna with a Slow-Wave (SW) structure. In a SW structure, the electromagnetic wave's propagation speed v_g is lower than the speed of light c . This implies that an antenna composed with a Slow-Wave structure will exhibit lower resonance frequency. A common technique for creating such structure is to modify the antenna geometry, in order to extend the total current path. For example, meandered line structure [32], a fractal structure [33], slots in a metal plane, etc. Not only do these solutions lower the resonance frequency, but if properly designed they also fill the space dedicated to the antenna structure efficiently. There are some planar geometry structures (Peano [34] and Hilbert curves [35], depicted in Fig. 1.8 and Fig. 1.9) that efficiently fill the largest planar space available. Therefore, the length of the antenna may be longer, yielding resonant behavior. Antennas composed of conjugate component structures are also promising candidates for realizing efficient electrically small antennas (shown in Fig. 1.10). The theory of operation behind complementary structures is that their capacitive and inductive components partially compensate each other, yielding a better radiation performance and frequency independent behavior. This principle was thoroughly investigated by Hohlfeld and Cohen. Being self-complementary and origin symmetrical form together the frequency independent behavior in antennas [36].

Contrary to the efforts made to maintain antenna performance by employing proper downsizing methods, miniature antennas will most likely suffer from at least some of the following disadvantageous properties. Apart from the above, a key property of the antenna always decreases during the downsizing process: the effective antenna length. This parameter is in close relation to the amount of electromagnetic energy

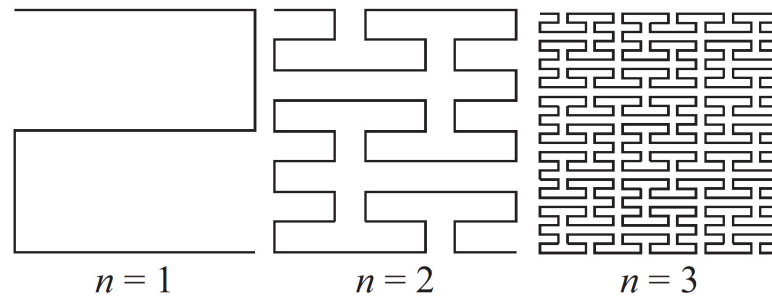


Figure 1.8: First, second and third-order Peano curves [34].

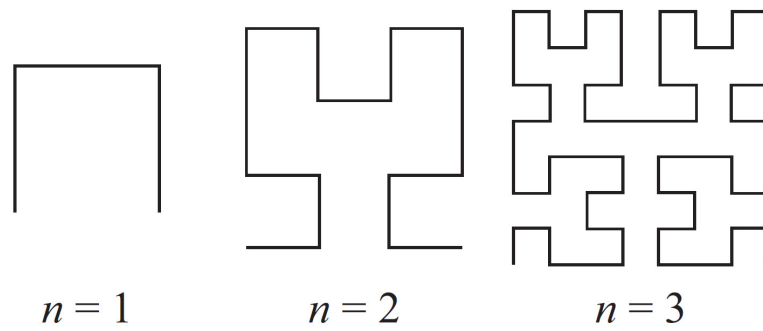


Figure 1.9: First, second and third-order Hilbert curves [35].



Figure 1.10: Self-complementary planar spiral antenna structure [31].

that can be extracted from the field surrounding the antenna. The larger the effective length, the better the antenna efficiency is. In case of ultra-small form factor antennas (where $ka \leq 0.5$) it is a reasonable practice to describe antenna performance with quantities in close relation to the effective length.

An Ultra-Small Form Factor passive RFID chip with OCA. RFID is a wireless technology used to transmit digital data between stationary devices (commonly referred to as: readers) and one or more moving objects (referred to as: tags). RFID links operate in a wide range of frequency bands. The expression *passive* in RFID systems refers to an RFID tag that lacks internal power source. The tag gains energy from the rectified power of the incident absorbed EM wave emitted by the reader. The power rectification process takes place inside the RFID chip that is attached to the RFID tag antenna. The communication process in passive RFID links is the following: the reader transmits power towards the passive tag's antenna, providing enough power for the tag chip to start the operation. The chip processes the incoming data and sends the data requested by the reader. The transmission happens by periodically changing the output impedance of the tag chip (in correspondence with the transmitted data), thus either reflecting, or absorbing the incident EM wave generated by the reader. This principle is similar to other reflection based detection techniques and it was first introduced by Stockman [37] who described it as: "Communication by means of reflected power". This type of transmission is not designed for high data rates, but data speed is not necessarily the most important property of RFID communication. The crucial property of a passive RFID link, is the largest available transmission distance between the tag and reader. As this property vastly depends on the performance of the tag antenna, I'm going to focus on improving the tag antenna performance. The antenna tag design for simulations is based on a commercially available RFID tag. The Ultra-Small Package Tag (USPT) by Hitachi Chemical Co. Ltd. is a complete passive RFID tag with an Impinj Monza 5 CMOS chip and integrated tag antenna. Regarding physical dimensions, the tag itself is 2.5 x 2.5 x 0.4 mm [38] and its operating frequency is 920 MHz. The tag antenna on the device complies with the definition of being electrically small. The parameter ka is calculated with the spherical condition introduced previously

$$ka = \frac{2\pi}{\lambda}a \approx 0.068. \quad (1.129)$$

This antenna is considered electrically small since the condition defined in Eq. 1.129 is fulfilled. The antenna structure (depicted in Fig. 1.11) is an orthogonal designed

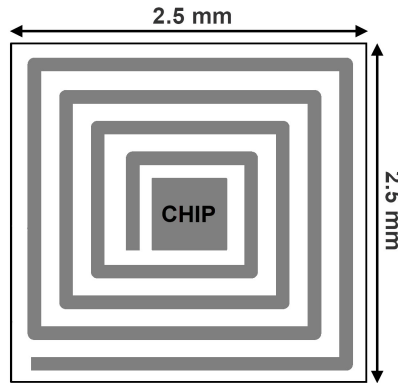


Figure 1.11: Top view of the RFID chip with the tag antenna surrounding it. [39]

planar spiral loop antenna. The center of the tag contains the RFID chip, and the tag antenna surrounds it in the planar domain. Strictly speaking, this spiral tag antenna is not an OCA, however as its dimensions are very close to the chip dimensions, therefore it can be considered as an OCA. Unfortunately, the manufacturer does not provide public, reliable simulation and measurement results related to the tag antenna performance. Therefore, the simulation presented here is based on the values found in the datasheet that is accessible on the manufacturer's website [39]. The manufacturer provides application notes for designing booster antennas for the device, however adding a booster structure would significantly increase the overall physical size of the device. My aim is to optimize the tag antenna performance by matching the antenna to the source better, via changes in antenna geometry and surrounding material. The first antenna simulation is based on the datasheet values of the USPT tag on-chip antenna.

The original USPT OCA simulation. CST Microwave Studio 2018 was used for the simulation tasks. The three-dimensional model of the USPT is illustrated in Fig. 1.12. The model lies in the X-Y plane. The discrete port excitation of the antenna structure is located on the bottom side of the chip at the endpoints of the spiral. The RFID chip manufacturer (Impinj) provides a wideband circuit model (shown in Fig. 1.13) for the chip's RF output impedance. This is considered in the discrete port parameters. In this construction, the on-chip antenna is terminated with the circuit shown Fig. 1.13.

Since the antenna is terminated with the circuit model in Fig. 1.13 this load is modeled using lumped elements, directly attached to the discrete port. The built-in FR-4 substrate model ($\epsilon_r = 4.5$, $\tan \delta = 0.025$) was utilized during simulation of the

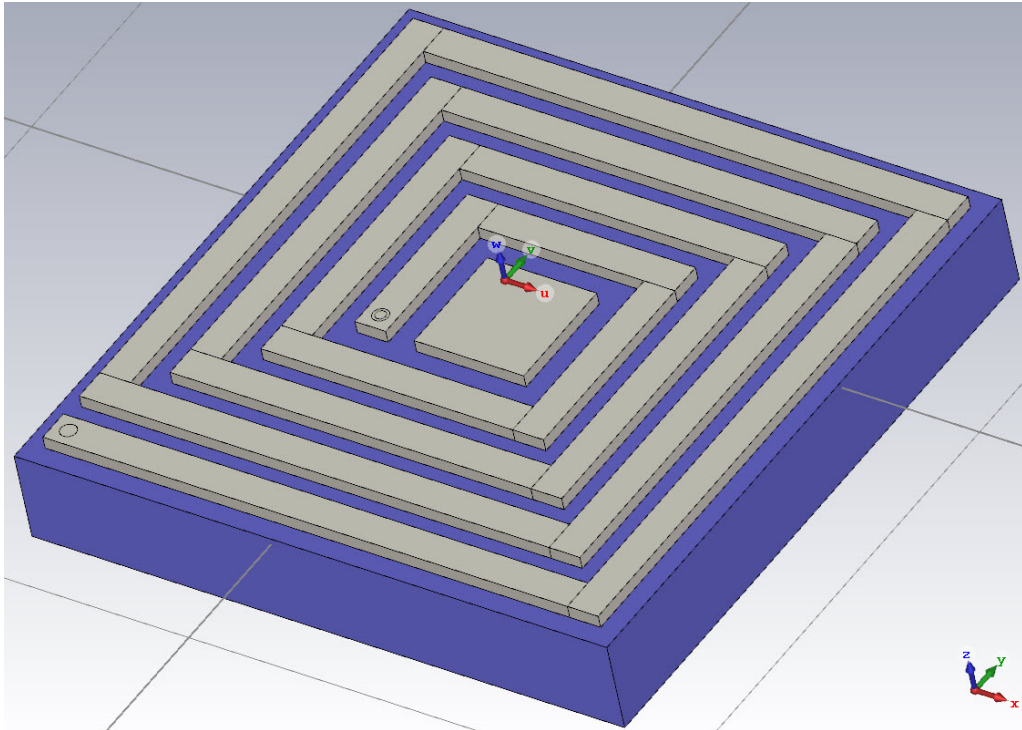


Figure 1.12: 3D model of the USPT in CST Microwave Studio 2018.

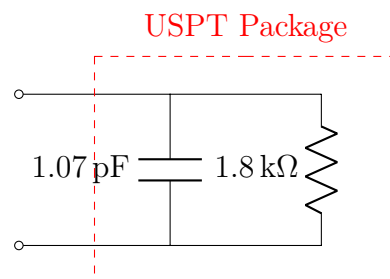


Figure 1.13: The USPT wideband circuit model.

tag antenna, based on the information provided by the manufacturer. The top copper layer width was $35\ \mu\text{m}$ and modeled as a Perfect Electric Conductor (PEC). CST Microwave Studio offers a frequency domain solver (F-solver), which is commonly used for high frequency problems. This F-solver was used to obtain simulation results. The on-chip antenna performance was evaluated by the built-in power flow field-monitor in CST. The power flow field-monitor calculates the magnitude of the absolute value of the Poynting vector on a dedicated curve, or a face above the antenna structure. Instead of the far-field monitors, it's an advantageous practice to use a power flow monitor in this situation. Due to the extreme size ratio between antenna dimensions and operating wavelength, a major problem arises. Accurate far-field calculations require a bounding box with planes at least $\lambda_g/2$ apart from the structure. However, this would result in a huge volume calculation domain with dense meshing, hence large computational load. For this reason, far-field calculations were omitted. Furthermore, during the RFID transmission in such small sized on-chip antennas, the energy for the passive RFID tag is coupled through the near-field inductive component of the reader's antenna. For this reason, near field dependent quantities are used for adequate antenna performance comparison.

Fig. 1.14 shows the amount of power flow, perpendicular to the X-Y plane, at $Z=5\ \text{mm}$. For an exact comparison, two cutting planes were applied and the power flow amount was evaluated along the X and Y axis (denoted with dashed black lines on). These cutting plane values are depicted in Fig. 1.15 and Fig. 1.16. These simulation results show that the absolute maximum value of the power flow is approximately $250\ \text{VA}/\text{m}^2$. This power flow value is saved as a reference. The antenna input impedance (Z_{in}) was calculated at the excitation port: $Z_{\text{in}} = 41 - 2300\ \text{j}\Omega$ and the input reflection coefficient is: $S_{11} = -0.096\ \text{dB}$. This impedance value is not even close to the chip's output impedance. Unfortunately, in case of such on-chip antennas conventional impedance matching networks cannot be implemented. As the space for external lumped or transmission line elements are substantially restricted, adding large lumped elements or quarter-wavelength stubs or coupled lines are not an option. The antenna geometry and surrounding material must be altered instead.

Alternative On-Chip Antenna Design with Slow-wave Structure Instead of matching the original antenna with lumped or transmission line elements, an alternative customized three-dimensional multi-layer spiral antenna was designed. The base size of the antenna was identical, but the substrate width was increased to three layers ($300\ \mu\text{m}$ each), containing an evolving spiral. The new antenna followed

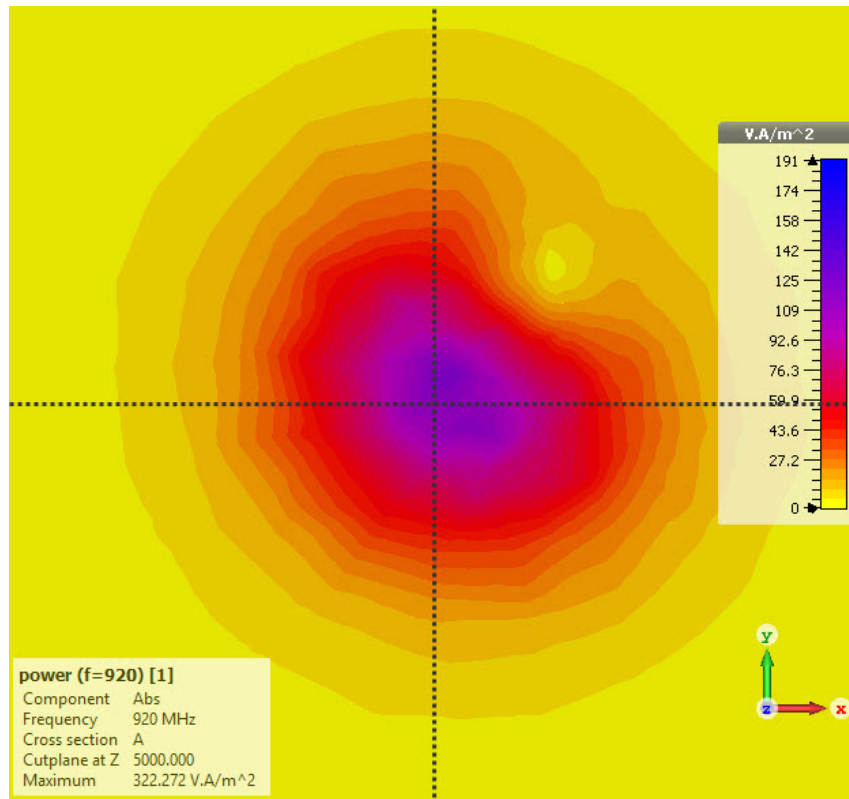


Figure 1.14: Power flow parallel to the X-Y plane, at Z=5 mm.

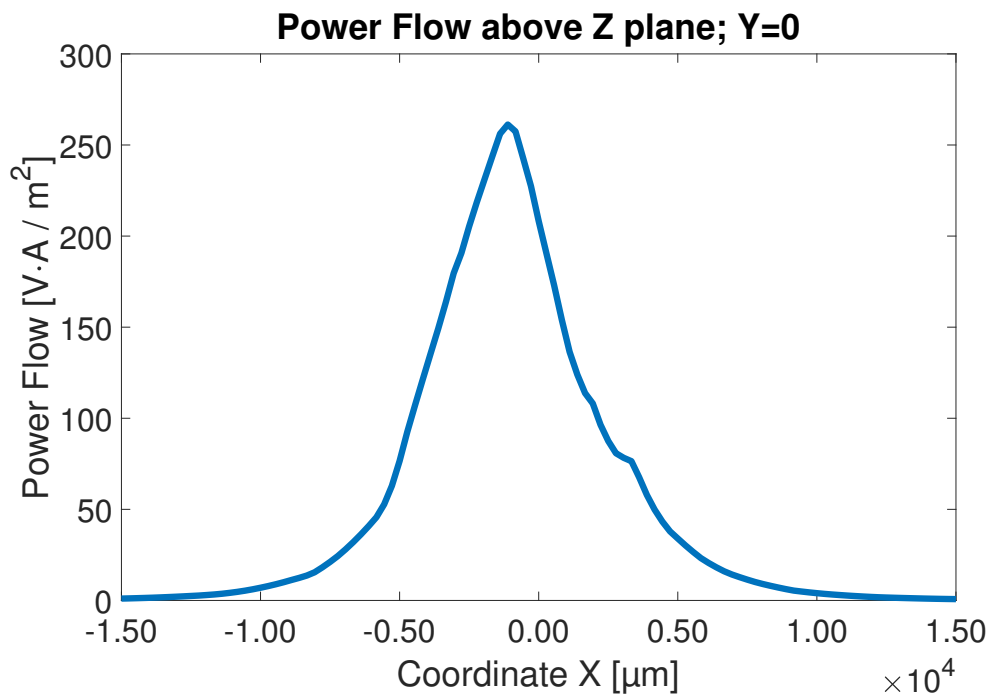


Figure 1.15: First antenna performance, x-axis.

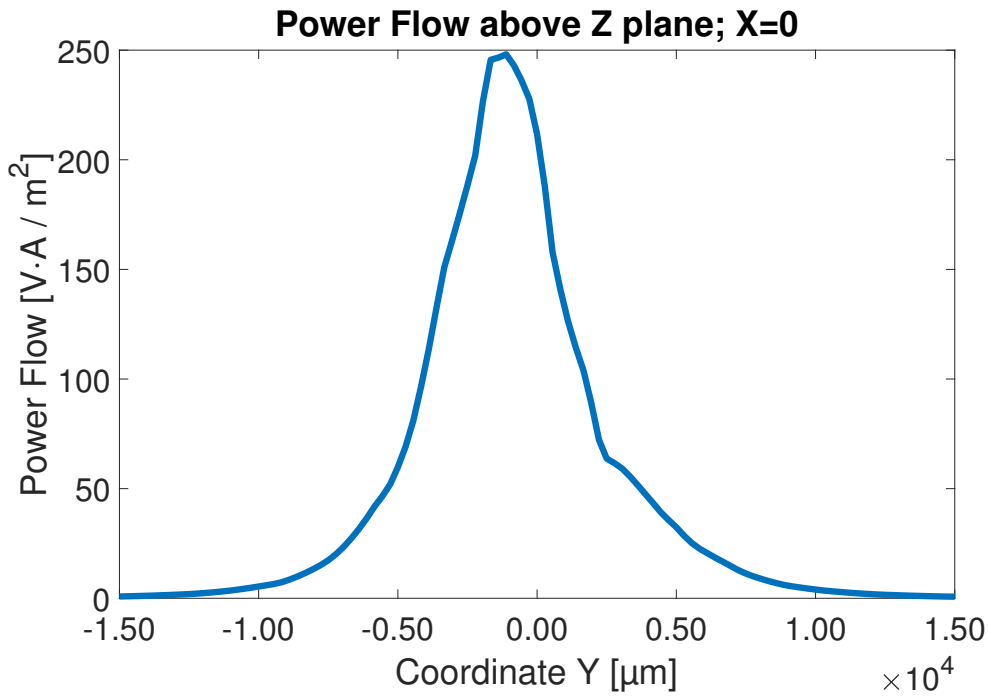


Figure 1.16: First antenna performance, y-axis.

the previous spiral structure with an elevation in the direction of the Z axis. After each complete round the spiral continues above the previous layer. This new antenna structure is depicted in Fig. 1.16. The transparent solid surrounding the 3D spiral structure is the changed substrate with a substantially higher dielectric constant $\epsilon_r = 20$. The input reflection coefficient is $S_{11} = -1.56$ dB and $Z_{in} = 869 - 3759$ j Ω . Since the input reflection coefficient improved significantly, my expectation was an increased amount of power flow. The power flow was evaluated at the same position above the antenna plane as previously. The simulation results are shown in Fig. 1.18 and Fig. 1.19. The antenna performance improved, the power flow peak reached 700 VA/m².

This three-dimensional spiral shaped antenna is a well-formed alternative to the first presented on-chip antenna, as this antenna exhibits better performance without major size increment in planar dimensions. This alternative antenna structure has almost three-times better performance than the first simulated antenna, in terms of power flow. Opting for this alternative antenna design leads to increased reading distance for RFID tags, without the need for higher transmitted power from the reader source.

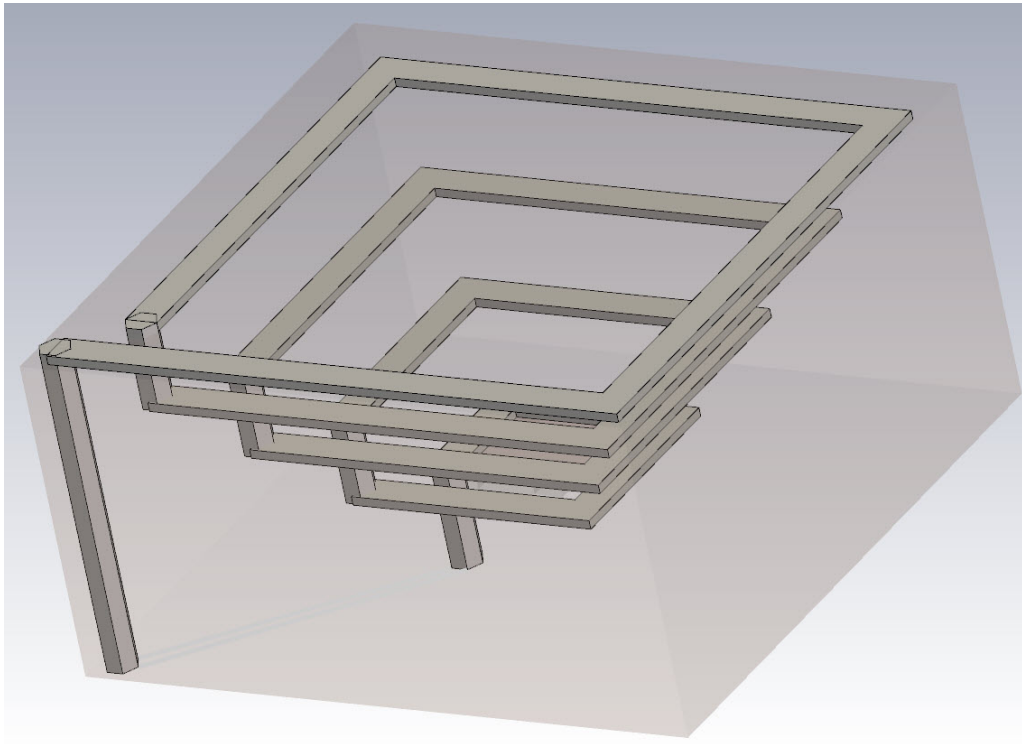


Figure 1.17: 3D spiral antenna model, perspective-view.

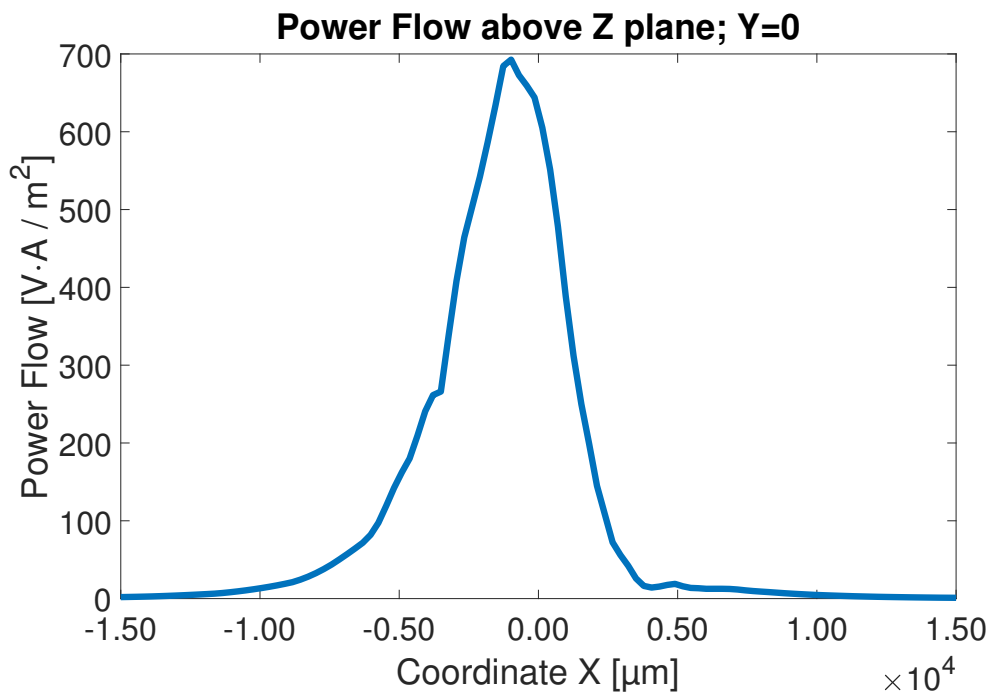


Figure 1.18: 3D multi-layered spiral antenna power flow, x-axis.

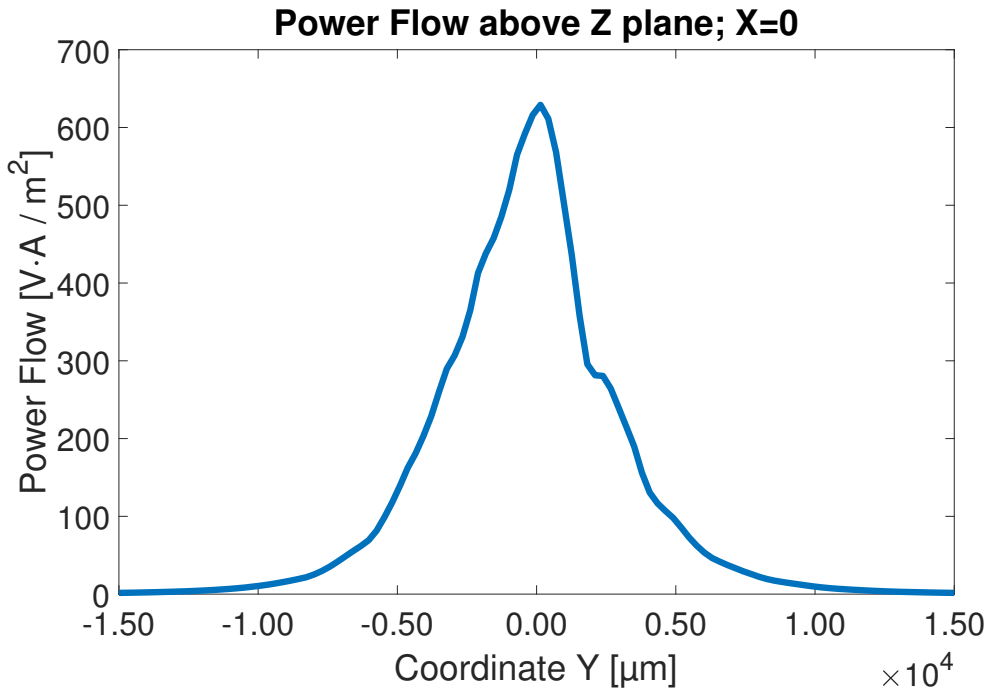


Figure 1.19: 3D spiral antenna power flow, y-axis.

1.10 Summary of Thesis I.

In this thesis, I first briefly presented the wideband complex impedance matching task and its' possible solutions. The scope of this thesis focuses on the wideband analytical complex impedance matching methods. The most common matching methods are briefly presented first: Youla's complex normalization method, Bode-Fano method. The aim of my thesis is to identify and solve the realization problems of the Bode-Fano complex impedance matching method, when combined with admittance or impedance inverters. I introduce the analytical results for both setups and provide a method for avoiding non-realizable matching networks. Finding the initial values before the complete matching process, in order to provide successful matching and realizable network is difficult. Therefore, I introduce an iterative algorithm to overcome this issue. The proposed solution provides the matching network that suits the required application best, within the range of the given input parameters. I suggest a complete step-by-step solution for matching series R-L-C loads, using shorted quarter-wavelength stubs. I validate the matching process performance using MATLAB and thoroughly present the matching process. I can safely stat that the suggested iterative algorithm improves the original Bode-Fano matching method, by automating the matching network design process and yielding only realizable matching networks. Finally, I shortly introduce an

impedance matching task where the Bode-Fano method is not applicable due to some physical constraints. This application area is the matching of ultra-small scale on-chip antennas.

Chapter 2

Differential Space-Divided 2x2 Visible Light Communication in Vehicle-to-Vehicle Applications

2.1 Introduction

Modern high-speed communication systems nowadays are unimaginable without optical-domain communication devices. The optical-domain in communication devices is referred to as the wavelength span between approximately 10 nm and 100 μm . The majority of high-speed fiber-based optical networks use wavelengths such as 850, 1310 and 1550 nm, which are not visible to the human eye. Due to the rising number and lowering cost of semiconductor-based consumer and industrial lighting equipment based on Light Emitting Diodes (LED), an interesting area of application emerged: Visible Light Communication [40]. Semiconductor lighting devices have the inherent ability to change the amount of emitted light rapidly, this property enables efficient light dimming and also data transmission with rapid changes in light intensity. But, what about the receiver side? Fortunately, the optical receiver devices: PIN (Positive Intrinsic Negative) diode and APD (Avalanche Photo Diode) devices were already present in fiber optical receivers. In addition, these optical receivers (optoelectronic converters) are capable of transforming even visible light wavelengths, to electrical signals. The scientific community started in-depth research in the area of VLC [41]. In this chapter, I'm going to present my scientific results and contribution to the field of Visible Light Communication.

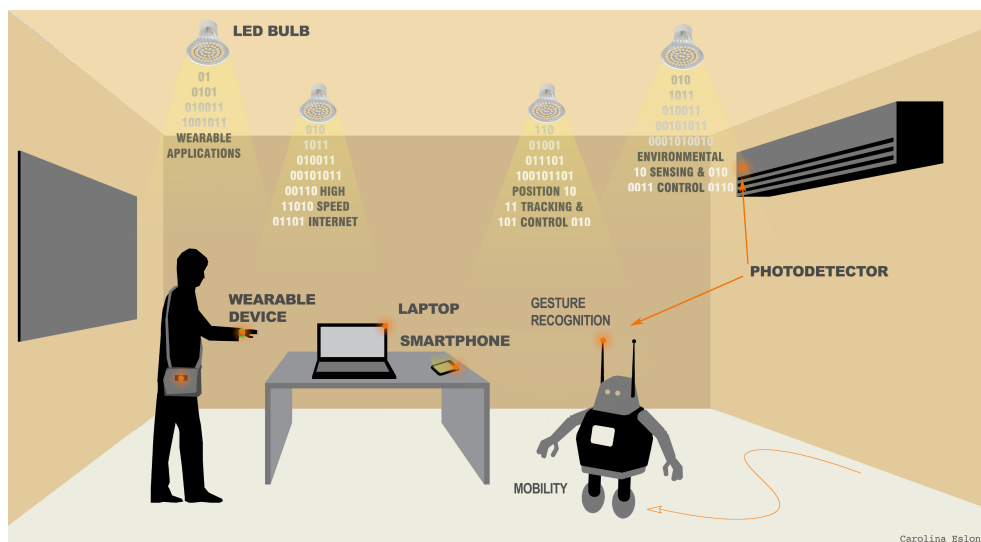


Figure 2.1: The concept of Visible Light Communication (VLC).

The visible light communication spectral range covers approximately 400 THz (from 385 THz to 789 THz), the wavelength span extends from 380 nm to 780 nm [42]. This frequency range is extremely large compared to the significantly more crowded and smaller radio-frequency spectrum (from 30000 Hz to 300 GHz). Moreover, this spectral range is license-free and free to use for communication purposes all around

the world. VLC-systems do not cause any electromagnetic interference, hindering other currently used wireless, radio-frequency communication systems. Besides, visible light does not have any documented serious impact on human health. The only effect worth mentioning is the flickering light of VLC transmitters that can have negative physiological impact on the human eye and brain. However, it has been shown in [42] that flicker frequencies above 200 Hz ¹ does not have any negative impacts on the human eye and brain.

Obviously, VLC based data transmission speed depends on the transmitter, receiver and propagation channel parameters. Generally, VLC data speeds may vary from few kbit/s, up to several Gbit/s. There are three physical types of VLC defined according to the IEEE 802.15.7 standard. PHY I operates from 11.67 kbit/s to 266.6 kbit/s, PHY II operates from 1.25 Mbit/s to 96 Mbit/s and PHY III operates between 12 and 96 Mbit/s. PHY I and PHY II are defined for a single light source and support On-Off Keying (OOK) and Variable Pulse-Position Modulation (VPPM). PHY III uses multiple optical sources with different wavelengths and uses wavelength multiplexing, called Color Shift Keying (CSK) [42]. Higher data speeds are reached with higher-order modulation formats, like N-Quadrature Amplitude Modulation (N-QAM) and frequency domain multiplexing, such as Optical Orthogonal Frequency Division Multiplexing (O-OFDM). As the available bandwidth is large, the only limitations are caused by the parasitic components in the transmitter (LED's junction capacitance) and receiver (photodiode parasitic capacitances) and of course the noises of the channel.

In most VLC links, a Line-of-Sight (LOS) propagation scenario is assumed. This assumption leads to one of the most important property of VLC: locality. In a general indoor environment where illumination devices are used (rooms, industrial halls, hangars, corridors) lights have a spatially limited projected light beam. Hence, the transmitted VLC data can only be captured locally in the range where light-beams are projected. For example, if there are two VLC transmitters which are separated by an opaque² wall, neither of the transmitters would disturb each other (Fig. 2.2). And eavesdropping through the walls are impossible as well. This is an indisputable advantage of VLC with respect to security and space division compared to wireless radio frequency systems. This opens up a wide-range of opportunities for local data transfer, indoor localization, location-based services, indoor navigation etc. All in all, VLC excels in providing a secure, local, LOS communication channel that is impossible to disturb or eavesdrop without physical presence in-between

¹the majority of VLC systems use modulation frequencies way above this limit

²not transparent regarding electromagnetic waves in the wavelength range of visible light

the transceiver units. As the majority of our everyday objects tend to block the propagation of visible light, this locality property can also be interpreted as a serious disadvantage. In VLC applications, where large areas are covered with VLC access and there is no LOS, more VLC transceivers must be placed for ample coverage than should be with other wireless radio frequency based solutions.

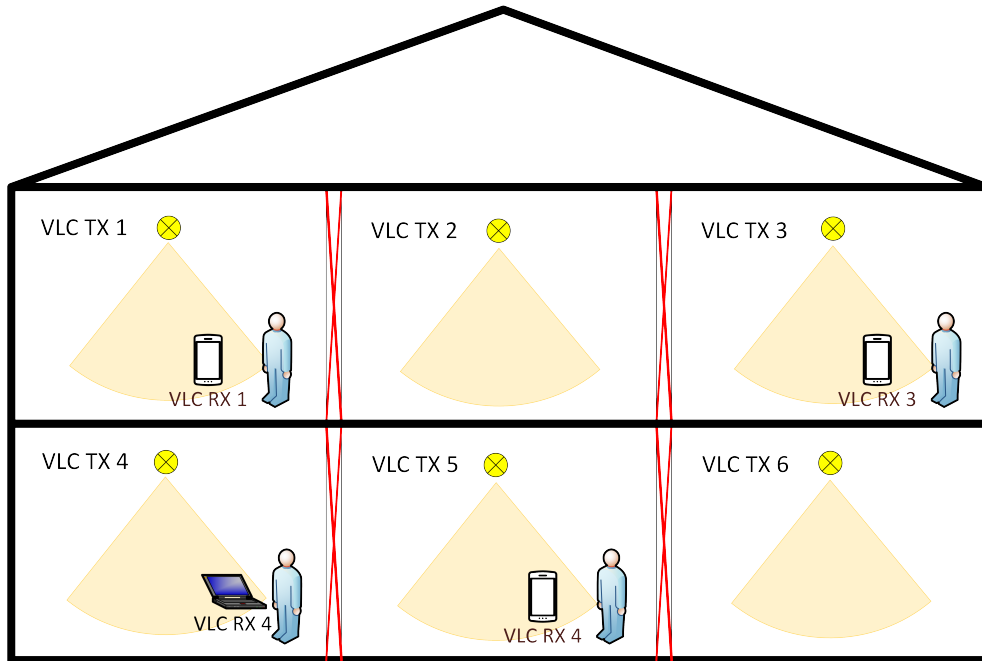


Figure 2.2: Multi-room, multi-user VLC scenario. No light penetration through the walls, hence eavesdropping among users may not happen. [43]

2.2 Applications of Visible Light Communication

The only area where VLC systems are not considered self-serving, are the ones where illumination plays a key role in the application, beside communication. A counter-example for this: if one uses VLC for television remote controllers instead of the already widespread infrared solution. In this case, visible light does not have any further added value, when compared to the infrared solution. Furthermore, as illumination generally requires a one-way light path, VLC performs best for applications where simplex or broadcast type communication is required. Naturally, uplink paths can be implemented with VLC, but there is not necessary a particular reason to do so. One could easily use infrared or other solutions for uplink.

2.2.1 Underwater Communication

Underwater communication is one of the key applications of VLC. The demand for underwater communication is increasing rapidly, due to the raised number of Underwater Unmanned Autonomous Vehicles (U-UAV). Reliable communication between U-UAVs and humans (divers) under water is outstandingly important [44, 45]. The reason why VLC (especially wavelengths in the range of blue-green light) is used for underwater systems, is that the lowest attenuation is achieved on these wavelengths in sea water [46]. In case of underwater VLC the feature of providing visible light for better visibility in deep sea operations is only a secondary purpose. Compared to existing underwater communication solutions, like communication based on acoustic waves and radio frequency links, VLC has some important advantages. VLC provides much larger data speeds, better communication range, lower cost, smaller transmitters and receivers [47]. There are several in-depth studies on underwater VLC seen in [48, 49]. The application is shown in Fig. 2.3.

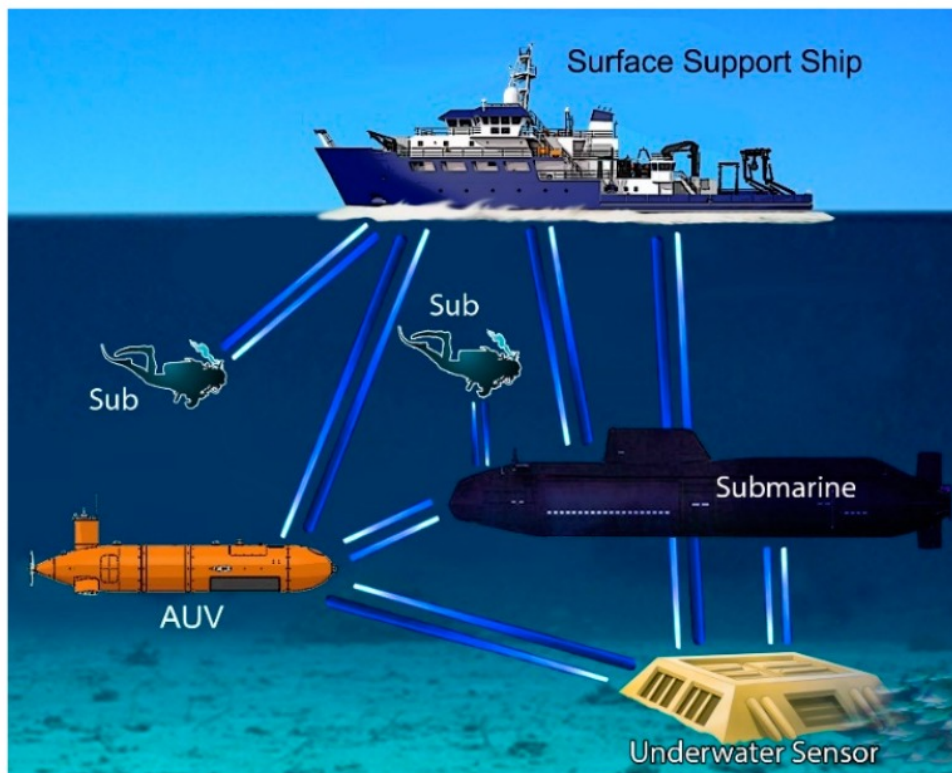


Figure 2.3: An Underwater Visible Light Communication scenario (U-VLC). [50]

2.2.2 Indoor Localization and Navigation

As indoor localization is not possible with conventional satellite-based solutions e.g.: Global Positioning System (GPS), there are currently several studies regarding

indoor localization and navigation for industrial and consumer applications [51, 52, 53] using VLC. As mentioned earlier, one of the major benefits of VLC is the spatial limitation of light propagation. Using custom designed VLC transmitters, localization accuracy can reach up to few centimeters [54, 55]. With these devices integrated into the currently available illumination devices, VLC-based location anchors are created. If these VLC anchors are well distributed and placed, a VLC receiver is able to determine which anchor is currently the nearest. Thus, it can provide a good estimate for the indoor position. Naturally, there are several implementations of such VLC positioning systems Fig. 2.4. Indoor navigation based on VLC is also a viable option, using the location data and base map of the environment. Indoor navigation based on VLC opens up a wide range of applications for controlling unmanned autonomous vehicles, robots, object tracking or providing position information for the visually impaired people [56, 57] etc.

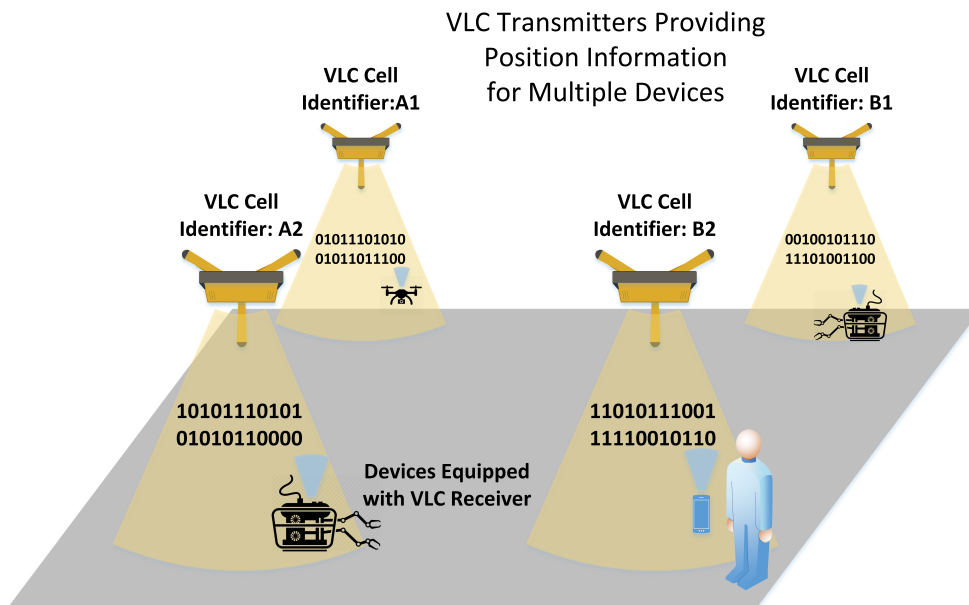


Figure 2.4: Indoor positioning and navigation via spatially distributed VLC transmitter anchors and devices equipped with VLC receivers.

2.2.3 Vehicle-to-X (V2X) Communication

There are two important areas of V2X: Vehicle-to-Vehicle (V2V) and Vehicle-to-Infrastructure (V2I). When data transmission happens between moving or stationary vehicles cars, motorcycles, bicycle etc., it is considered V2V [58, 59]. When the data transmission occurs between one stationary object and a moving vehicle: for example a traffic light and a moving car, that is called V2I. As traffic organization facilities are already using visible light for sending basic commands

to the human drivers (red light: stop, green light: go etc.) VLC based V2I may serve as an alternative communication method for autonomous connected vehicles (shown in Fig. 2.5). The actual states and upcoming maneuvers between vehicles such as reversing, turning, braking are indicated with different visible light colors: white, orange and red respectively. As these indicator lights in modern vehicles are mostly LEDs [60, 61], VLC-V2V integration wouldn't take large effort. Using the built-in LED lights in vehicles, several real-time information (traffic updates, navigation command, vehicle state, vehicle speed etc.) is shared between vehicles, enabling more efficient, optimized traffic organization or even autonomous vehicles [62, 63].

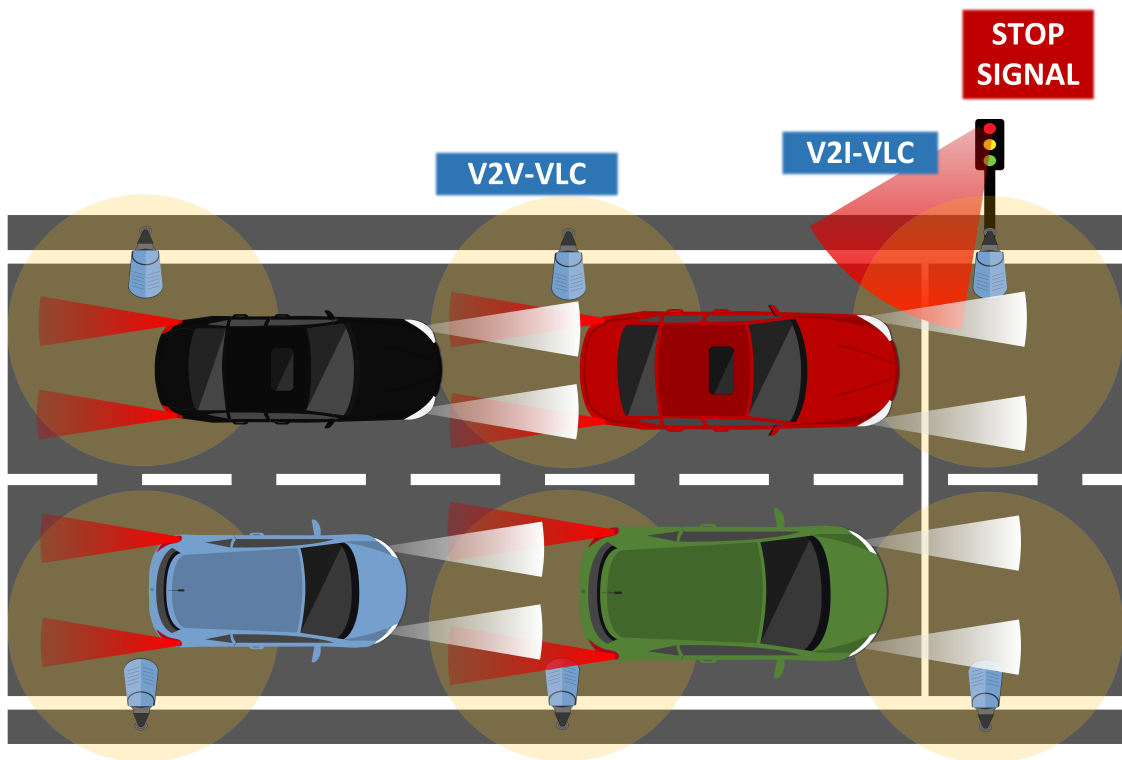


Figure 2.5: V2X Communication via VLC. Vehicles share real-time traffic and vehicular data, enabling massive real-time traffic control operations and other important features.

2.3 Visible Light Communication in Vehicle-to-Vehicle Applications (VLC-V2V)

Visible light devices have been used for illumination and driver notification purposes in the automotive industry since the earliest days. Front lights were used for illuminating the road under badly lit road conditions. Brake lights were applied at the back of the vehicles, in order to prevent rear-end collisions. Turning light

indicators were added to indicate the upcoming changes in the vehicle's expected trajectory. The meaning of these indicator lights is decoded by the other drivers and vehicle maneuvers are chosen with respect to these signals. As known from several studies, a large amount of car accidents are caused by the intermittent loss of driver attention, leading to slow reaction speeds in cases of emergency maneuvers. VLC-V2V may offer an alternative in cases where visible light indicators act as an immediate trigger indicator for a specific driver interaction, such as emergency braking. In modern vehicles these functions Autonomous Emergency Braking (AEB) or Adaptive Cruise Control (ACC) is implemented using short-range radio frequency RADARs. VLC-V2V offers a viable alternative even for these advanced functions by establishing a real-time connection and data sharing between vehicles. This real-time connection may even solve the emerging problems of traffic organization, such as phantom traffic jams and overcrowded lanes. As vehicles use visible light devices in the front (headlights) and the back (taillights), relaying data between several vehicles with very short delay is also available. For instance, Fig. 2.6 presents a possible situation where the VLC-V2V system cooperates with the built-in RADAR and immediately transmits an AEB trigger signal backwards to other vehicles, thus avoiding chain reaction rear-end collisions.

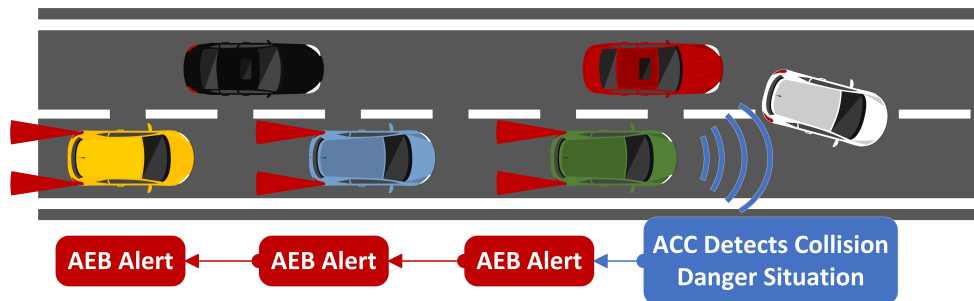


Figure 2.6: The white car initiates a dangerous lane switch, the Adaptive Cruise Control RADAR (ACC) detects and identifies the situation and emergency brake message is transmitted instantaneously through the brakelights backwards via VLC-V2V

Naturally, transmission parameters like transmission range, bit or packet error rate greatly depends on the VLC-V2V communication channel. As the transmission channel between vehicles has multiple time-variant property and depends on weather and visibility conditions [64], there are several studies available, where the VLC-V2V channel is modeled [61, 65, 66, 67, 68]. There are also studies on the specific impact of some dedicated weather conditions (e.g. fog and rain) [69, 70, 71] to the VLC-V2V channel. As VLC-V2V is an alternative to short-range radiofrequency (RF) communication, the VLC channel is compared to the RF-V2V channel in [72]. The VLC-V2V channel is similar to the short-range Free-Space-Optical (FSO)

channel with the addition of potentially larger time-variance, due to the movement of the transceiver endpoints. In most cases, a Line-of-Sight (LOS) transmission is assumed. There are also studies on non-LOS arrangements, discussed in [73], with an amount of attenuation caused by weather and other environmental effects [67, 71, 74]. The VLC-V2V channel is substantially affected by natural ambient light, sun irradiance [75] and artificial light sources: traffic lights, public lighting and other VLC interference from vehicles or objects nearby [76, 77]. These noises have a significant impact on the quality of the VLC-V2V link. Therefore, their effects must be taken into consideration.

In VLC-V2V links the majority of optical receivers are either high-speed cameras [71, 78, 79] or photodiode based amplified detectors [76, 80]. In several experimental VLC-V2V links, only one receiver is attached to the back or the front section of the vehicle. This single receiver structure collects the transmitter (TX), noise and all other interference signals as shown in Fig 2.7. The signal from noise and interference separation can be implemented in either the optical or the electrical domain. Optical domain separation is performed by using polarization or wavelength filters [76, 81]. Unfortunately, these devices have a considerable amount of insertion loss, therefore utile signal attenuation occurs. Electrical domain separation is done by using analog or digital filters based on the *a priori* information regarding noise frequency and power distribution [80, 82, 83]. However, if there are multiple time-varying noise sources present, their real-time tracking and suppression becomes remarkably difficult. If the noise source's signal overlaps with the utile signal in the frequency domain, simple linear filtering is unable to separate signal from noise. My aim is to introduce a new method for reducing the effects of common-mode optical noise in VLC-V2V applications. My suggested method does not require neither optical wavelength and polarization filters nor any electrical domain filters, thus providing a cost-efficient alternative to other known solutions, presented in [84, 85, 86]. Moreover, the proposed system performs better than conventional VLC-V2V solutions in several aspects.

2.4 The Concept of Differential Space-Divided 2x2 VLC-V2V

The 2x2 D-SD VLC-V2V link consists of the headlights (or taillights) of the vehicle and the receiver units at the back (or the front) of the vehicle. If the transmitter headlights (or taillights) are driven complementary, only one VLC transmitter sends

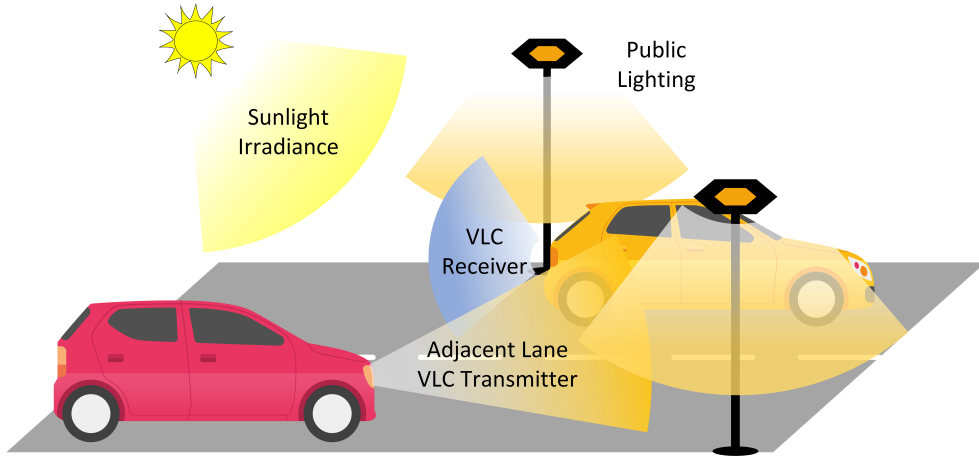


Figure 2.7: The VLC receiver at the back of the vehicle. It collects all visible light signals, from sun irradiance, public lighting and light beams of vehicles in the adjacent lanes.

a light signal during a single bit transmission. The other transmitter does not emit light. Assuming that one transmitted light beam only reaches the corresponding receiver, the received signals have the complementary property as well. If both VLC receivers are affected by common-mode, identical amplitude visible light noise, by simultaneously subtracting the two receiver signals the transmitted VLC signal remains the same, whereas the common-mode noise signal is eliminated. This method is similar to the well-known differential signal transmission used in wired communication applications, used for common-mode noise reduction. Figure 2.8 presents the two different VLC-V2V solutions, 2x2 D-SD and 2x2 C-SD as well. In order to accurately investigate the benefits and drawbacks of the suggested 2x2 D-SD VLC-V2V solution, the following section presents the mathematical background and the simulation comparison under several noise distribution and other channel conditions, with the conventional 2x2 C-SD VLC-V2V.

2.4.1 Mathematical Background of 2x2 C-SD and 2x2 D-SD for VLC-V2V

To highlight the beneficial properties regarding the noise cancellation performance of the 2x2 D-SD I'm going to present a mathematical model that is able to compare 2x2 D-SD to 2x2 C-SD. I present the fundamental calculations regarding common-mode and non-common-mode noise signals and their influence on the transmission performance. Later on, in the next section I use these mathematical formulae and equations for the simulation environment implementation.

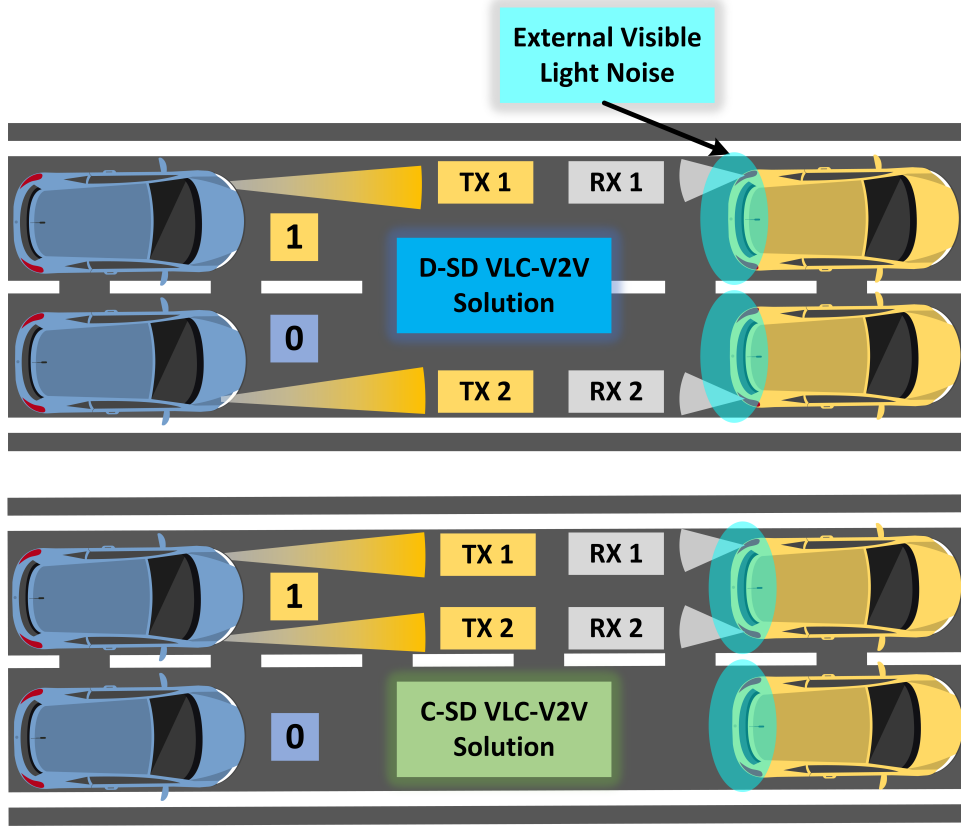


Figure 2.8: The D-SD VLC-V2V vs. C-SD VLC-V2V solution. In ideal situations TX-A activates RX-A and TX-B RX-B respectively, all other external visible light noise is superimposed to all receivers. In C-SD the signals of RX-A and RX-B are summed, contrary to D-SD, where RX-B is subtracted from RX-A.

The signals on the transmitter side for the dual-transmitter setup are

$$\underbrace{\begin{bmatrix} S_1(t) \\ S_2(t) \end{bmatrix}}_{\text{TX output}} = \underbrace{\begin{bmatrix} s_1(t) \\ s_2(t) \end{bmatrix}}_{\text{Source signal}} + \underbrace{\begin{bmatrix} n_{s1}(t) \\ n_{s2}(t) \end{bmatrix}}_{\text{TX noise}}, \quad (2.1)$$

where $s_1(t)$ and $s_2(t)$ are the noise-free transmitter signals and $n_{s1}(t)$ and $n_{s2}(t)$ are the two additive, uncorrelated noise signals, representing internal transmitter noises. The signals on the receiver side for the dual-receiver setup are

$$\underbrace{\begin{bmatrix} r_1(t) \\ r_2(t) \end{bmatrix}}_{\text{RX output}} = \underbrace{\begin{bmatrix} a_{11} & a_{12} \\ a_{21} & a_{22} \end{bmatrix}}_{\text{Crosstalk and attenuation}} \cdot \underbrace{\begin{bmatrix} S_1(t) \\ S_2(t) \end{bmatrix}}_{\text{TX output}} + \underbrace{\sum_{j=1}^K \begin{bmatrix} b_{f,j} \cdot N^{(j)}(t) \\ (1 - b_{f,j}) \cdot N^{(j)}(t) \end{bmatrix}}_{\text{Common-mode noises}} + \underbrace{\begin{bmatrix} n_{r1}(t) \\ n_{r2}(t) \end{bmatrix}}_{\text{RX noise}}, \quad (2.2)$$

where a_{mn} are constant coefficients representing crosstalk and transmission between TX m and RX n , $0 < b_{f,j} < 1$ is the balance factor of the j^{th} common-mode noise component $N^{(j)}$, whereas n_{r1} and n_{r2} represent residual receiver noise components. The total number of common-mode noise components is K . This matrix

representation contains the crosstalk between the two channels. Therefore, crosstalk is

$$X_{1 \rightarrow 2} = \frac{a_{21}}{a_{22}} : \text{crosstalk from TX1 to RX2}, \quad (2.3)$$

$$X_{2 \rightarrow 1} = \frac{a_{12}}{a_{11}} : \text{crosstalk from TX2 to RX1}. \quad (2.4)$$

The 2x2 C-SD method sums the two received signals $r_1(t)$, $r_2(t)$ and these source signals $s_1(t)$, $s_2(t)$ are identical. Therefore, the output signal for the 2x2 C-SD method $o^c(t)$ is

$$\begin{aligned} o^c(t) &= r_1(t) + r_2(t) \quad (2.5) \\ &= (a_{11} + a_{12} + a_{21} + a_{22}) \cdot s_1(t) \\ &\quad + (a_{11} + a_{21}) \cdot n_{s1}(t) + (a_{12} + a_{22}) \cdot n_{s2}(t) \\ &\quad + \sum_{j=1}^K N^{(j)}(t) + n_{r1}(t) + n_{r2}(t). \end{aligned}$$

The 2x2 D-SD method subtracts the two received signals $r_1(t)$ and $r_2(t)$ and the source signals $s_1(t)$ and $s_2(t)$ are complementary ($s_1(t) = -s_2(t)$). Therefore, the output signal for the 2x2 D-SD method $o^d(t)$ is

$$\begin{aligned} o^d(t) &= r_1(t) - r_2(t) \quad (2.6) \\ &= (a_{11} + a_{22} - a_{12} - a_{21}) \cdot s_1(t) \\ &\quad + (a_{11} - a_{21}) \cdot n_{s1}(t) + (a_{12} - a_{22}) \cdot n_{s2}(t) \\ &\quad + \sum_{j=1}^K (2 \cdot b_{f,j} - 1) \cdot N^{(j)}(t) + n_{r1}(t) - n_{r2}(t). \end{aligned}$$

Eq. 2.6 clearly shows that crosstalk (a_{12} and a_{21}) influences the output signal differently. In 2x2 C-SD it increases the received utile signal amplitude, contrary to 2x2 D-SD. The aforementioned equations also imply that 2x2 D-SD is capable of common-mode noise reduction if $0 < b_{f,j} < 1$. 2x2 D-SD is also capable of reducing TX noise (n_{s1} and n_{s2}), if crosstalk is not zero. However, neither 2x2 C-SD nor 2x2 D-SD is capable of reducing the independent, uncorrelated RX noises. Assuming an ideal setup, where all common-mode noise components are perfectly balanced ($b_{f,j} = 0.5 \forall j$), crosstalk and receiver noises are negligible ($a_{12} = a_{21} \approx 0$, $n_{r2} = n_{r1} \approx 0$) the expression is modified to

$$o^c(t) = (a_{11} + a_{22}) \cdot s_1(t) + a_{11} \cdot n_{s1}(t) + a_{22} \cdot n_{s2}(t) + \sum_{j=1}^K N^{(j)}(t), \quad (2.7)$$

$$o^d(t) = (a_{11} + a_{22}) \cdot s_1(t) + a_{11} \cdot n_{s1}(t) - a_{22} \cdot n_{s2}(t). \quad (2.8)$$

It is clear from Eq. 2.7 and Eq. 2.8 that the 2x2 D-SD solution completely eliminates common-mode noise. The 2x2 D-SD equation states that transmitter noise components' reduction depends on the correlation between $n_{s1}(t)$ and $n_{s2}(t)$. If correlation is low, neither 2x2 D-SD, nor 2x2 C-SD is able to reduce noise. On the other hand if correlation is high, 2x2 D-SD provides better noise reduction.

2.5 2x2 D-SD VLC-V2V Simulation Environment and Results

In this section the 2x2 C-SD setup is compared to the suggested 2x2 D-SD arrangement in a MATLAB simulation environment. For the ease of calculation, all signals are analyzed in the electrical domain after the optical/electrical conversion. Noise factors and non-linearities originating from optical/electrical conversion, thermal noise, optical shot noise were assumed to exhibit a much lower impact on the quality of transmission than the added noise, hence they were omitted during the simulation. The main features of the simulation environment are

- random bit-sequence generation,
- compatible 2x2 C-SD and 2x2 D-SD mode for accurate comparison,
- 2 individual noise channels with adjustable noise functions,
- implemented Additive White Gaussian Noise (AWGN) source for analyzing non-common-mode noise effects,
- ability to analyze the effects of amplitude imbalance and crosstalk between propagation channels,
- approximate Bit Error Rate (BER) calculation based on Q-factor calculation and eye-diagram,
- graphical representation of the transmitted, received and output signals.

The complete simulation environment is based on the equations presented in the mathematical background section (Sec. 2.4.1). Using my simulation environment (schematic diagram shown in Fig. 2.9) the 2x2 C-SD can be compared to the proposed 2x2 D-SD solution precisely.

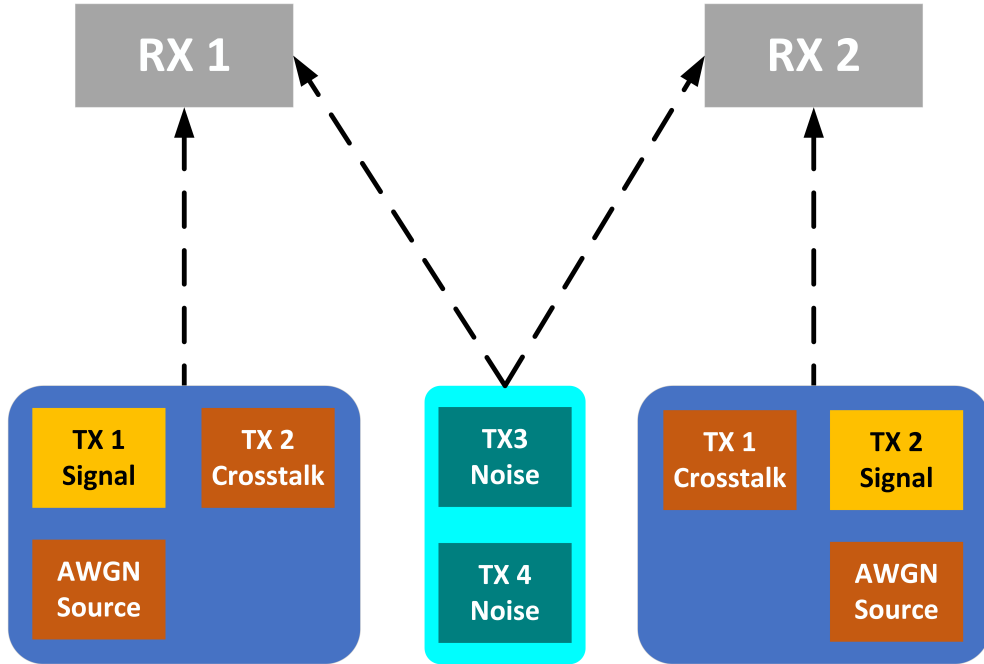


Figure 2.9: Schematic diagram of the signals and signal routes implemented in the simulation environment. Crosstalk, external noise sources (TX3 and TX4) and AWGN noise effects may be investigated.

2.5.1 The Simulated 2x2 D-SD Noise Rejection Performance

The simulation results are presented to highlight noise reduction performance differences between the 2x2 C-SD and 2x2 D-SD arrangement. For appropriate comparison, all the simulation parameters, noise properties are fixed for making the difference between 2x2 C-SD and 2x2 D-SD clear. First the simulation parameters are adjusted for a general comparison. In this first simulation setup, three noise sources are used: 2 common-mode balanced noise sources and 1 non-common-mode AWGN source. For exact comparison and reproducible results, the simulation environment parameter values are presented in Tab. 2.1. The expected results based on the *a priori* assumptions are the following: common-mode balanced noises will deeply affect 2x2 C-SD output signal quality, contrary to 2x2 D-SD, where the subtract operation will eliminate common-mode balanced noise. On the other hand, the non-common-mode AWGN source will approximately equally affect output signals in both the 2x2 C-SD and 2x2 D-SD setup. In order to quantify performance the approximated Bit Error Rate is used, based on the calculated quality factor (later on Q-factor). I used the following equation for the BER approximation

$$BER \approx \frac{1}{2} \operatorname{erfc} \left(\frac{Q}{\sqrt{2\pi}} \right). \quad (2.9)$$

<i>Parameter name</i>	<i>Value</i>	<i>Short description</i>
TX1 Amplitude	0.2	Transmitted VLC signal amplitude from TX1
TX1 bits/s	115200	Transmitted VLC signal frequency from TX1
AWGN TX1 Amplitude	0.1	AWGN noise amplitude affecting TX1
TX2 Amplitude	0.2	Transmitted VLC signal amplitude from TX2
AWGN TX2 Amplitude	0.1	AWGN noise amplitude affecting TX2
TX1 to RX2 Crosstalk	0	Crosstalk from TX1 towards RX2
TX2 to RX1 Crosstalk	0	Crosstalk from TX2 towards RX1
TX3 Noise Type	square	Noise signal type: square, constant, sine
TX3 Noise Target	both	Noise target: RX1, RX2, both
TX3 Noise Frequency	57600	Noise signal frequency of TX3
TX3 Noise Amplitude	0.1	Noise signal amplitude of TX3
TX3 Noise Balance	50 %	Noise distribution among RX1 and RX2
TX4 Noise Type	sine	Noise signal type: square, constant, sine
TX4 Noise Target	both	Noise target: RX1, RX2, both
TX4 Noise Frequency	10000	Noise signal frequency of TX4
TX4 Noise Amplitude	0.1	Noise signal amplitude of TX4
TX4 Noise Balance	50 %	Noise distribution among RX1 and RX2

Table 2.1: Simulation parameters for the noise reduction comparison.

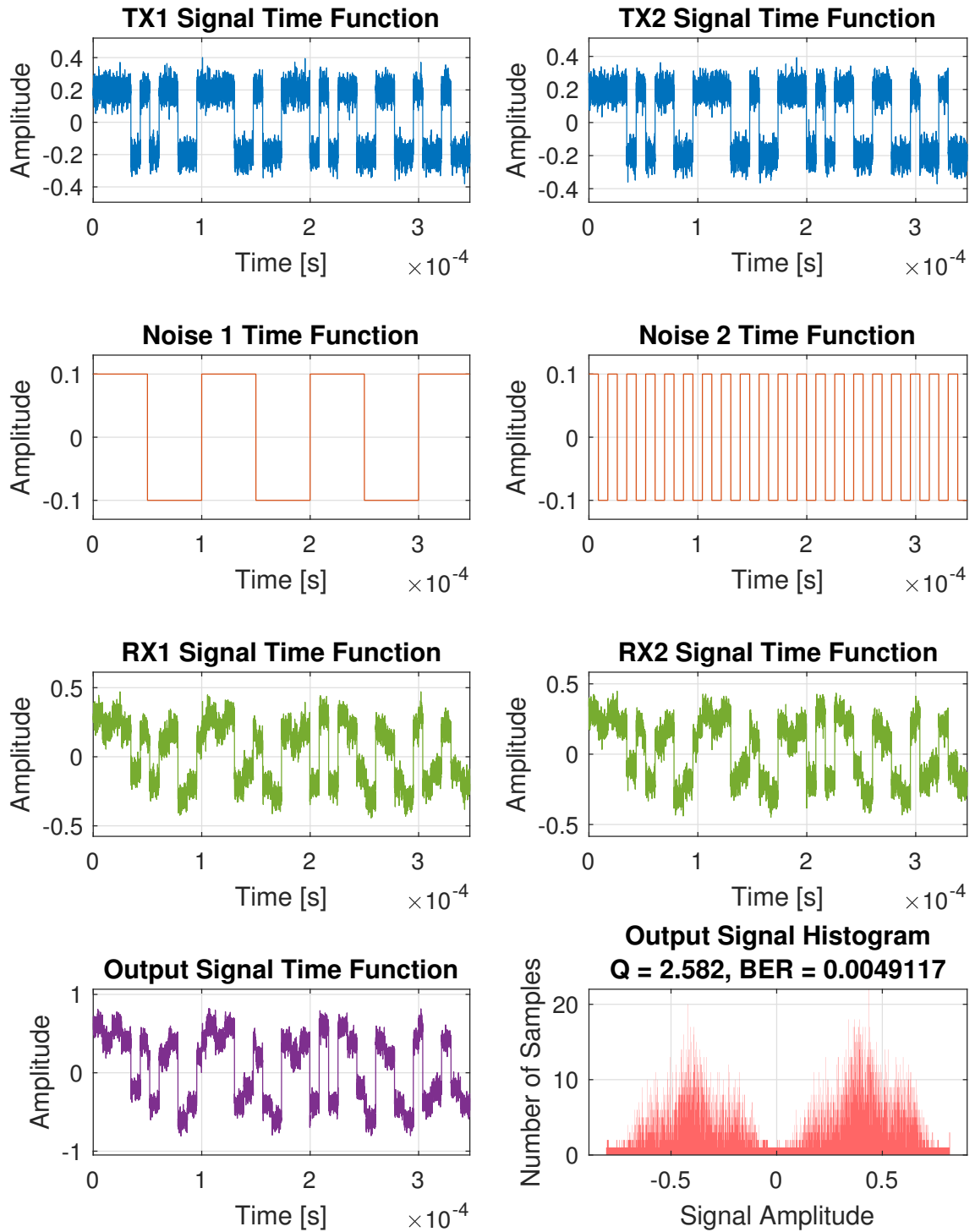


Figure 2.10: 2x2 CT simulation results. Amplitude values are in arbitrary units, time scale is in seconds. The two transmitter signal functions (TX1, TX2) are influenced by two balanced common-mode noises (Noise 1 and Noise 2). The effects of common-mode noise is perceivable in the received signal (RX1 and RX2). The output signal in this case is the sum of RX1 and RX2. The signal amplitude distribution is spread out, resulting in weak performance and high BER.

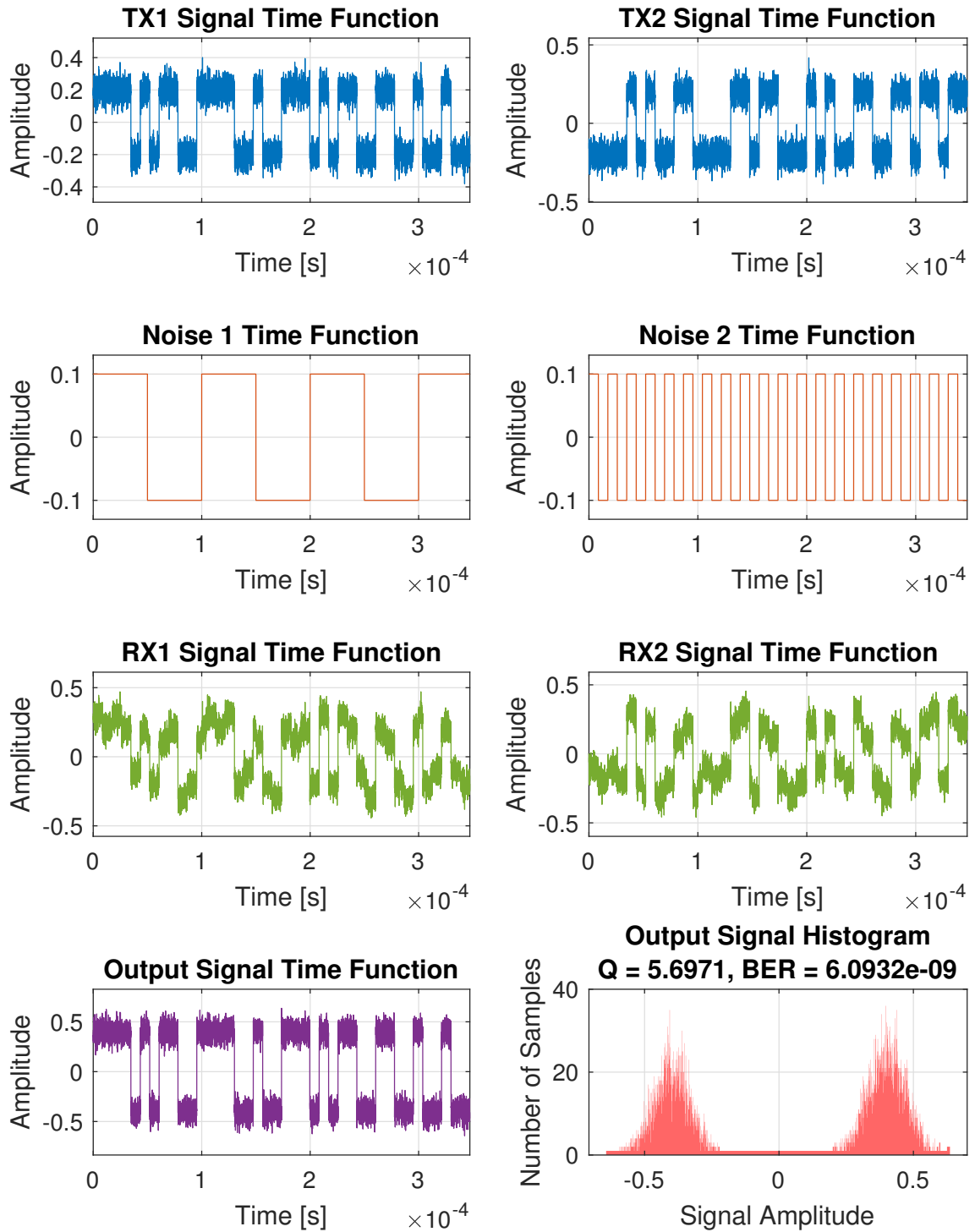


Figure 2.11: 2x2 DT simulation results. Amplitude values are in arbitrary units, time scale is in seconds. The two transmitter signal functions (TX1, TX2) are influenced by two balanced common-mode noises (Noise 1 and Noise 2). The effects of common-mode noise is perceivable in the received signal (RX1 and RX2). The output signal in this case is the difference of RX1 and RX2. The signal amplitude distribution is spread out, resulting in weak performance and high BER.

In Fig. 2.10 and Fig. 2.11, the simulation results are in close relation with the assumptions based on the mathematical background presented in Sec. 2.4.1. Neither the 2x2 C-SD, nor the 2x2 D-SD solution performed well in reducing AWGN. On the contrary, 2x2 D-SD solution excelled at rejecting common-mode noise (from TX3 and TX4) even when the noise signal frequency was the same as the VLC transmitted signal frequency. In addition, the output signal Q-factor (quality) rose from 2.58 to 5.69, when 2x2 D-SD was used instead of 2x2 C-SD with identical added noises. The calculated BER values were: $4.9 \cdot 10^{-3}$ and $6.1 \cdot 10^{-9}$.

In this simulation setup the data-speed was 115200 bit/s ($\approx 10^5$ bits/s). Taking this into consideration, I assumed that a BER value under 10^{-6} was considered error-free. With the 2x2 C-SD solution, approximately 565 bit errors are statistically expected in every second, whereas 2x2 D-SD is considered error-free. Summarizing the above, the 2x2 D-SD solution performed much better and error-free in this comparison. However, as the number of variable parameters is large, further results are presented in in the following section (Sec. 2.5.2).

2.5.2 The Effects of Noise Amplitude Imbalance on Noise Rejection Performance

As mentioned earlier, the beneficial noise reduction property of the 2x2 D-SD solution depends on the amount of crosstalk, i.e. overlap between received light beams. Moreover, the noise rejection performance directly depends on the received noise amplitude balance between the two receivers. For quantifying the performance under several unbalanced signal amplitude situations the Q-factor and BER values are used. The noise balance values in Fig. 2.12 and Fig. 2.13 are interpreted as follows. A noise balance value of 25 % means that 25 % of the total noise amplitude affects one receiver and 75 % the other receiver, respectively. Hence, only amplitude balance values between 0 % and 50 % are calculated. The modified parameters are shown in Tab. 2.2. All other simulation parameters are exactly the same as in the previous section, see Tab. 2.1.

<i>Parameter</i>	<i>Value</i>	<i>Short description</i>
TX3 Noise Balance	0 . . . 50 %	Noise distribution among RX1 and RX2
TX4 Noise Balance	0 . . . 50 %	Noise distribution among RX1 and RX2

Table 2.2: Changed simulation parameters for the noise amplitude balance investigation simulation.

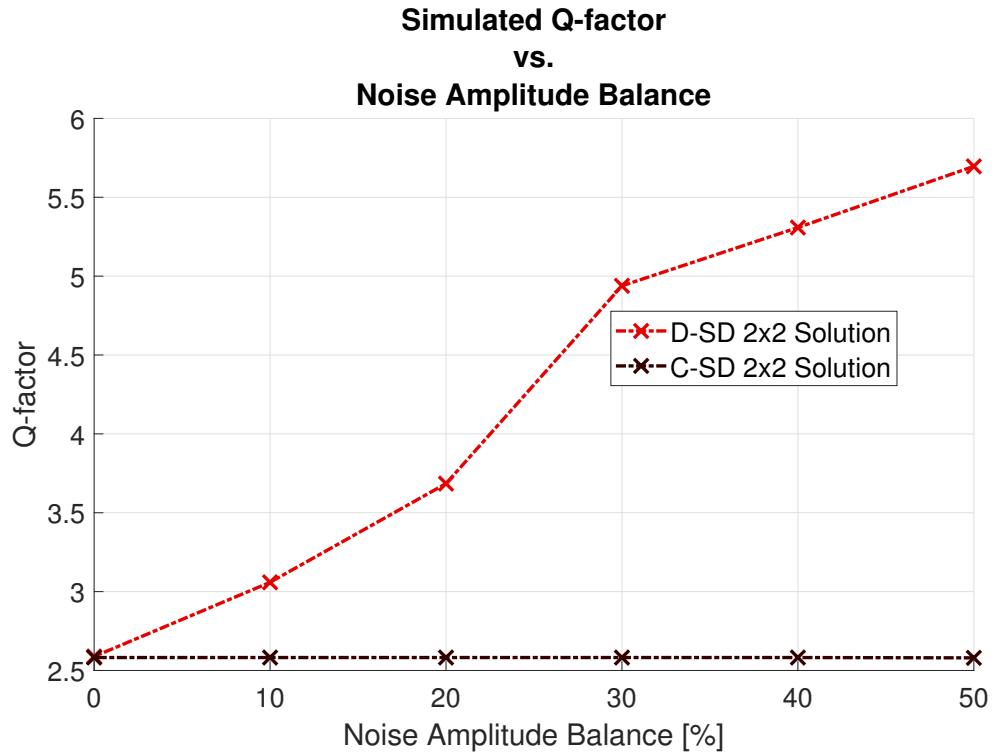


Figure 2.12: The effect of noise imbalance between receivers on the Q-factor.

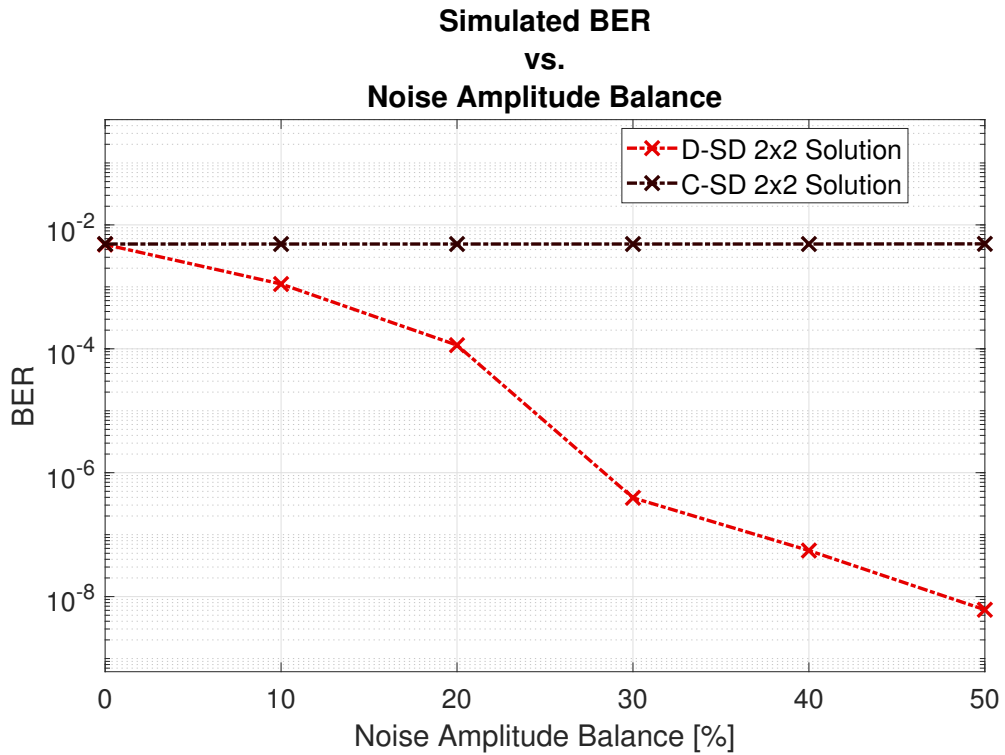


Figure 2.13: The effect of noise imbalance between receivers on the BER.

The simulation results clearly show that the proposed 2x2 D-SD solution provides better performance under almost all noise balance conditions. Naturally, the best noise rejection performance and lowest BER is present with the 2x2 D-SD solution when the noise amplitudes (reaching both receivers simultaneously) are equal. Besides, the 2x2 C-SD solution provides a fairly constant BER with respect to noise balance variance, however these BER values are significantly higher than the 2x2 D-SD solution. Based on these simulation results, I can safely state that the suggested 2x2 D-SD VLC-V2V solution can provide a better alternative under all common-mode noise circumstances.

2.5.3 The Effects of Crosstalk Between Transmitted Signals

This simulation provides an insight into the effects of overlapping light beams at the receiver side. The crosstalk value in simulation is

$$X = \frac{\text{RX Amplitude at RX A from TX B}}{\text{RX Amplitude at RX B from TX B}} \quad [\%]. \quad (2.10)$$

All simulation parameters (signal and noise) were exactly the same, see Tab. 2.1 for details. I'm expecting degrading BER values in the 2x2 D-SD solution as the crosstalk increases. In the simulation setup the crosstalk from TX1 to RX2 was adjusted between 0...100%. The 2x2 C-SD solution will probably exhibit a slowly decreasing BER as crosstalk value rises. The reason for this is that if the amount of crosstalk rises, and the direct path (TX1 to RX1) signal level remains the same as the crosstalk increases, the TX1 to RX2 signal (crosstalk) is added to it. Therefore, in 2x2 C-SD systems crosstalk may be beneficiary from a BER point of view.

As seen in Fig. 2.14 and Fig. 2.15, at the beginning, when there is no overlap between beams (crosstalk) the 2x2 D-SD solution provides significantly better results. This high crosstalk value does not influence the quality of the transmission, if the transmitted light beams are collimated and directed at receivers with narrow Field-of-View (FOV).

2.5.4 Simulation Results Summary

By combining the results in the last three sections the comparison result between the proposed 2x2 D-SD and 2x2 C-SD is clear, see Fig. 2.16. Clearly, there are situations where the conventional 2x2 C-SD transmission leads to better results. The 2x2 D-SD solution outperforms 2x2 C-SD when the crosstalk between light beams are low and the amount of common-mode noise is relatively high, compared to the utile signal levels.

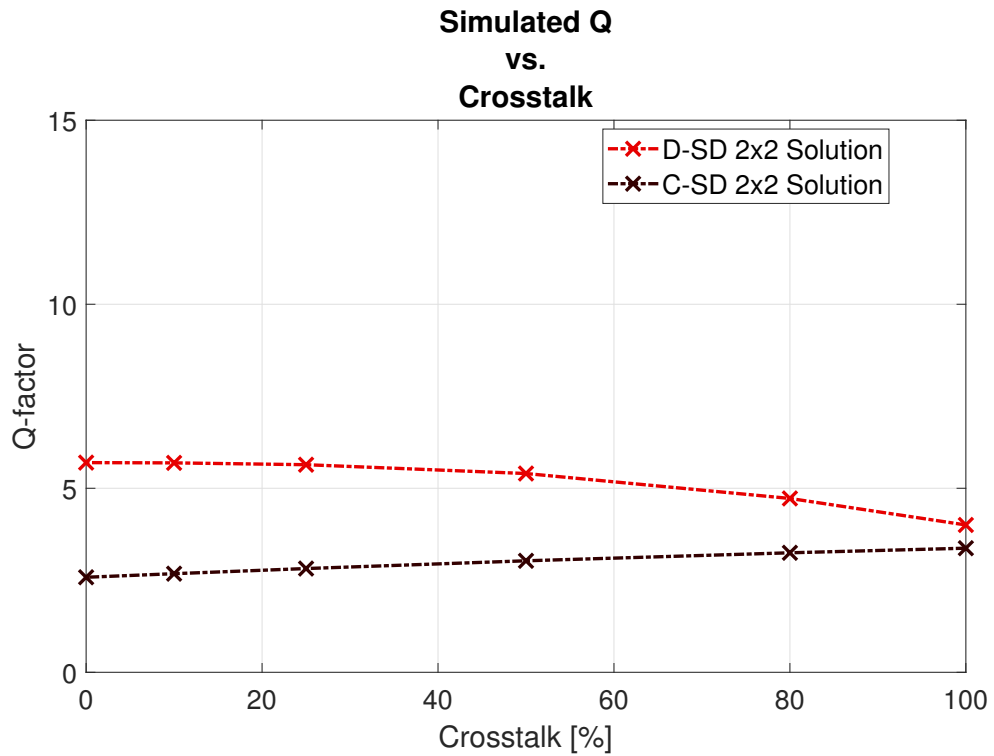


Figure 2.14: The effect of overlapping beams at receivers. Q-factor vs. crosstalk value.

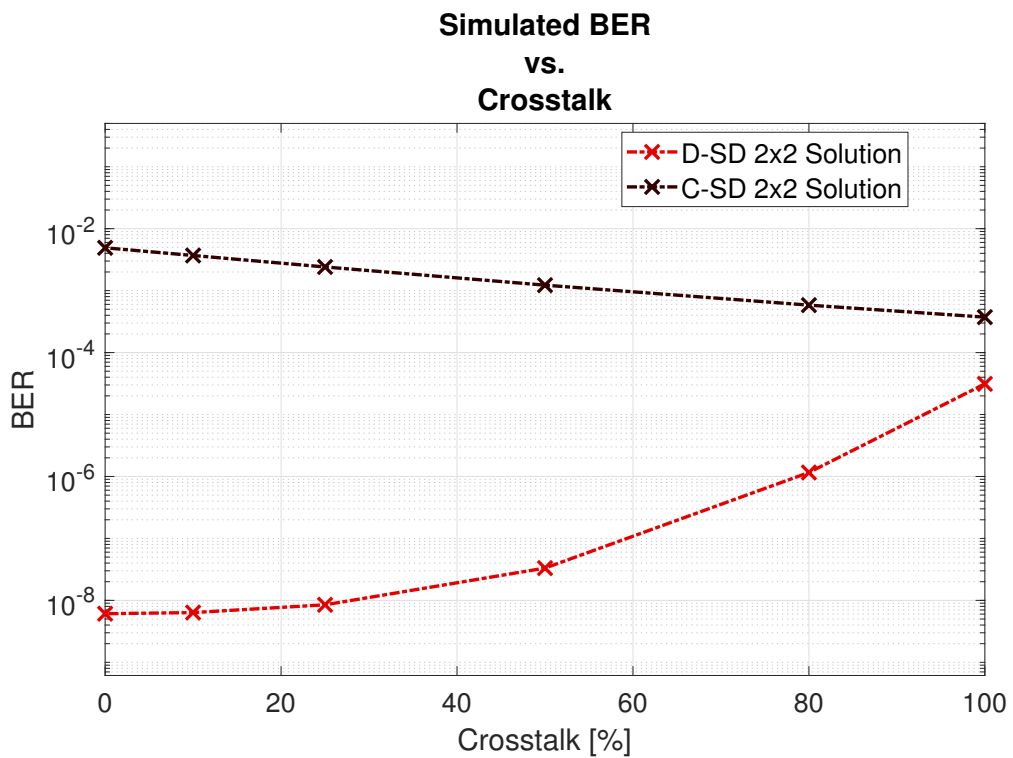


Figure 2.15: The effect of overlapping beams at receivers. BER vs. crosstalk value.

	Low	High
Crosstalk	D-SD 2x2	C-SD 2x2
Noise Amplitude Balance	C-SD 2x2	D-SD 2x2
Noise Amplitude	C-SD 2x2	D-SD 2x2

Figure 2.16: The table for choosing the 2x2 D-SD over 2x2 C-SD, with respect to crosstalk, noise amplitude and noise amplitude balance.

2.6 Visible Light Noise Measurement in Urban Environment Under Low-Light Conditions

After the promising simulation results, the next goal was to identify the nature of optical noise sources that are present in the VLC-V2V channel under low-light environmental conditions. By using a 2x2 D-SD receiver structure, the best noise rejection performance is available when both receivers are affected by balanced common-mode noise. A dedicated measurement setup was designed for investigating whether this type of noise rejection technique performs well in a real-world road test.

2.6.1 Measurement Setup and Data Processing

First, the two photodiode-based amplified detectors were attached to the bottom segment of the car's trunk lid (pointed at with yellow arrows in Fig. 2.17). The two receivers were horizontally 80 cm apart.

The signal of both detectors and the differential amplifier that subtracts the two detector signals were fed into a Data Acquisition Unit (DAU): RedLab 204 USB Mini DAQ. The DAQ was placed on the backseat of the vehicle and connected to a portable PC via USB. The block diagram of the measurement setup is shown in Fig. 2.18.

The signal time functions were recorded with 100 kSample/s. The measurement took place in an urban area, under low-light conditions at night on roads with public lighting. The measurement lasted for 600 seconds altogether. The vehicle moved along the route, obeying the speed limits and laws of the road with an average speed of approximately 25 km/h. The data collected throughout the measurement was

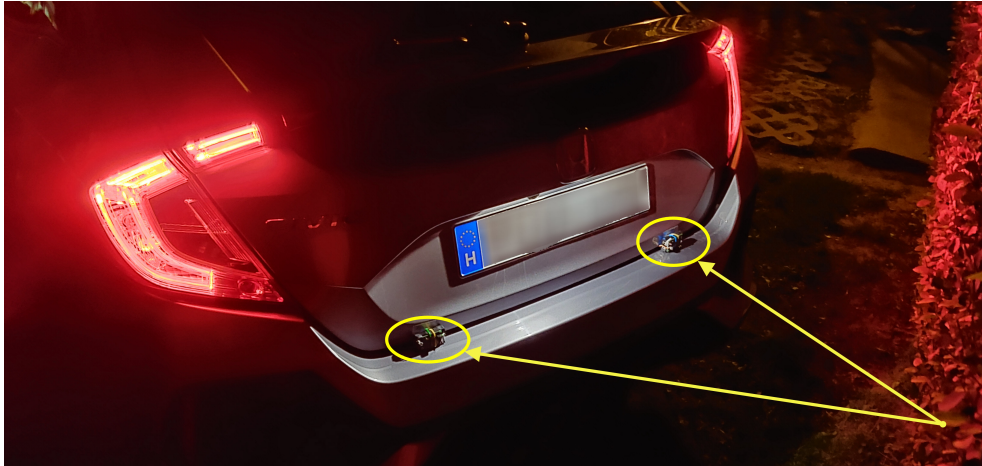


Figure 2.17: Receiver arrangement for road testing on the car's trunk lid.

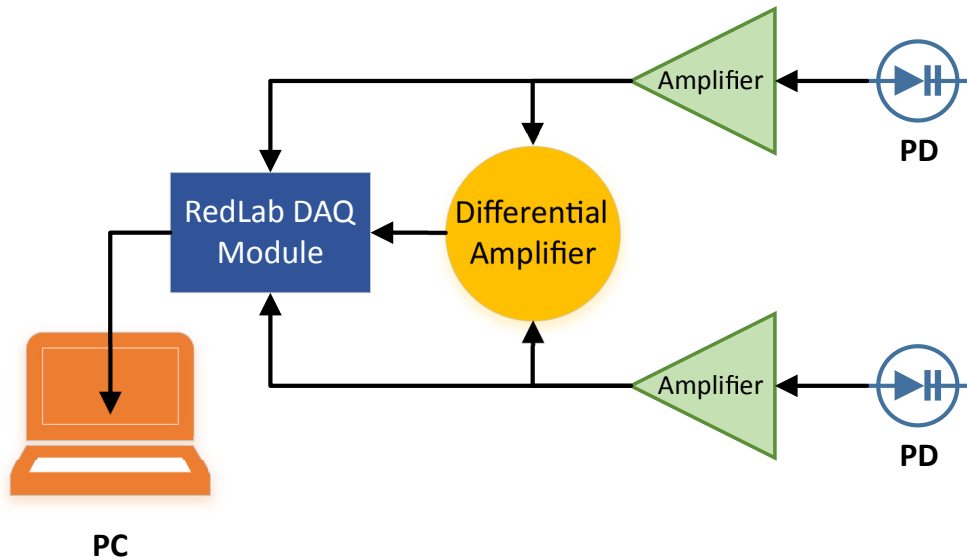


Figure 2.18: Road test measurement setup block diagram.

post-processed in a MATLAB environment. For the demonstration of common-mode noise rejection performance, the discrete Fourier transforms (using the built-in FFT algorithm of MATLAB) was used instead of the recorded time-domain signals. As there were approximately 60 million independent time-domain samples from each signal (RX1, RX2, RX1+RX2, RX1-RX2), it would have been remarkably difficult to visualize the noise rejection performance using time-domain signals. Fig. 2.19 shows a portion of the spectral distribution of two signals: RX1+RX2 sum is yellow, RX1-RX2 difference is red. As we did not encounter dominant higher frequency components above 6.5 kHz, the inset shows components up to 6.5 kHz only. The original plot in Fig. 2.19 highlights the dominant measured frequency components up to 1 kHz.

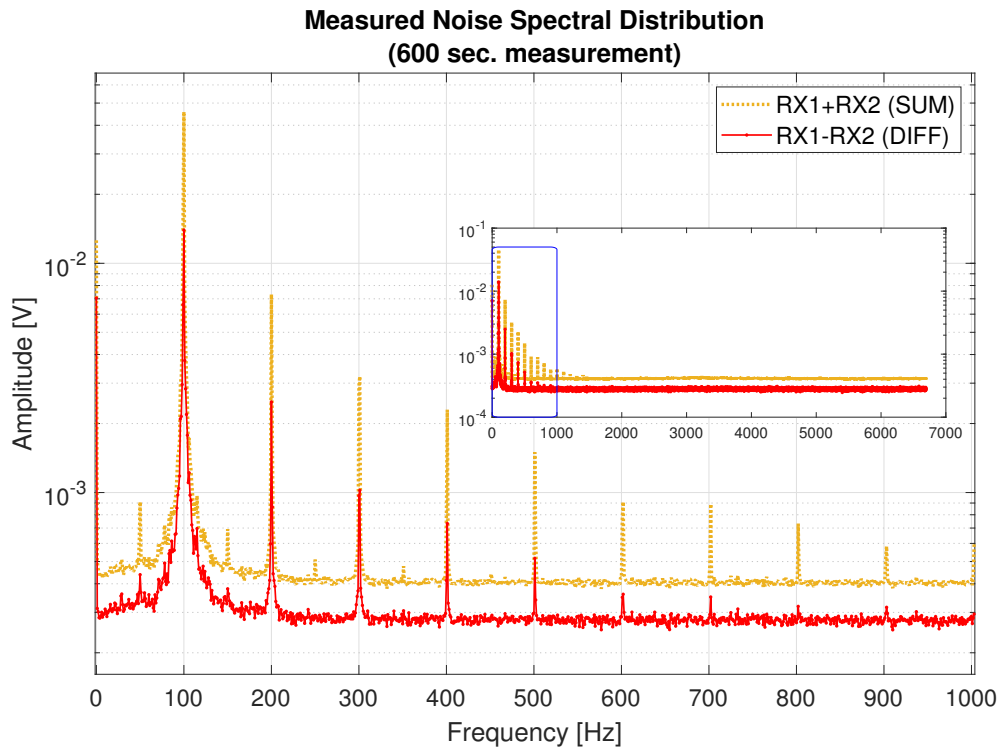


Figure 2.19: Visible light noise measurement results. The spectral distribution of the sum and the difference signals (sum: orange, difference: red).

2.6.2 Evaluation of Measurement Results

Based on research presented in [87], the public lighting alongside the measurement route is based on incandescent lamps as the odd and even harmonics of the 50 Hz driving frequency is present. Interestingly the harmonics of 100 Hz are even more dominant in our measurement. Fig. 2.19 shows the sum and the difference signal spectra of receiver RX1 and RX2. The benefit of the difference signal is clearly present as its peaks (red) are significantly lower than the summed signal spectra (orange). The proposed system's measured common-mode noise reduction performance is promising. I can safely state that the investigated VLC-V2V channel contains significant amount of common-mode noise, caused by public lighting. Our proposed method 2x2 D-SD for reducing this noise type performed successfully in the real-life road test. Concluding the above, the concept of real-time common-mode noise rejection using the 2x2 D-SD receiver performed well in the road-test.

2.7 Indoor Laboratory Measurement Results for 2x2 D-SD VLC-V2V

For further examination of the 2x2 D-SD system performance, I built an indoor 2x2 VLC-V2V transceiver. The schematic diagram is shown in Fig. 2.20, the arrangement in Fig. 2.21 and Fig. 2.22. This arrangement contained two automotive-grade headlights and two custom-built photodiode based amplified detectors. The TX-RX distance (parameter A in Fig. 2.20) was gradually adjusted from 2 m up to 10 m. The RX horizontal distance (parameter B in Fig. 2.20) was set to 1.2 m. The transmission quality is quantified by the Q-factor of the received signals.

2.7.1 Measurement setup

The headlight housings contained a 15 W H7-socket type LED light each with the built-in driving circuit removed. Each headlight was attached to a custom-built VLC driver circuit, capable of 2x2 D-SD and 2x2 C-SD VLC-V2V operation. The transmitted signal in our setup was a pseudo-random bit sequence with a data speed of 115.2 kbps (square signal, OOK modulation).

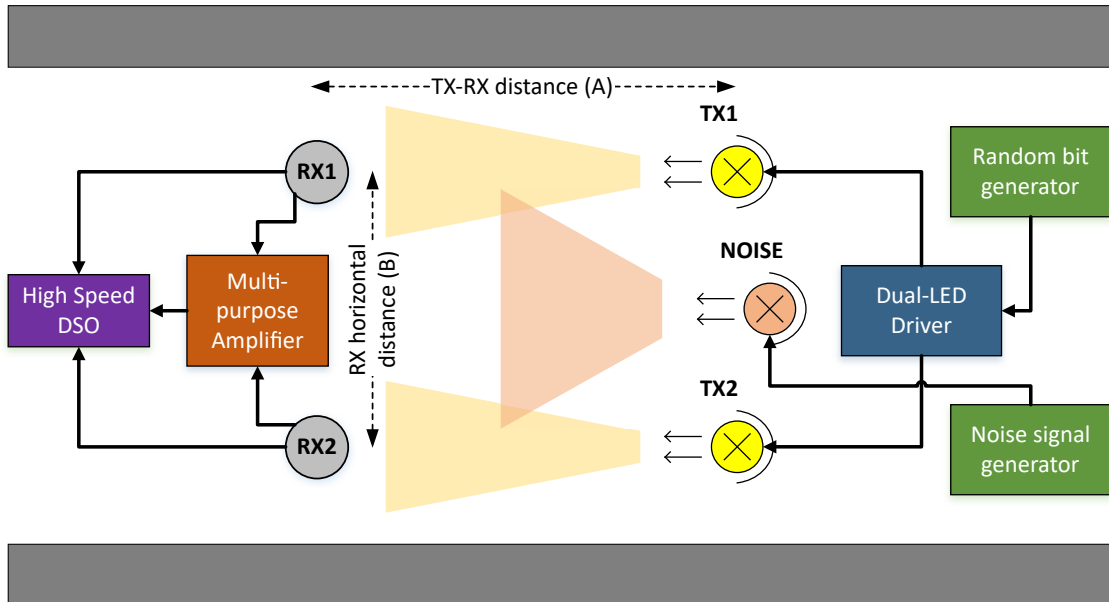


Figure 2.20: The schematic diagram of the indoor measurement setup. In this arrangement I was able to accurately compare the 2x2 D-SD and 2x2 C-SD setup with automotive-grade lighting equipment.

The two receivers were attached to adjustable height tripods for accurate positioning. The receiver signals were fed to a multi-purpose amplifier (able to operate in differential or in common-mode). The receiver signals and the multi-purpose

amplifier output signal was measured with a High-Speed Digital Storage Oscilloscope (HS-DSO).

For noise rejection performance evaluation purposes, a high-power 100 W LED-based noise source was added to the setup shown in Fig. 2.22. This noise source was precisely positioned in such a way, that it affects both receivers with the same amount of visible light noise. Hence, this is considered as an ideal common-mode balanced noise source in my setup. The driving signal for this LED is an independent pseudo-random bit sequence with the same 115.2 kbps data rate (square signal, OOK modulation). This signal is interpreted as a worst-case common-mode, balanced, in-band optical noise. The noise source can be toggled on and off between measurements.



Figure 2.21: Indoor laboratory measurement setup, for 2x2 D-SD vs. 2x2 C-SD comparison with deactivated common-mode noise source.

2.7.2 Noise Rejection Performance Measurement of 2x2 D-SD and 2x2 C-SD VLC-V2V

My goal with this measurement is to show that my suggested 2x2 D-SD VLC-V2V arrangement performs better than the conventional 2x2 C-SD solution. I set up 11 measurement distances, equidistantly spaced between 2 and 10 meters and measured the transmission quality with and without the presence of common-mode noise. Activated and deactivated noise source setups are shown in Fig. 2.22 and Fig. 2.23. Eye-diagrams and the corresponding Q-factors were obtained from the HS-DSO.

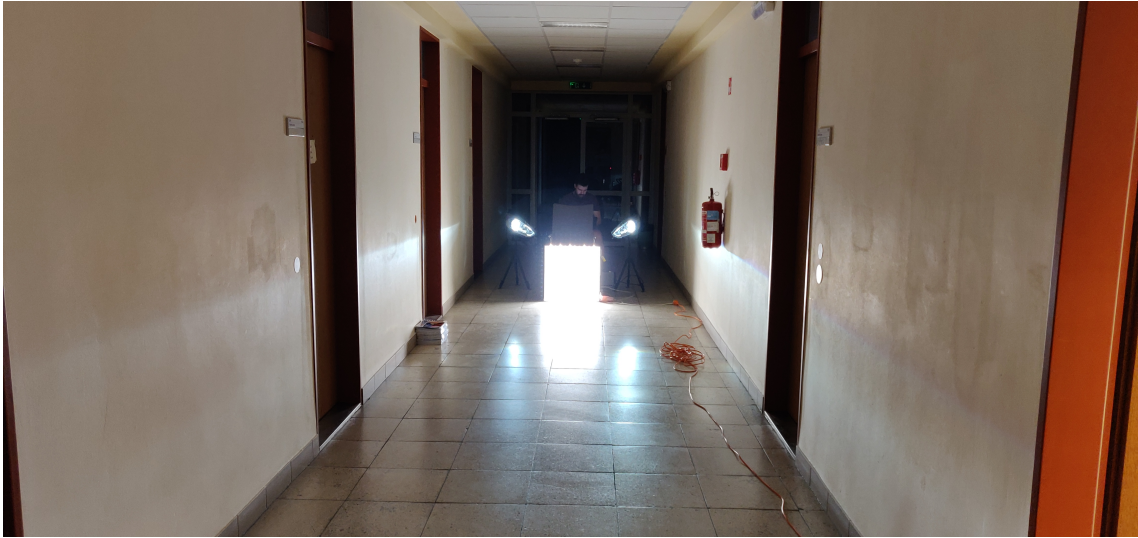


Figure 2.22: Indoor laboratory measurement setup for the 2x2 D-SD vs. 2x2 C-SD comparison, with activated common-mode noise source.

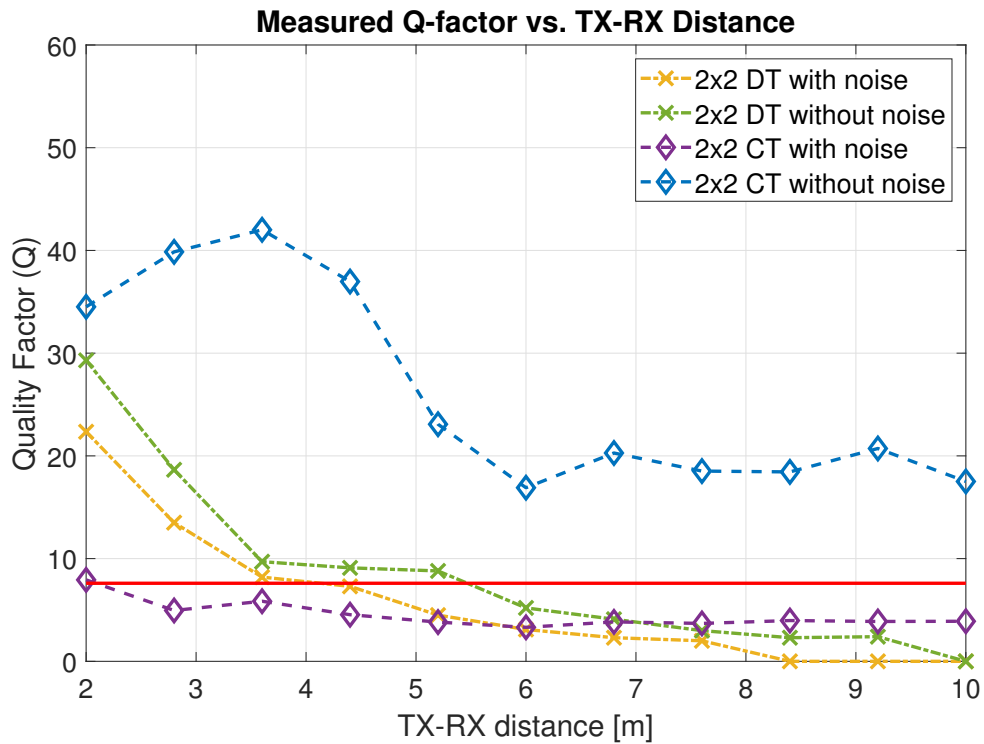


Figure 2.23: Measurement results. Noise rejection performance comparison between 2x2 D-SD and 2x2 C-SD transmission.

2.7.3 Measurement Results and Conclusion

The 2x2 measurement results are shown in Fig. 2.23. The best transmission performance is available with the 2x2 CT arrangement when the noise source was deactivated (denoted in blue with dashed line). The lowest acceptable Q-factor was 7.6, which is approximately equal to a BER value of 10^{-14} . This Q-factor

limit is denoted with a solid red line on Fig. 2.23. In practice, if the VLC-V2V channel's common-mode noise is low (or zero), the best transmission performance is available with the 2x2 C-SD arrangement as expected from the simulation results. However, if balanced common-mode noise is present, transmission performance dramatically decays. In these situations the 2x2 C-SD arrangement exhibits weak performance. The difference between 2x2 C-SD and 2x2 D-SD is clearly present. In case of 2x2 D-SD, the balanced common-mode noise does not influence transmission quality as noticeably, as in 2x2 C-SD. For distances between 2 and 6 meters, 2x2 D-SD (shown in green and yellow color in Fig. 2.23) outperforms the 2x2 C-SD arrangement in presence of common-mode balanced noise. On the other hand, for distances above 6 meters, 2x2 D-SD transmission has lower performance in every setup. Our assumption for this phenomenon is that it's mainly caused by the raised amount of crosstalk between channels. This crosstalk directly degrades transmission performance, and it is mainly originated from the divergence of the light beams emitted by the two LED headlights.

My measurement results proved that the 2x2 D-SD is a promising candidate for common-mode balanced noise rejection. 2x2 D-SD performed better than 2x2 C-SD in common-mode balanced noise situations (where TX-RX distance was less than 6 meters). Above TX-RX distances of 6 meters, the 2x2 D-SD performed weaker than 2x2 C-SD, due to the presumably higher crosstalk, i.e overlap between light beams at large distances. For distances less than 6 meters and environments where common-mode noise is present, 2x2 D-SD performs better. In noise-free situations the best performance is available with the 2x2 C-SD arrangement, as expected. After these results, my goal was to enhance the 2x2 D-SD noise cancellation performance further by reducing crosstalk between receivers.

2.7.4 Improvements in Crosstalk Reduction for 2x2 D-SD VLC-V2V Systems

The crosstalk between the two propagation routes can either be reduced by adjusting the divergence and altering the projected image of the headlights or changing the receivers' directional sensitivity. In VLC-V2V communication both solutions are available:

- headlight projection image electrically controlled using segmented LED arrays
or
- application of a Field-of-View (FOV) limiter to the amplified detector.

In my case I chose the latter, due to the transmitter headlight limitations and the more frequent use of H7 LED-based headlights. My FOV limiter attached to the amplified detector reduced the FOV to 30° in both horizontal and vertical directions.

2.7.5 Measurement Results with Receiver FOV Limiter

The FOV limiter was added to both receivers and measurements were conducted similarly to the previous section. As seen in Fig. 2.24, the Q-factors improved significantly in the case of 2x2 D-SD, compared to the previous measurement. Similarly to the previous measurement, the Q-factor limit is denoted with a solid red line on Fig. 2.24. It is important to highlight that the conventional 2x2 C-SD fails in presence of common-mode noise for distances above 4 meters. However, clearly due to the FOV limiter, the transmission quality is better for distances less than 4 meters when compared to the previous measurement. In balanced common-mode noise situations the 2x2 D-SD solidly outperformed 2x2 C-SD as expected. This result verified my previous assumption: the main performance decay in 2x2 D-SD for distances higher than 6 meters was due to the the overlap between light beams (crosstalk). The FOV limiter reduced crosstalk and the 2x2 D-SD transmission quality significantly improved. The results clearly show that in almost all cases my proposed 2x2 D-SD solution reached a higher Q-factor than the prescribed Q-factor limit (7.6). Furthermore, common-mode balanced noise does not affect 2x2 D-SD as significantly, as the 2x2 C-SD solution. To summarize, we can safely state that when balanced common-mode noise is present, my proposed 2x2 D-SD solution performs better than conventional 2x2 C-SD.

2.7.6 Future Plans for Crosstalk Reduction in 2x2 D-SD Systems

LED based headlights in modern vehicles, have opened up the way for adaptive projected light beam-forming by using segmented LED arrays. Using the built-in cameras in modern vehicles and combining their real-time image data with the adaptive headlights, road illumination efficiency can be improved. For instance, those dangerous traffic situations can be avoided where one vehicle's high-beam blinds the other vehicle's driver heading from the opposite direction. Furthermore, if the light-beam controller units are connected with the steering wheel position sensor, the light-beams are able to track the curvature of the road. This technology has already been implemented: Audi Matrix LED Lights, Mercedes Multi-Beam LED headlamps etc. As I mentioned earlier, crosstalk can be reduced in the 2x2

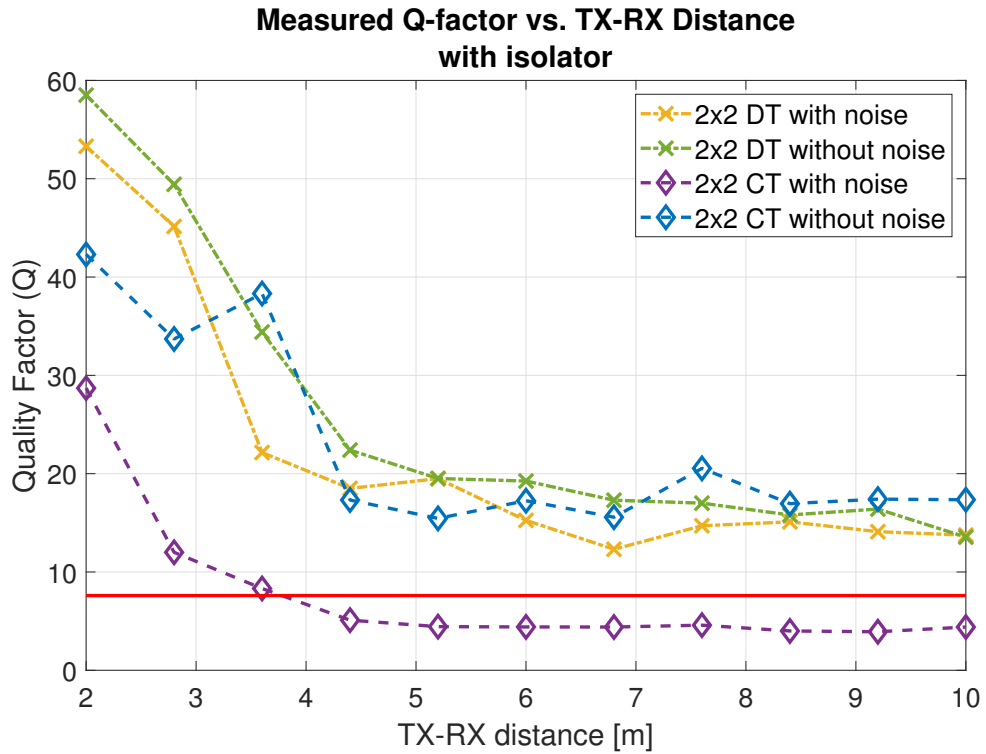


Figure 2.24: Measurement results. Noise rejection performance comparison between 2x2 D-SD and 2x2 C-SD transmission, using FOV limiters at the receiver side.

D-SD solution by altering the projected image of light beams. My future plan is to design a 2x2 D-SD VLC-V2V system with active vehicle tracking, shown in Fig. 2.25. By altering the communication LED segments (beam-segments) adaptively (VLC-V2V beam hopping) the crosstalk can be minimized between light beams, enhancing transmission quality. In my opinion, combining the adaptively controlled LED segments with the proposed 2x2 D-SD VLC-V2V structure, this would offer a powerful alternative to the 2x2 C-SD in cases where common-mode optical noise is dominant.

2.8 Summary of Thesis II.

In this thesis I proposed and presented a novel technique for reducing common-mode noise effects in VLC-V2V links. I presented the mathematical model of the proposed noise reduction method. I implemented a simulation environment in MATLAB to test the noise reduction efficiency, under several noise signal combinations and situations (balanced, unbalanced). I highlighted the negative effects of crosstalk and noise imbalance to the noise cancellation efficiency. Afterwards, I built a demonstration VLC-V2V 2x2 arrangement, based on automotive grade components. I conducted several indoor measurements for comparing my suggested solution to

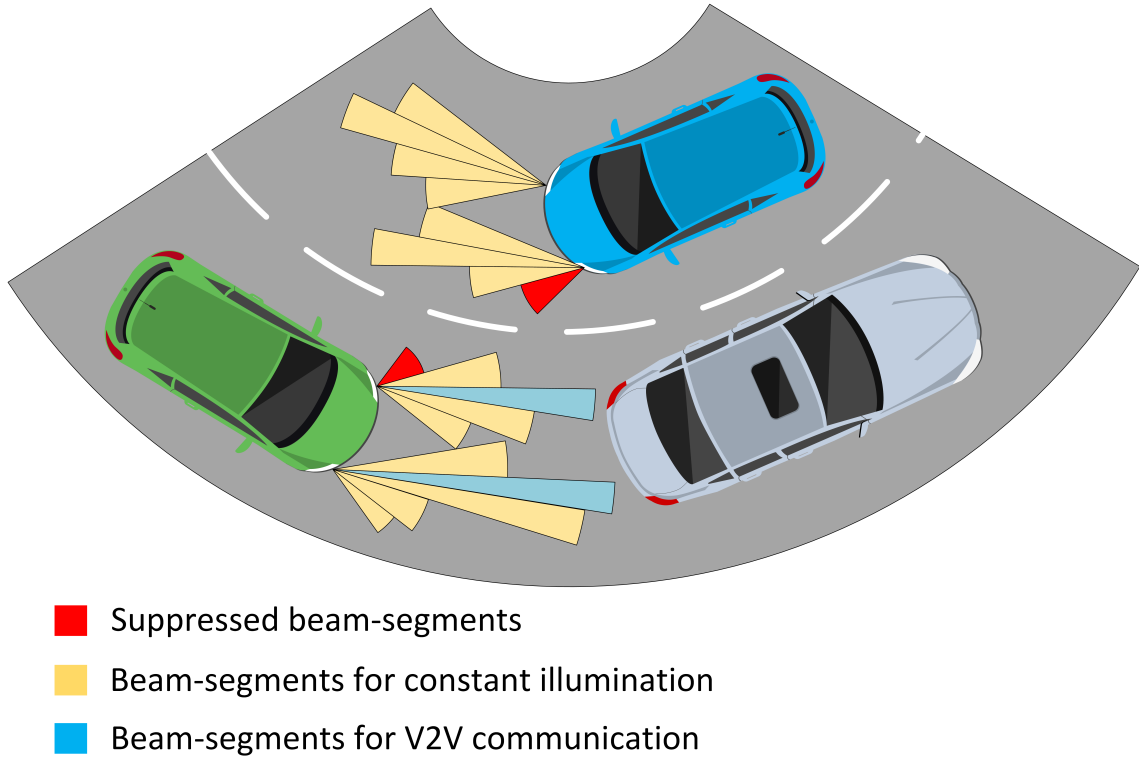


Figure 2.25: VLC-V2V using adaptively controlled LED headlight segments. V2V communication beams, suppressed beams and illumination beams are chosen with respect to relative vehicle orientation.

the commonly used common-mode TX-RX structure. The measurement results showed good correspondence with the theoretical and simulation expectations. I presented that regarding common-mode noise cancellation my suggested 2x2 D-SD arrangement performs significantly better, if noise levels are in the range of the utile signal and crosstalk level is low. I advised a method to reduce the crosstalk in 2x2 D-SD. The advised method reduced the crosstalk level and enhanced the 2x2 D-SD solution significantly. The whole work I presented in this thesis can be found in my published journal shown in the novel scientific results in Chapter 3.

Finally, I would like to briefly summarize the future plans for the VLC-V2V 2x2 D-SD system. Up until now, all the measurements were conducted under indoor, laboratory circumstances. My future plan is to integrate the 2x2 D-SD VLC-V2V transceiver structure into two vehicles and perform real-world road test with live communication and on-the-go bit error rate measurements. I would also like to examine the effects of sun irradiance, optical noises from vehicles in the adjacent lanes and how the 2x2 D-SD solution handles them. I'm also planning to design a test environment with LED matrix headlights, which are able to track the vehicle in front and create the adaptively chosen VLC-V2V beam hopping, shown in Fig. 2.25. This

might be able to help in: reducing adjacent lanes noise emission, stabilize VLC-V2V connection in bends and during cornering, reducing crosstalk between lamps.

Chapter 3

Novel Scientific Results: Summary of Theses and List of Related Publications

3.1 Thesis I. - Overcoming the Realization Problems of Wideband Impedance Matching Network Synthesis

Introduction

The Bode-Fano method provides the low-pass filter prototypes (impedance matching network prototype). As the majority of impedance matching tasks require band-pass response, frequency transformation is required [4]. At this point the matching network designer can freely choose between several realization options. One can choose: lumped element matching network, quarter-wave shunt-stub transmission line network or quarter-wave coupled line transmission line network. In case of lumped element networks the reactant elements are substituted by either a parallel or series resonant L-C structures. In transmission line networks mainly admittance or impedance inverters are used. Impedance and admittance inverters are also useful for altering the generator impedance for an arbitrary value (e.g. $50\ \Omega$). I discovered that during the synthesis of impedance or admittance inverters an important issue can occur: non-realizable matching network element values. This equally affects admittance and impedance inverter synthesis. My aim in this thesis is to find and eliminate the origins of non-realizable networks. I achieved this through the systematic inspection of all the input and internal parameters of

the admittance/impedance inverter synthesis process. Fortunately, I found some constraints that have proven to be useful for avoiding non-realizable networks. Under the *non-realizable* term I mean admittance/impedance values smaller than or equal to zero, or the values are not purely real. These realization constraints can also be inserted into an automated matching network synthesis algorithm. As an application example, I created an algorithm for finding the best acceptable and also realizable matching network in a MATLAB environment. With this algorithm the end-user can achieve better matching results, without needing to manually reiterate through several parameter values with a trial-and-error approach.

Thesis I/A. - Realization Constraints of Admittance Inverters based on Shunt Stub Transmission Lines

Admittance inverters are used when series R-L-C loads are matched to an arbitrary purely real generator impedance on a pre-defined frequency range (bandpass frequency response). In order to avoid non-realizable (complex or negative) matching network values, I present the results based on the analytical calculations in Sec. 1.7.1. If parameter $d > \frac{\delta}{2}$ then all impedance values are purely real [1, 5]. The rules for avoiding negative impedance values are a bit more complex.

1. If $Y_{2,3}$ is purely real, then $Y_{2,3} > 0$ without any further condition.
2. If $d_p < 1$ then $Y_2 > 0$ without any further condition. However, if $d_p > 1$ then $Y_2 > 0$ only if the necessary condition is fulfilled:

$$U < \frac{U}{2d_p} + 2 \frac{(d_p - 1)}{d_p} J_{2,3}. \quad (3.1)$$

3. The sufficient condition for $Y_3 > 0$ is:

$$d_p \frac{\delta}{k_{1,2}^2} < \frac{R_L}{\delta D R_g}. \quad (3.2)$$

Thesis I/B. - Realization Constraints of Impedance Inverters based on Coupled Transmission Lines

Impedance inverters are used when parallel R-L-C loads are matched to an arbitrary purely real generator impedance on a pre-defined frequency range (bandpass frequency response). To avoid non-realizable matching network values, I presented the results based on the analytical calculations in Sec. 1.7.2. If parameter $d > \frac{\delta}{2}$ then all impedance values are purely real. This result is similar to the one I got at

the admittance inverter analysis. The rules for avoiding negative impedance values are a bit more complex, therefore it can be found summarized below. As a rule of thumb, the arbitrary parameter d_p should be less than or equal to 1. But this is neither a necessary, nor a sufficient condition. The complete system of requirements for the coupled line impedance values to be larger than 0 is presented here.

1. $(Z_{0\text{-even}}^a)_{2,3} > 0$ is unconditionally fulfilled for any $d_p > 0$ values.
2. $(Z_{0\text{-odd}}^a)_{2,3} > 0$ must be separated into three further cases.
 - If $0 < d_p \leq 1$, then $(Z_{0\text{-even}}^a)_{2,3} > 0$.
 - If $d_p > 1$ and $U > K_{2,3}$ then $(Z_{0\text{-even}}^a)_{2,3} > 0$, where $U = R_{\text{L}} \tan(\Theta_1) \frac{\delta}{k_{1,2}^2}$.
 - If $d_p > 1$ and $U < K_{2,3}$ and $1 < d_p < \frac{U-2K_{2,3}}{2(U-K_{2,3})}$ then $(Z_{0\text{-even}}^a)_{2,3} > 0$.
3. $(Z_{0\text{-even}}^b)_{2,3} > 0$ is unconditionally fulfilled for any $d_p > 0$ values.
4. $(Z_{0\text{-odd}}^b)_{2,3} > 0$ if $(Z_{0\text{-even}}^b)_{2,3} > 2K_{2,3}$.

Thesis I/C. - Algorithmic Implementation of the Bode-Fano Method Demonstrated with Admittance Inverters using the Suggested Realization Constraints

The realization constraints alone does not actively aid efficient matching network synthesis. After an input parameter combination that resulted a non-realizable network, the parameters must be adjusted manually. Afterall, the whole process ends up being a series of trial-and-error iterations. Therefore, I suggested an efficient algorithm that pre-filters the non-realizable results, before the complete synthesis process is done [1]. Without this pre-filtering step, all parameter combinations must be analyzed separately, resulting in slow synthesis process (even if realization is impossible). Instead, the non-realizable networks are filtered out before the whole synthesis process, resulting in reasonably faster network synthesis.

Apart from, the arbitrary input parameter values (d_p, r) , I declared an adjustable relative bandwidth parameter b . This parameter aids the matching network designer to find the acceptable frequency response (required minimal bandwidth). Although, generally the required matching bandwidth is a static constant defined before the matching process is initiated, in the case of the Bode-Fano method there are situations where a narrower required bandwidth: smaller b is non-realizable and a higher b value is (or the opposite). For this reason, I set up parameter b to be

adjustable. I implemented the automated matching algorithm in MATLAB and presented the result of a series R-L load matching task as an example.

Using my suggested automated matching algorithm, the burdensome trial-and-error approach for finding the acceptable matching network is substituted with a significantly more efficient automated solution. The block diagram representing the iterative algorithm is shown in Sec. 1.8.

Thesis I/D. - Alternative Matching Approach for On-Chip Antennas used in UHF RFID Applications

Without a doubt, the Bode-Fano method does have its' limitations. In cases where the load quality factor is high ($Q > 30$) and the aimed frequency range is relatively large ($b > 1\%$) the synthesis process can potentially fail, without finding an acceptable result. For loads that are not well substituted by a single reactance load, the Bode-Fano method cannot be utilized. This is the case for ultra-small form factor, electrically small, On-chip RFID tag Antennas (OCA). For matching OCAs, alternative antenna design method is needed, presented in [2]. Without adding an additional matching network, altering the antenna geometry and adding a slow-wave structure resulted in better impedance matching and better radiation performance (details are shown in [2]).

3.2 Thesis II. - Differential Space-Divided 2x2 Visible Light Communication in Vehicle-to-Vehicle Applications

3.2.1 Introduction

In the last few years, VLC started to spread as the 6G initiative delegated it as a viable alternative to high-speed, local, secure RF communication. As modern lighting devices are based on semiconductor technology (LED, LASER), this gave an important boost for the area of VLC. Using VLC for V2V applications has spread in the last few years [6], as modern vehicles are equipped with LED lamps. This thesis focuses on a novel approach for enhancing the noise reduction performance of VLC links used in V2V applications. I proposed a differential 2x2 space-divided (2x2 D-SD) method for reducing common-mode noises in the VLC-V2V channel [7]. I made real-life measurements regarding the nature of optical noises, that may occur in the VLC-V2V channel. Based on the measurements, I built the demonstrative measurement setup and conducted several common-mode noise measurements and compared the performance of my suggested solution, with the conventional common-mode transmission (2x2 C-SD). My results showed, that my solution performed better, when common-mode noise was significant and transmission distance was under 10 meters [3].

Thesis II/A. - Common-Mode Noise in V2V-VLC Communication

My first assumption was regarding the presence of noises in the V2V-VLC channel under badly lit environmental conditions. I assumed that the major noise source is the light emitted by public lighting. Assuming, that the vehicles are far away from the public lighting, the light reaching the vehicle's chassis reaches both separated VLC receivers simultaneously, when they are placed on the rear of the vehicle near each other. I suggested a dual, spatially separated receiver structure and a differential amplifier to cancel out common-mode noise emitted by public lighting. I confirmed these assumptions with real-life road measurements which I carried out in an urban environment at night with a special equipped car. My measurements confirmed that: the VLC-V2V channel does contain common-mode noise emitted from public lighting and the differential receiver structure significantly reduced the amount of common-mode noise, as expected: up to 50 % in some situations, see [3].

Thesis II/B. - Simulation of Common-Mode Noise Reduction in V2V-VLC Application

For the sake of more exact comparison with the already widely used common-mode transmitter-receiver VLC-V2V structures, I introduced the simplified mathematical model of the 2x2 D-SD and 2x2 C-SD arrangement. I included thorough investigations regarding the advantages and disadvantages of the differential transmission method using a simulation environment I implemented in MATLAB. I compared my 2x2 D-SD solution under several conditions, including: overlapping between light beams (crosstalk), balanced and unbalanced common-mode and non-common-mode added noise. I also presented the versatility of the D-SD solution that it efficiently reduces common-mode noise without using optical domain filters or electrical domain filters. I showed the application limitations and criteria of the 2x2 D-SD arrangement. I presented several simulation arrangements for a wide range of signal and noise scenarios in [3]. I confirmed with simulations, that the 2x2 D-SD solution performs well under situations where the amount of common-mode noise is close to the level of the utile signal. I presented the disadvantageous effects of overlapping light beams at the receiver side with the simulation environment.

Thesis II/C. - Measurement Results of the Proposed Common-Mode Noise Reduction Technique

Based on the preliminary simulation results and arrangements, I built a complete 2x2 VLC-V2V setup using licensed automotive grade LED lamps (unlike the majority of published works, so far) and my custom designed VLC receivers. The quantity I used for rating the quality of the connection was the Q-factor I extracted from the eye-diagram. I also did approximate BER calculations, based on the Q-factor values. I conducted measurements at several TX-RX distances, with and without in-band common-mode noise source. I compared the 2x2 D-SD solution with the common 2x2 C-SD solution (where both transmitters send the same optical signal and receivers sum the incoming optical power). My results showed great correspondence with the simulation results. I measured that for shorter distances the 2x2 D-SD transmission performed significantly better, than for larger TX-RX distances, due to the overlapping light beams. 2x2 D-SD excelled at noise reduction compared to 2x2 C-SD, in those setups where common-mode noise level was relatively high. I was able to give a rule of thumb for those use cases, where 2x2 D-SD performs better than 2x2 C-SD. Finally, I gave a possible solution for reducing crosstalk between light beams, by applying Field-of-View (FOV) limiters on the receivers. By

attaching FOV limiters at the receiver side, the amount of crosstalk I measured, had reduced significantly enhancing the quality of connection and lowering BER values, as expected (see [3]).

Thesis Related Publications

Journal papers

- [1] Balázs Matolcsy and Attila Zólomy. “Overcoming the Realization Problems of Wideband Matching Networks”. In: *Infocommunications Journal* 10.4 (2019), pp. 31–36.
- [2] Balázs Matolcsy and Attila Zólomy. “Designing an Efficient Ultra Small Form Factor On-Chip Antenna for UHF RFID Application.” In: *Radioengineering* 29.2 (2019).
- [3] Balázs Matolcsy, Eszter Udvary, and Ágoston Schranz. “Common-mode noise filtering with space-divided differential 2x2 VLC for V2V applications”. In: *Optical and Quantum Electronics* 53.4 (2021). DOI: 10.1007/s11082-021-02808-z.

Conference papers

- [4] Balázs Matolcsy, Attila Zólomy, and Eszter Udvary. “Wideband impedance matching for VCSELs used in Free-Space quantum communication”. In: *2016 18th International Conference on Transparent Optical Networks (ICTON)*. IEEE. 2016, pp. 1–4.
- [5] Balázs Matolcsy and Attila Zólomy. “Practical Realization Rules for Wideband Impedance Matching using the Double-Terminated Filter Synthesis Method”. In: *2018 11th International Symposium on Communication Systems, Networks & Digital Signal Processing (CSNDSP)*. IEEE. 2018, pp. 1–5.
- [6] Tamás Szili, Balázs Matolcsy, and Gábor Fekete. “Water pollution investigations by underwater visible light communications”. In: *2015 17th International Conference on Transparent Optical Networks (ICTON)*. IEEE. 2015, pp. 1–4.

- [7] Balázs Matolcsy and Eszter Udvary. “Common-mode Noise Rejection in V2V/V2I Communication Based on Differential VLC Transmission”. In: *2020 12th International Symposium on Communication Systems, Networks and Digital Signal Processing (CSNDSP)*. IEEE. 2020, pp. 1–6.

Bibliography

- [8] H. W. Bode. *Network analysis and feedback amplifier design*. van Nostrand New York, 1945.
- [9] R. M. Fano. “Theoretical limitations on the broadband matching of arbitrary impedances”. In: *Journal of the Franklin Institute* 249.1 (1950), pp. 57–83.
- [10] R. Gudipati and W. K. Chen. “Explicit formulas for the design of broadband matching bandpass equalizers with Chebyshev response”. In: *Proceedings of ISCAS’95-International Symposium on Circuits and Systems*. Vol. 3. IEEE. 1995, pp. 1644–1647.
- [11] R. Levy. “Explicit formulas for Chebyshev impedance-matching networks, filters and interstages”. In: *Proceedings of the Institution of Electrical Engineers*. Vol. 111. 6. IET. 1964, pp. 1099–1106.
- [12] G Matthaei. “Synthesis of Tchebycheff impedance-matching networks, filters, and interstages”. In: *IRE Transactions on circuit theory* 3.3 (1956), pp. 163–172.
- [13] D. C. Youla. “A new theory of broad-band matching”. In: *IEEE Transactions on Circuit Theory* 11.1 (1964), pp. 30–50.
- [14] D. C. Youla, F. Winter, and S. U. Pillai. “A new study of the problem of compatible impedances”. In: *International journal of circuit theory and applications* 25.6 (1997), pp. 541–560.
- [15] K. Géher. “Linear Networks”. In: *Hungarian, Budapest* (1979), pp. 423–430.
- [16] H. Carlin and P. Crepeau. “Theoretical limitations on the broad-band matching of arbitrary impedances”. In: *IRE Transactions on Circuit Theory* 8.2 (1961), pp. 165–165.
- [17] T. R. Cuthbert. *Circuit design using personal computers*. Wiley, 1983.
- [18] C. M. Gewertz. “Synthesis of a Finite, Four-Terminal Net-Work from its Prescribed Driving-Point Functions and Transfer Function”. In: *Journal of Mathematics and Physics* 12.1-4 (1933), pp. 1–257.

- [19] D. M. Pozar. *Microwave Engineering*. John Wiley & Sons, 2011.
- [20] Wai-Kai Chen. *Broadband matching: Theory and implementations*. Vol. 18. World Scientific, 2015.
- [21] L. F. Chen et al. *Microwave Electronics: Measurement and Materials Characterization*. Wiley, 2004. ISBN: 9780470020456. URL: <https://books.google.hu/books?id=1vmUdUX1BNIC>.
- [22] G. L. Matthaei, L. Young, and E. M. T. Jones. *Microwave filters, impedance-matching networks, and coupling structures*. Artech house, 1980.
- [23] S. Darlington. “Synthesis of Reactance 4-Poles Which Produce Prescribed Insertion Loss Characteristics: Including Special Applications To Filter Design”. In: *Journal of Mathematics and Physics* 18.1-4 (1939), pp. 257–353.
- [24] E. Green. *Amplitude-frequency Characteristics of Ladder Networks*. Marconi’s Wireless Telegraph Company, 1954.
- [25] W. T. Luk and K. N. Yung. “Bending dipole design of passive UHF RFID tag antenna for CD / DVD discs”. In: *Proc. Asia-Pacific Microwave Conf.* 2008, pp. 1–4. DOI: 10.1109/APMC.2008.4958093.
- [26] B. D. Braaten, M. Reich, and J. Glower. “A Compact Meander-Line UHF RFID Tag Antenna Loaded With Elements Found in Right/Left-Handed Coplanar Waveguide Structures”. In: *IEEE Antennas and Wireless Propagation Letters* 8 (2009), pp. 1158–1161. DOI: 10.1109/LAWP.2009.2034990.
- [27] W. Pachler et al. “A novel booster antenna design coupled to a one square millimeter coil-on-chip RFID tag enabling new medical applications”. In: *Proc. European Microwave Conf.* 2013, pp. 1003–1006. DOI: 10.23919/EuMC.2013.6686829.
- [28] P. Jankowski-Mihulowicz, D. Kawalec, and M. Weglarski. “Antenna design for semi-passive UHF RFID transponder with energy harvester”. In: *Radioengineering* 24.3 (2015), p. 723.
- [29] P. Jankowski-Mihulowicz. “A method for measuring the radiation pattern of UHF RFID transponders”. In: *Metrology and Measurement Systems* 23.2 (2016), pp. 163–172.
- [30] Ronold W. P. King. *The Theory of Linear Antennas. With Charts and Tables for Practical Applications*. 2013. DOI: 10.4159/harvard.9780674182189.

- [31] K. Fujimoto and H. Morishita. *Modern Small Antennas*. 2013. DOI: 10.1017/cbo9780511977602.
- [32] J. Rashed-Mohassel, A. Mehdipour, and H. Aliakbarian. “New schemes of size reduction in space filling resonant dipole antennas”. In: *Proc. 3rd European Conf. Antennas and Propagation*. 2009, pp. 2430–2432.
- [33] C. P. Baliarda, J. Romeu, and A. Cardama. “The Koch Monopole: a Small Fractal Antenna”. In: *IEEE Transactions on Antennas and Propagation* 48.11 (2000), pp. 1773–1781. DOI: 10.1109/8.900236.
- [34] Jinhui Zhu, Hoorfar, and Engheta. “Peano antennas”. In: *IEEE Antennas and Wireless Propagation Letters* 3 (2004), pp. 71–74. DOI: 10.1109/LAWP.2004.827899.
- [35] X. Chen, S. S. Naeini, and Y. Liu. “A down-sized printed Hilbert antenna for UHF band”. In: *Proc. IEEE Antennas and Propagation Society Int. Symp.. Digest. Held in conjunction with: USNC/CNC/URSI North American Radio Sci. Meeting (Cat. No.03CH37450)*. Vol. 2. 2003, 581–584 vol.2. DOI: 10.1109/APS.2003.1219304.
- [36] R. G: Hohlfeld and N. Cohen. “Self-similarity and the geometric requirements for frequency independence in antennae”. In: *Fractals* 07.01 (1999), pp. 79–84. DOI: 10.1142/s0218348x99000098.
- [37] H. Stockman. “Communication by Means of Reflected Power”. In: *Proceedings of the IRE* 36.10 (1948), pp. 1196–1204. DOI: 10.1109/JRPROC.1948.226245.
- [38] Hitachi. *Design Guideline – Hitachi USPT Ultra-Small UHF RFID Tag*. Online: 2021. 03. 14. 2016. URL: <https://echaintechnology.com/product/hitachi-uspt-ultra-small-versatile-embeddable-indestructible-uhf-rfid-tag/>.
- [39] Hitachi. *Datasheet – Hitachi USPT Ultra-Small UHF RFID Tag*. Online: 2021. 03. 14. 2016. URL: https://www.hitachi-chem.co.jp/english/products/ppcm/files/IM5-PK2525_Datasheet_ver.3.0.pdf.
- [40] Eszter Udvary. “Visible Light Communication Survey”. In: *Infocommunications Journal* 11.2 (June 2019), pp. 22–31. ISSN: 2061-2079.
- [41] T. Komine and M. Nakagawa. “Fundamental analysis for visible-light communication system using LED lights”. In: *IEEE Transactions on Consumer Electronics* 50 (1 2004), pp. 100–107. ISSN: 1558-4127. DOI: 10.1109/TCE.2004.1277847.

- [42] S. Rajagopal, R. D. Roberts, and S-K. Lim. “IEEE 802.15.7 Visible Light Communication: Modulation schemes and dimming support”. In: *IEEE Communications Magazine* 50 (3 2012), pp. 72–82. ISSN: 1558-1896. DOI: 10.1109/MCOM.2012.6163585.
- [43] IMDEA. *IMDEA Networks introduces the OpenVLC platform for research in Visible Light Communication Systems*. Online: 2020. 03. 14. Aug. 2018. URL: <http://netcom.it.uc3m.es/news/2016/imdea-networks-introduces-openvlc-platform-research-visible-light-communication-systems.html>.
- [44] I. C. Rust and H. H. Asada. “A dual-use visible light approach to integrated communication and localization of underwater robots with application to non-destructive nuclear reactor inspection”. In: *Proc. IEEE Int. Conf. Robotics and Automation*. 2012, pp. 2445–2450.
- [45] A. K. Das et al. “Underwater communication system for deep sea divers using visible light”. In: *Proc. Photonics Global Conf. (PGC)*. 2012, pp. 1–3.
- [46] Ming Chen et al. “Demonstration of a 2.34 Gbit/s Real-Time Single Silicon-Substrate Blue LED-Based Underwater VLC System”. In: *IEEE Photonics Journal* 12 (1 2020), pp. 1–11. ISSN: 1943-0647. DOI: 10.1109/JPHOT.2019.2958969.
- [47] C. Shen et al. “Going beyond 10-meter, Gbit/s underwater optical wireless communication links based on visible lasers”. In: *Proc. Opto-Electronics and Communications Conf. (OECC) and Photonics Global Conf. (PGC)*. 2017, pp. 1–3.
- [48] M. Jain et al. “Performance Analysis of NOMA Assisted Underwater Visible Light Communication System”. In: *IEEE Wireless Communications Letters* 9.8 (2020), pp. 1291–1294.
- [49] A. K. Chaudhary, S. Shukla, and S. Singh. “Analysis of Underwater Wireless Communication using Visible Light LEDs”. In: *Proc. IEEE Int. Students’ Conf. Electrical, Electronics and Computer Science (SCEECS)*. 2020, pp. 1–4.
- [50] Giuseppe Schirripa Spagnolo, Lorenzo Cozzella, and Fabio Leccese. “Underwater Optical Wireless Communications: Overview”. In: *Sensors* 20.8 (2020), p. 2261. DOI: 10.3390/s20082261.
- [51] P. Lou et al. “Fundamental analysis for indoor visible light positioning system”. In: *Proc. 1st IEEE Int. Conf. Communications in China Workshops (ICCC)*. 2012, pp. 59–63.

- [52] S. Yang, E. Jung, and S. Han. “Indoor Location Estimation Based on LED Visible Light Communication Using Multiple Optical Receivers”. In: *IEEE Communications Letters* 17.9 (2013), pp. 1834–1837.
- [53] C. Wang et al. “The research of indoor positioning based on visible light communication”. In: *China Communications* 12.8 (2015), pp. 85–92.
- [54] J. Luo, L. Fan, and H. Li. “Indoor Positioning Systems Based on Visible Light Communication: State of the Art”. In: *IEEE Communications Surveys Tutorials* 19.4 (2017), pp. 2871–2893.
- [55] W. Raes, L. D. Strycker, and N. Stevens. “Design and Accuracy Evaluation of a RSS-Based Visible Light Positioning Implementation”. In: *Proc. Navigation and Communications (WPNC) 2018 15th Workshop Positioning*. 2018, pp. 1–5.
- [56] A. Funahashi et al. “i-LightHouse: A Visible Light Communication system for the visually impaired”. In: *Proc. Indoor and Mobile Radio Communications 2011 IEEE 22nd Int. Symp. Personal*. 2011, pp. 1026–1030.
- [57] A. Jayakody et al. “AVII [Assist Vision Impaired Individual]: An Intelligent Indoor Navigation System for the Vision Impaired Individuals with VLC”. In: *Proc. IEEE Int. Conf. Information and Automation for Sustainability (ICIAfS)*. 2016, pp. 1–6.
- [58] D. Mohammed et al. “Digital Data Transmission via Visible Light Communication (VLC): Application to Vehicle to Vehicle Communication”. In: *Proc. 4th Int. Conf. Control Engineering Information Technology (CEIT)*. 2016, pp. 1–5.
- [59] P. A. P. Ferraz and I. S. Santos. “Visible Light Communication Applied on Vehicle-to-Vehicle Networks”. In: *Proc. Electronics and Automotive Engineering (ICMEAE) 2015 Int. Conf. Mechatronics*. 2015, pp. 231–235.
- [60] J-H. Yoo et al. “Demonstration of Vehicular Visible Light Communication based on LED Headlamp”. In: *Proc. Fifth International Conference Ubiquitous and Future Networks (ICUFN)*. 2013, pp. 465–467.
- [61] M. Uysal et al. “Visible Light Communication for Vehicular Networking: Performance Study of a V2V System Using a Measured Headlamp Beam Pattern Model”. In: *IEEE Vehicular Technology Magazine* 10.4 (2015), pp. 45–53.

- [62] J. Kim et al. “Vehicle-to-vehicle visible light communications using sub-pulse Manchester modulation”. In: *Proc. Sixth Int. Conf. Ubiquitous and Future Networks (ICUFN)*. 2014, pp. 481–482.
- [63] K. Siddiqi, A. D. Raza, and S. S. Muhammad. “Visible Light Communication for V2V Intelligent Transport System”. In: *Proc. Int. Conf. Broadband Communications for Next Generation Networks and Multimedia Applications (CoBCom)*. 2016, pp. 1–4.
- [64] A. Chen et al. “Time variation in vehicle-to-vehicle visible light communication channels”. In: *Proc. IEEE Vehicular Networking Conf. (VNC)*. 2016, pp. 1–8.
- [65] S. J. Lee et al. “Simulation modeling of visible light communication channel for automotive applications”. In: *Proc. 15th Int. IEEE Conf. Intelligent Transportation Systems*. 2012, pp. 463–468.
- [66] F. M. Alsalami et al. “Regular-Shaped Geometry-Based Stochastic Model for Vehicle-to-Vehicle Visible Light Communication Channel”. In: *Proc. IEEE Jordan Int. Joint Conf. Electrical Engineering and Information Technology (JEEIT)*. 2019, pp. 297–301.
- [67] M. Karbalayghareh et al. “Channel Modelling and Performance Limits of Vehicular Visible Light Communication Systems”. In: *IEEE Transactions on Vehicular Technology* (2020), p. 1.
- [68] H. B. Eldeeb, F. Miramirkhani, and M. Uysal. “A Path Loss Model for Vehicle-to-Vehicle Visible Light Communications”. In: *Proc. 15th Int. Conf. Telecommunications (ConTEL)*. July 2019, pp. 1–5. DOI: 10.1109/ConTEL.2019.8848562.
- [69] Y. H. Kim, W. A. Cahyadi, and Y. H. Chung. “Experimental Demonstration of VLC-Based Vehicle-to-Vehicle Communications Under Fog Conditions”. In: *IEEE Photonics Journal* 7.6 (2015), pp. 1–9.
- [70] M. Elamassie et al. “Effect of Fog and Rain on the Performance of Vehicular Visible Light Communications”. In: *Proc. IEEE 87th Vehicular Technology Conf. (VTC Spring)*. 2018, pp. 1–6.
- [71] E. Eso et al. “Experimental Investigation of the Effects of Fog on Optical Camera-based VLC for a Vehicular Environment”. In: *Proc. 15th Int. Conf. Telecommunications (ConTEL)*. 2019, pp. 1–5.
- [72] L. Cheng et al. “Comparison of Radio Frequency and Visible Light Propagation Channels for Vehicular Communications”. In: *IEEE Access* 6 (2018), pp. 2634–2644.

- [73] C. Tebruegge, A. Memedi, and F. Dressler. “Empirical Characterization of the NLOS Component for Vehicular Visible Light Communication”. In: *Proc. IEEE Vehicular Networking Conf. (VNC)*. 2019, pp. 1–4.
- [74] G. Singh, A. Srivastava, and V. A. Bohara. “Impact of Weather Conditions and Interference on the Performance of VLC based V2V Communication”. In: *Proc. 21st Int. Conf. Transparent Optical Networks (ICTON)*. 2019, pp. 1–4.
- [75] M. S. Islim et al. “The Impact of Solar Irradiance on Visible Light Communications”. In: *Journal of Lightwave Technology* 36.12 (June 2018), pp. 2376–2386. ISSN: 1558-2213. DOI: 10.1109/JLT.2018.2813396.
- [76] Y. H. Chung and S. Oh. “Efficient optical filtering for outdoor visible light communications in the presence of sunlight or artificial light”. In: *Proc. Int. Symp. Intelligent Signal Processing and Communication Systems*. Nov. 2013, pp. 749–752. DOI: 10.1109/ISPACS.2013.6704649.
- [77] M. Beshr, C. Michie, and I. Andonovic. “Evaluation of Visible Light Communication system performance in the presence of sunlight irradiance”. In: *Proc. 17th Int. Conf. Transparent Optical Networks (ICTON)*. July 2015, pp. 1–4. DOI: 10.1109/ICTON.2015.7193685.
- [78] I. Takai et al. “Optical Vehicle-to-Vehicle Communication System Using LED Transmitter and Camera Receiver”. In: *IEEE Photonics Journal* 6.5 (2014), pp. 1–14.
- [79] S. Halawi et al. “Performance Analysis of Circular Color Shift Keying in VLC Systems With Camera-Based Receivers”. In: *IEEE Transactions on Communications* 67.6 (2019), pp. 4252–4266.
- [80] M. Ahmed and A. Bermak. “A CMOS Transimpedance Amplifier With Ambient Light Rejection for Visible Light Communication in Intelligent Transport Systems”. In: *Proc. 15th Int. Wireless Communications Mobile Computing Conf. (IWCMC)*. June 2019, pp. 7–13. DOI: 10.1109/IWCMC.2019.8766535.
- [81] C. Tebruegge, Q. Zhang, and F. Dressler. “Optical Interference Reduction with Spatial Filtering Receiver for Vehicular Visible Light Communication”. In: *Proc. IEEE Intelligent Transportation Systems Conf. (ITSC)*. Oct. 2019, pp. 3055–3061. DOI: 10.1109/ITSC.2019.8917042.

- [82] T. Adiono et al. “Analog filters design in VLC analog front-end receiver for reducing indoor ambient light noise”. In: *Proc. IEEE Asia Pacific Conf. Circuits and Systems (APCCAS)*. Oct. 2016, pp. 581–584. DOI: 10.1109/APCCAS.2016.7804058.
- [83] F. Chang et al. “Design and implementation of anti low-frequency noise in visible light communications”. In: *Proc. Int. Conf. Applied System Innovation (ICASI)*. May 2017, pp. 1536–1538. DOI: 10.1109/ICASI.2017.7988219.
- [84] M. R. Alam and S. Faruque. “Prospects of differential optical receiver with ambient light compensation in vehicular visible light communication”. In: *Proc. IEEE Vehicular Networking Conf. (VNC)*. 2016, pp. 1–4.
- [85] H. Farahneh, S. M. Kamruzzaman, and X. Fernando. “Differential Receiver as a Denoising Scheme to Improve the Performance of V2V-VLC Systems”. In: *Proc. IEEE Int. Conf. Communications Workshops (ICC Workshops)*. 2018, pp. 1–6.
- [86] M. R. Alam and S. Faruque. “Prospects of differential optical receiver with ambient light compensation in vehicular visible light communication”. In: *Proc. IEEE Vehicular Networking Conf. (VNC)*. Dec. 2016, pp. 1–4. DOI: 10.1109/VNC.2016.7835929.
- [87] Gábor Fekete et al. “Visible light communication channel disturbances and examination of the modulation formats”. In: *International Journal of Microwave and Wireless Technologies* 8.8 (2015), pp. 1163–1171. DOI: 10.1017/s1759078715001269.